

國立臺灣大學工學院應用力學研究所



博士論文

Graduate Institute of Applied Mechanics

College of Engineering

National Taiwan University

Doctoral Dissertation

三相線張力於遲滯角之影響與光控仿生偶氮苯花瓣

Evolution of three-phase line tension on contact angle
hysteresis and photo-controllable design on an artificial
Azo-IPN petal

翁承義

Cheng-Hsi Weng

指導教授：張培仁 博士

施文彬 博士

Advisor: Pei-Zen Chang, Ph.D.

Wen-Pin Shih, Ph.D.

中華民國 107 年 04 月

April, 2018

國立臺灣大學博士學位論文
口試委員會審定書

三相線張力於遲滯角之影響與光控仿生偶氮
苯花瓣

Evolution of three-phase line tension on contact
angle hysteresis and photo-controllable design on
an artificial Azo-IPN petal

本論文係翁承義君（學號：F99543035）在國立臺灣大學應用力學研究所完成之博士學位論文，於民國 107 年 4 月 2 日承下列考試委員審查通過及口試及格，特此證明

口試委員：

張培仁 張培仁 施文彬



(指導教授)

賴君亮 賴君亮

戴子安 戴子安

楊馥菱 楊馥菱

胡毓忠 胡毓忠

所 長

王立昇 王立昇

致謝



在這研究所的求學期間，很高興能加入應力所張培仁老師的實驗室，與大學的基礎研究不同，在研究所的期間開始學著探討問題與解決問題，謝謝張老師在這一路上的指導，雖然張老師很忙碌，但皆能仔細的聆聽我在研究的過程中所遇到的問題，提供有效的解決方式與適合的研究策略。也很感謝機械所施文彬老師的教導，每週的開會討論，盯著研究進度，激勵思考，嚴格的訓練，讓自己在邏輯的訓練上更加清晰，研究的架構更加明確。

感謝賴君亮老師、戴子安老師、胡毓忠老師與楊馥菱老師在忙碌中抽空來給予指教，在口試的過程中，更回頭省視過去的研究，不同角度下的討論，讓自己在研究上有更細膩的探討，更透徹的了解。

感謝實驗室的助理，美芳，對實驗室大家的關照，關心在研究之外所遇到的生活問題，製造樂趣，讓繁重的研究生活增添了歡樂的氣氛。進到實驗室後，受到很多張 group 學長姐、學弟妹的幫忙，很感謝小丁、小祥、小金、婉君、建君、仁傑、歐弟、郁智、海鄰、小郭、小江、文章、富程、Mars、政道、蔡球、孟洋、則翔、泓緯、雅珊、福臨、葉廷、元玠、柏瑄、胤禎、承祐、家銘、品蓉、子森與仲璿的幫忙，而在 R433 的實驗室裡，飛龍、育諺、KiKi、宜靜、彪姐、俊彥、隆翊、聿庭、羿穎、小龍、Christian 與凱全等等，讓實驗室的生活充滿朝氣。也很感謝 TiMMeL 實驗室，承俊、品淳、彥安、瑋杰等，以及順區的幫忙，讓實驗得以順利。要感謝的人很多，不同的研究室也好，不同科系也好，相互的砥礪與鼓勵，讓研究生的這幾年充滿回憶，也祝福每個人都能邁向自己的目標，勇往直前。

最後，很感謝家人在這一路的支持，求學之路方能順利完成，最後特別感謝女友，巧怡的陪伴，讓煩悶時有吐露的對象，讓自己在焦躁時能靜下來好好規劃，謝謝。



很榮幸在張培仁老師的實驗室完成學業，盼自己未來也能是實驗室的驕傲。

翁承義

2018 年 05 月謹誌於台灣大學

中文摘要



本論文展示花瓣效應是由線張力所控制，並發現表面的結構的特徵長度所扮演的重要角色。藉由線張力所修正的 Wenzle 方程式，對應實驗上的數據是較合理的。在這研究中利用高分子材料設計不同的特徵長度的基材表面，進一步去評估在這樣的不同的表面粗糙度與表面接觸線比例對於遲滯角的影響。在遲滯角實驗中，線張力是會轉變的，並且由正轉為負值，轉變的過程，遲滯的狀態也剛好是前進角轉為後退角的狀態。可發現表面粗糙度影響的是在前進角的階段，線張力則是主要影響後退角。當增加特徵長度時，接觸角可從 107 ± 1.1 度增加為 129.3 ± 0.9 度，而遲滯角的部分則是明顯的由 23.1 ± 1.3 度增加到 62.1 ± 2.1 度。在這樣的實驗觀察結果下，線張力對於潤濕效應的影響有了清楚的了解，並可以設計所需要的結構表面，這對於生醫上的設計與應用可以有大幅的幫助。

在這研究中，了解表面粗糙度對於潤濕效應的影響，進一步發展表面能量對於潤濕效應的影響。開發一可光控的人造玫瑰花瓣，藉由偶氮苯以互穿型網狀結構作為設計。玫瑰花瓣上的微米與奈米結構皆完整的仿生玫瑰花瓣上的微米與奈米結構皆完整的複製。由於偶氮苯是光學幾何異構物，就由不同的波長的光照射，偶氮苯的順反異構物有不同的表面能量，使得此仿生花瓣的接觸角度變化範圍 99.2 ± 0.9 度至 140.9 ± 1.8 度，遲滯角也可在 99.2 ± 0.9 度到 140.9 ± 1.8 度之間來回變化，比起真實的玫瑰，此仿生花瓣有更高的接觸角與更明顯的遲滯效應，更進一步的是可用非接觸的光學方式進而改變與調整。

關鍵字：花瓣效應、線張力、特徵長度、遲滯角、高分子與仿生

Abstract



This paper experimentally investigated how the petal effect is governed by line tension and showed that the characteristic length of the surface structure plays an important role. Particularly, Wenzel's equation modified with line tension was used to model the contact angle hysteresis. We designed different surfaces on polydimethylsiloxane with various structure lengths, 15 to 50 μm , to evaluate the effect of surface roughness and the actual length of the three-phase contact line on the contact angle hysteresis. The sign of the line tension alters from positive to negative when the droplet changes from advancing to receding state. The surface tension dominates the contact angle in the advancing state while the line tension governs the contact-line movement in the receding state. By increasing the characteristic length of the surface structure, the static contact angle can be altered from $107 \pm 1.1^\circ$ to $129.3 \pm 0.9^\circ$, and the contact angle hysteresis changes obviously from $23.1 \pm 1.3^\circ$ to $62.1 \pm 2.1^\circ$. These results facilitate better understanding of the effect of line tension on a wetting surface for a more robust biomimetic design.

This paper presents a biomimetic rose petal whose contact angle hysteresis can be reversibly tuned by photo-illumination. With azobenzene interpenetrating polymer network, the micron- and nano-scale surface structure of a rose petal was duplicated. By changing the exposure light wavelength, the surface free energy of the artificial petal was modulated between trans-to-cis azobenzene photo-isomerations. The static contact angle of the artificial petal can be tuned to range from $99.2 \pm 0.9^\circ$ to $140.9 \pm 1.8^\circ$. The contact angle hysteresis between $50.3 \pm 0.6^\circ$ and greater than 84° can be achieved. Comparing to the value measured on a real rose petal, the fabricated counterpart presents more prominent petal effect in terms of larger static contact angle and greater contact angle hysteresis.

Keywords: petal effect, line tension, characteristic length, contact angle hysteresis, polymers, biomimetic.



Contents

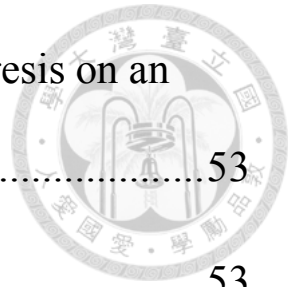


致謝.....	ii
中文摘要.....	iv
Abstract	v
Contents	vii
Figures.....	x
Tables.....	xxi
Nomenclature	xxii
.Chapter 1 Introduction	1
1.1 Motivation	1
1.2 Literature Survey	2
1.2.1. Line tension	2
1.2.2. Azobenzene in interpenetrating polymer networks.....	4
.Chapter 2 Wetting behavior theories	9
2.1 Introduction	9
2.2 Modified Young equation.....	10

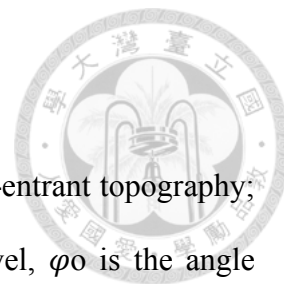


2.3 Modified Wenzel equation.....	12
2.4 Modified Gibbs free energy of Wenzel's model.....	14
.Chapter 3 Evolution of three-phase line tension on petal-like	
contact angle hysteresis.....	16
3.1 Introduction	16
3.2 Experiment	19
3.2.1 Materials and fabrication	19
3.2.2 Measurement of contact angles.....	20
3.3 Results and discussion	21
3.3.1 Static contact angle.....	21
3.3.2 Contact angle hysteresis.....	23
3.3.3 Hysteresis of Gibbs free energy.....	26
3.3.4 Ratio of the actual length of the contact line to the apparent (κ)	28
3.3.5 Effect of structure length	29
3.4 Conclusion.....	31
3.5 Experiment Results of other structures	31

.Chapter 4 Photo-controllable contact angle hysteresis on an artificial Azo-IPN petal.....	53
4.1 Introduction	53
4.2 Material and fabrication.....	53
4.3 Measurement procedure of the contact angle hysteresis	56
4.4 Conclusion.....	63
.Chapter 5 Conclusions	64
.Chapter 6 Future works	65
6.1 Redefined surface roughness (λ) and ratio of actual length of the three-phase contact line to the apparent (κ).....	65
6.2 New derivation	67
References	72



Figures



- Figure 1. Geometrical air trapping on a hydrophilic relief with re-entrant topography;
 φ is the angle corresponding to the current liquid level, φ_0 is the angle
corresponding to the initial liquid level, θ_Y is the Young angle [10]..... 3
- Figure 2. The determination of contact line tension. (a-e) The contact line energy τL
versus the droplet circumference $2\pi r$ at different fluid-solid interaction
strengths of ϵ_{sf} . (f) The obtained contact line tension τ versus the fluid-solid
interaction ϵ_{sf} [11]. 4
- Figure 3. The photo-isomerization of azobenzene compounds. 5
- Figure 4. The optomechanical response of an LCE sample. Two frames from a video
clip recording the bending and relaxation dynamics of the sample. The
measured displacement of the LCE sample center from its initial rest position
as a function of time from onset of illumination [17]. 6
- Figure 5. Model for the UV-induced change in the elasticity [18]. 7
- Figure 6. The reversible UV response of the length of the semi-IPN film at 25°C [18].
..... 7
- Figure 7. Photoisomerization of azobenzene moieties in the surface of the azo-HPC
films [21]. 8
- Figure 8. (a) The changes of contact angle of the azo-HPC3 film over several cycles of
irradiation with UV light ($\lambda = 365$ nm) for 20 min and subsequently with
visible light ($\lambda > 420$ nm) for 25 min. (b) The variation of the contact angle
($\Delta\theta$) of the azo-HPCs upon irradiation by UV and subsequently by visible
light under the conditions of (a) [21]. 8
- Figure 9. Droplet in contact with a flat solid surface. 10

Figure 10. (a) Droplet in contact with rough solid surface. (b) l is the actual length of contact line; L is the apparent length.	12
Figure 11. (a) Droplet in contact with a solid surface. (b) Advancing and receding angles.	18
Figure 12. (a) Microscopic image of a fabricated PDMS surface. (b) Schematic view of the surface. (c) Process flow for fabricating the silicon mold.....	20
Figure 13. Images of expansion and contraction of the DI water droplet on the flat PDMS surface. The droplet volume was increased from 0.5 μL to 5 μL at 0.5 μL increment and then decreased.	21
Figure 14. (a) The relationship between the apparent contact angle and intrinsic contact angle by ignoring the effect of line tension. The inset shows the measurement and Wenzel's equation for all λ 's. (b) Extracted line tension at different surface roughness.....	22
Figure 15. The measurement results of $\lambda=1.33$ and $\kappa=1.37$. (a) Contact angle hysteresis. (b) Radius of contact line versus droplet volume. (c) Line tension versus droplet volume. (d) Line tension versus radius of contact line.	26
Figure 16. Gibbs energy (G^*) of $L=15 \mu\text{m}$ with (a) $\lambda=1.33$. (b) $\lambda=1.12$. (c) $\lambda=1.06$. $\Delta G \sim 0$ for θ is equal to advancing angle and receding angle.....	27
Figure 17. (a) Extracted line tension versus the radius of three-phase contact line for $L=15 \mu\text{m}$. Measured contact angle versus the radius of three-phase contact line.....	29
Figure 18. CA hysteresis versus κ for different structure lengths: (a) $L=25 \mu\text{m}$. (b) $L=30 \mu\text{m}$. (c) $L=35 \mu\text{m}$. (d) $L=40 \mu\text{m}$	30

Figure 19. (a) Results of different structure lengths with different surface roughness.	
(b) The relationship between the contact angle hysteresis and the structure length.....	30

Figure 20. The measurement results of flat surface ($L=0$). (a) Contact angle hysteresis.	
(b) Radius of contact line versus droplet volume. (c) Line tension versus droplet volume. (d) Line tension versus radius of contact line.	32

Figure 21. The measurement results of $L=15\ \mu\text{m}$, $\lambda=1.33$ and $\kappa=1.37$. (a) Contact angle hysteresis. (b) Radius of contact line versus droplet volume. (c) Line tension versus droplet volume. (d) Line tension versus radius of contact line.	32
---	----

Figure 22. The measurement results of $L=15\ \mu\text{m}$, $\lambda=1.18$ and $\kappa=1.24$. (a) Contact angle hysteresis. (b) Radius of contact line versus droplet volume. (c) Line tension versus droplet volume. (d) Line tension versus radius of contact line.	33
---	----

Figure 23. The measurement results of $L=15\ \mu\text{m}$, $\lambda=1.12$ and $\kappa=1.18$. (a) Contact angle hysteresis. (b) Radius of contact line versus droplet volume. (c) Line tension versus droplet volume. (d) Line tension versus radius of contact line.	33
---	----

Figure 24. The measurement results of $L=15\ \mu\text{m}$, $\lambda=1.08$ and $\kappa=1.15$. (a) Contact angle hysteresis. (b) Radius of contact line versus droplet volume. (c) Line tension versus droplet volume. (d) Line tension versus radius of contact line.	34
---	----

Figure 25. The measurement results of $L=15\ \mu\text{m}$, $\lambda=1.06$ and $\kappa=1.12$. (a) Contact angle hysteresis. (b) Radius of contact line versus droplet volume. (c) Line	
---	--

tension versus droplet volume. (d) Line tension versus radius of contact line.
 34

Figure 26. The measurement results of $L=20\ \mu\text{m}$, $\lambda=1.33$ and $\kappa=1.37$. (a) Contact angle hysteresis. (b) Radius of contact line versus droplet volume. (c) Line tension versus droplet volume. (d) Line tension versus radius of contact line.
 35

Figure 27. The measurement results of $L=20\ \mu\text{m}$, $\lambda=1.18$ and $\kappa=1.24$. (a) Contact angle hysteresis. (b) Radius of contact line versus droplet volume. (c) Line tension versus droplet volume. (d) Line tension versus radius of contact line.
 35

Figure 28. The measurement results of $L=20\ \mu\text{m}$, $\lambda=1.12$ and $\kappa=1.18$. (a) Contact angle hysteresis. (b) Radius of contact line versus droplet volume. (c) Line tension versus droplet volume. (d) Line tension versus radius of contact line.
 36

Figure 29. The measurement results of $L=20\ \mu\text{m}$, $\lambda=1.08$ and $\kappa=1.15$. (a) Contact angle hysteresis. (b) Radius of contact line versus droplet volume. (c) Line tension versus droplet volume. (d) Line tension versus radius of contact line.
 36

Figure 30. The measurement results of $L=20\ \mu\text{m}$, $\lambda=1.06$ and $\kappa=1.12$. (a) Contact angle hysteresis. (b) Radius of contact line versus droplet volume. (c) Line tension versus droplet volume. (d) Line tension versus radius of contact line.
 37

Figure 31. The measurement results of $L=25\ \mu\text{m}$, $\lambda=1.33$ and $\kappa=1.37$. (a) Contact angle hysteresis. (b) Radius of contact line versus droplet volume. (c) Line

tension versus droplet volume. (d) Line tension versus radius of contact line.
 37

Figure 32. The measurement results of $L=25\ \mu\text{m}$, $\lambda=1.18$ and $\kappa=1.24$. (a) Contact angle hysteresis. (b) Radius of contact line versus droplet volume. (c) Line tension versus droplet volume. (d) Line tension versus radius of contact line.
 38

Figure 33. The measurement results of $L=25\ \mu\text{m}$, $\lambda=1.12$ and $\kappa=1.18$. (a) Contact angle hysteresis. (b) Radius of contact line versus droplet volume. (c) Line tension versus droplet volume. (d) Line tension versus radius of contact line.
 38

Figure 34. The measurement results of $L=25\ \mu\text{m}$, $\lambda=1.08$ and $\kappa=1.15$. (a) Contact angle hysteresis. (b) Radius of contact line versus droplet volume. (c) Line tension versus droplet volume. (d) Line tension versus radius of contact line.
 39

Figure 35. The measurement results of $L=25\ \mu\text{m}$, $\lambda=1.06$ and $\kappa=1.12$. (a) Contact angle hysteresis. (b) Radius of contact line versus droplet volume. (c) Line tension versus droplet volume. (d) Line tension versus radius of contact line.
 39

Figure 36. The measurement results of $L=30\ \mu\text{m}$, $\lambda=1.33$ and $\kappa=1.37$. (a) Contact angle hysteresis. (b) Radius of contact line versus droplet volume. (c) Line tension versus droplet volume. (d) Line tension versus radius of contact line.
 40

Figure 37. The measurement results of $L=30\ \mu\text{m}$, $\lambda=1.18$ and $\kappa=1.24$. (a) Contact angle hysteresis. (b) Radius of contact line versus droplet volume. (c) Line

tension versus droplet volume. (d) Line tension versus radius of contact line.

..... 40

Figure 38. The measurement results of $L=30\ \mu\text{m}$, $\lambda=1.12$ and $\kappa=1.18$. (a) Contact angle hysteresis. (b) Radius of contact line versus droplet volume. (c) Line tension versus droplet volume. (d) Line tension versus radius of contact line.

..... 41

Figure 39. The measurement results of $L=30\ \mu\text{m}$, $\lambda=1.08$ and $\kappa=1.15$. (a) Contact angle hysteresis. (b) Radius of contact line versus droplet volume. (c) Line tension versus droplet volume. (d) Line tension versus radius of contact line.

..... 41

Figure 40. The measurement results of $L=30\ \mu\text{m}$, $\lambda=1.06$ and $\kappa=1.12$. (a) Contact angle hysteresis. (b) Radius of contact line versus droplet volume. (c) Line tension versus droplet volume. (d) Line tension versus radius of contact line.

..... 42

Figure 41. The measurement results of $L=35\ \mu\text{m}$, $\lambda=1.33$ and $\kappa=1.37$. (a) Contact angle hysteresis. (b) Radius of contact line versus droplet volume. (c) Line tension versus droplet volume. (d) Line tension versus radius of contact line.

..... 42

Figure 42. The measurement results of $L=35\ \mu\text{m}$, $\lambda=1.18$ and $\kappa=1.24$. (a) Contact angle hysteresis. (b) Radius of contact line versus droplet volume. (c) Line tension versus droplet volume. (d) Line tension versus radius of contact line.

..... 43

Figure 43. The measurement results of $L=35\ \mu\text{m}$, $\lambda=1.12$ and $\kappa=1.18$. (a) Contact angle hysteresis. (b) Radius of contact line versus droplet volume. (c) Line

tension versus droplet volume. (d) Line tension versus radius of contact line.
 43

Figure 44. The measurement results of $L=35 \mu\text{m}$, $\lambda=1.08$ and $\kappa=1.15$. (a) Contact angle hysteresis. (b) Radius of contact line versus droplet volume. (c) Line tension versus droplet volume. (d) Line tension versus radius of contact line.
 44

Figure 45. The measurement results of $L=35 \mu\text{m}$, $\lambda=1.06$ and $\kappa=1.12$. (a) Contact angle hysteresis. (b) Radius of contact line versus droplet volume. (c) Line tension versus droplet volume. (d) Line tension versus radius of contact line.
 44

Figure 46. The measurement results of $L=40 \mu\text{m}$, $\lambda=1.33$ and $\kappa=1.37$. (a) Contact angle hysteresis. (b) Radius of contact line versus droplet volume. (c) Line tension versus droplet volume. (d) Line tension versus radius of contact line.
 45

Figure 47. The measurement results of $L=40 \mu\text{m}$, $\lambda=1.18$ and $\kappa=1.24$. (a) Contact angle hysteresis. (b) Radius of contact line versus droplet volume. (c) Line tension versus droplet volume. (d) Line tension versus radius of contact line.
 45

Figure 48. The measurement results of $L=40 \mu\text{m}$, $\lambda=1.12$ and $\kappa=1.18$. (a) Contact angle hysteresis. (b) Radius of contact line versus droplet volume. (c) Line tension versus droplet volume. (d) Line tension versus radius of contact line.
 46

Figure 49. The measurement results of $L=40 \mu\text{m}$, $\lambda=1.08$ and $\kappa=1.15$. (a) Contact angle hysteresis. (b) Radius of contact line versus droplet volume. (c) Line

tension versus droplet volume. (d) Line tension versus radius of contact line.
 46

Figure 50. The measurement results of $L=40\ \mu\text{m}$, $\lambda=1.06$ and $\kappa=1.12$. (a) Contact angle hysteresis. (b) Radius of contact line versus droplet volume. (c) Line tension versus droplet volume. (d) Line tension versus radius of contact line.
 47

Figure 51. The measurement results of $L=45\ \mu\text{m}$, $\lambda=1.33$ and $\kappa=1.37$. (a) Contact angle hysteresis. (b) Radius of contact line versus droplet volume. (c) Line tension versus droplet volume. (d) Line tension versus radius of contact line.
 47

Figure 52. The measurement results of $L=45\ \mu\text{m}$, $\lambda=1.18$ and $\kappa=1.24$. (a) Contact angle hysteresis. (b) Radius of contact line versus droplet volume. (c) Line tension versus droplet volume. (d) Line tension versus radius of contact line.
 48

Figure 53. The measurement results of $L=45\ \mu\text{m}$, $\lambda=1.12$ and $\kappa=1.18$. (a) Contact angle hysteresis. (b) Radius of contact line versus droplet volume. (c) Line tension versus droplet volume. (d) Line tension versus radius of contact line.
 48

Figure 54. The measurement results of $L=45\ \mu\text{m}$, $\lambda=1.08$ and $\kappa=1.15$. (a) Contact angle hysteresis. (b) Radius of contact line versus droplet volume. (c) Line tension versus droplet volume. (d) Line tension versus radius of contact line.
 49

Figure 55. The measurement results of $L=45\ \mu\text{m}$, $\lambda=1.06$ and $\kappa=1.12$. (a) Contact angle hysteresis. (b) Radius of contact line versus droplet volume. (c) Line

tension versus droplet volume. (d) Line tension versus radius of contact line.

..... 49

Figure 56. The measurement results of $L=50\ \mu\text{m}$, $\lambda=1.33$ and $\kappa=1.37$. (a) Contact angle hysteresis. (b) Radius of contact line versus droplet volume. (c) Line tension versus droplet volume. (d) Line tension versus radius of contact line.

..... 50

Figure 57. The measurement results of $L=50\ \mu\text{m}$, $\lambda=1.18$ and $\kappa=1.24$. (a) Contact angle hysteresis. (b) Radius of contact line versus droplet volume. (c) Line tension versus droplet volume. (d) Line tension versus radius of contact line.

..... 50

Figure 58. The measurement results of $L=50\ \mu\text{m}$, $\lambda=1.12$ and $\kappa=1.18$. (a) Contact angle hysteresis. (b) Radius of contact line versus droplet volume. (c) Line tension versus droplet volume. (d) Line tension versus radius of contact line.

..... 51

Figure 59. The measurement results of $L=50\ \mu\text{m}$, $\lambda=1.08$ and $\kappa=1.15$. (a) Contact angle hysteresis. (b) Radius of contact line versus droplet volume. (c) Line tension versus droplet volume. (d) Line tension versus radius of contact line.

..... 51

Figure 60. The measurement results of $L=50\ \mu\text{m}$, $\lambda=1.06$ and $\kappa=1.12x$. (a) Contact angle hysteresis. (b) Radius of contact line versus droplet volume. (c) Line tension versus droplet volume. (d) Line tension versus radius of contact line.

..... 52

Figure 61. Top-view images, taken with scanning electron microscopy, of the micro-hills and nano-folds on: (a) the cavities in the parylene mold, (b) the Azo-IPN artificial petal..... 54

Figure 62. Top-view images, taken with scanning electron microscopy of real rose petal.....	55
Figure 63. Schematic transition of trans-cis isomerization on the surface of the Azo-IPN artificial petal.....	55
Figure 64. Temporal evolution of the absorbance spectrum of the artificial Azo-IPN petal under the exposure of (a) UV light and (b) green light.	58
Figure 65. Comparison of the measured contact angle hysteresis θ_h on (a) a real rose.	58
Figure 66. Top-view images, taken with laser confocal microscope: (a) without exposure, (b) UV light (365 nm wavelength, 15 mW/cm ²), (c) green light (530 nm wavelength, 20 mW/cm ²), (d) 3D image display of Azo-IPN film.	59
Figure 67. Top-view images, taken with scanning electron microscopy: (a) without exposure, (b) UV light (365 nm wavelength, 15 mW/cm ²), (c) green light (530 nm wavelength, 20 mW/cm ²)	59
Figure 68. FTIR of Azo-IPN film after different light exposure	61
Figure 69. Cyclic variation of the contact angle hysteresis by alternating the wavelength of the exposure light.....	62
Figure 70. Reversible tenability of the degree of petal effect of a fabricated Azo-IPN petal after exposure to light of various wavelengths. (a) After exposure to UV light (365 nm wavelength, 15 mW/cm ² intensity) for 3 minutes. (b) After exposure to green light (530 nm wavelength, 20 mW/cm ² intensity) for 3 minutes.....	63
Figure 71. Schematic view of the surface.....	66

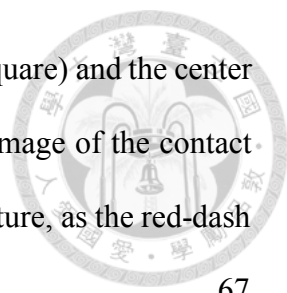


Figure 72. (a) The image of the characteristic structure (red-dash square) and the center of the contact line of the droplet (green spot). (b) The image of the contact line of the droplet. A square means a characteristic structure, as the red-dash square. 67

Figure 73. Illustration of moving contact line on a textured surface. 69


Tables

Table 1. Measured contact angle of DI water on textured surfaces.....	22
Table 2. Measured contact angle hysteresis of DI water on textured surfaces.....	24
Table 3. Measured contact angle and contact angle hysteresis of deionized water on artificial petal of Azo-IPN film.	61
Table 4. Surface roughness (λ) for different DR	66
Table 5. The numbers of different ratios of 45 sections for $DR=1$:.....	67
Table 6. The ratio of actual length of the three-phase contact line to the apparent (κ) for different DR	67

Nomenclature



Symbol	Description
γ	Surface free energy
T	Temperature
P	Pressure
V	Volume
μ	Chemical potential
W	Free energy
A	Area of interface
L	Length
W_{sl}	Free energy of solid-liquid phase
W_{sv}	Free energy of solid-vapor phase
W_{lv}	Free energy of liquid-vapor phase
W_{τ}	Free energy of three-phase contact line
A_{sl}	Smooth interface area of solid-liquid phase
A_{sv}	Smooth interface area of solid-vapor phase
A_{lv}	Smooth interface area of liquid-vapor phase
L_{τ}	Smooth length of three-phase contact line
γ_{sl}	Surface tension of solid-liquid phase
γ_{sv}	Surface tension of solid-vapor phase
γ_{lv}	Surface tension of liquid-vapor phase
τ	Line tension of three-phase contact line
θ	Contact angle



r	Base radius of the droplet
a_{sl}	Rough interface area of solid-liquid phase
a_{sv}	Rough interface area of solid-vapor phase
a_{lv}	Rough interface area of liquid-vapor phase
l_r	Rough length of three-phase contact line
λ	Surface roughness
κ	ratio of actual length of the three-phase contact line to the apparent
G	Gibbs free energy
R	Radius of the droplet
A_{all}	Area of all interface
G^*	Normalized Gibbs free energy

.Chapter 1 Introduction

1.1 Motivation



Wetting behavior is a common phenomenon and numerous researchers want to know how to use it to improve the life. The lotus effect and petal effect are two special cases. Both of them are hydrophobic, but they have opposite degree on the contact angle hysteresis. Petal effect has high contact angle hysteresis, and it will pin the droplet on the surface. Although it has been studied for a long time, contact angle hysteresis have not been well understood. The original Young, Cassie-Baxter and Wenzel equations are not enough to explain. There are two main characters, surface roughness and surface energy, affect the hysteresis. In this research, we introduce the line tension to modified the Wenzel equation to find the effect of surface roughness. We found that the surface roughness is not the key role, and the characteristic length and the ratio of actual length of the three-phase contact line to the apparent are more important. By knowing these two characters, we can design the particular contact angle hysteresis.

And we also found out that the photoisomer, azobenzene, can effectively control the hysteresis under various wavelength light irradiation. The difference of surface energy between tran and cis azobenzene strongly affect the behavior of hysteresis. The artificial petal created by azobenzene present the sliding drops under the exposure of UV and green light.

Contact angle hysteresis is an important physical phenomenon. To clarify this, starting from the basic definition of contact angle hysteresis by adding line tension, we not only explain the key role, but also use the artificial azobenzene petal to control it. This research can approve the industrial applications such as sliding drops, coffee stains phenomenon, curtain, ink-jet printing and wire coating techniques.

1.2 Literature Survey

1.2.1. Line tension



Contact angle hysteresis (CAH) is one of the most important and classic elements of wetting of liquid droplets in systems from centimeter to micrometer scales. It can be intuitively understood by looking at a droplet resting on a horizontal substrate. If the substrate is tilted, the droplet would want to move down by the pulling of gravity. However, the CAH will pin the droplet on the substrate. Under this condition, the droplet will become asymmetric but will not move. The top of the droplet will become thin and the contact angle will become smaller, while the bottom will become thick and the contact angle will become larger. When the droplet reaches a specific size, the droplet slides down the substrate, and the difference between the larger and smaller contact angle is called the hysteresis [1]. For its great value, many scientists have studied hysteresis to give the theoretical understanding of the retention forces on droplets sticking to solid surfaces [3], [7]-[9].

For knowing the wetting behavior better, the line tension becomes particularly important. The line tension is defined as the excess free energy of a solid-liquid-vapor system per unit length of the three-phase contact line. In 2013, Edward Bormashenko and Gene Whyman found out the role of line tension in the stability of Cassie-Wenzel wetting [10]. As Figure 1, The effect of line tension may increase or decrease the potential barrier separating the Cassie and the Wenzel wetting states, depending on the sign of the line tension and the topography of a relief. The formation of the barrier separating the Cassie and Wenzel wetting states on reentrant topographies, which demonstrate pronounced superhydrophobicity and superoleophobicity, is treated. In spite of the fact that the line tension is regarded as a weak effect, it may be essential for

stabilizing (destabilizing) the Cassie wetting. The effect may be crucial to understanding the stability of the Cassie-like wetting of inherently hydrophilic nanoscaled reliefs.

Yawei Liu et al. modified the Young equation by line tension to confirm the viability of Young equation [11]. They present a theoretical method to determine the line tension of nanodroplets on homogeneous substrates via decomposing the grand free energy into volume, interface and line contributions. Figure 2 shows the obtained line energy τL as a function of the droplet circumference for different values of ε_{sf} . Good linear relationships are observed from this figure, indicating that the line tension is chemical potential independent, namely the line tension can be treated as a constant at a fixed temperature and fluid-solid interaction. Moreover, it also shows that the line tension is always negative, and reaches a minimal value at $\varepsilon_{sf} = 0.50$.

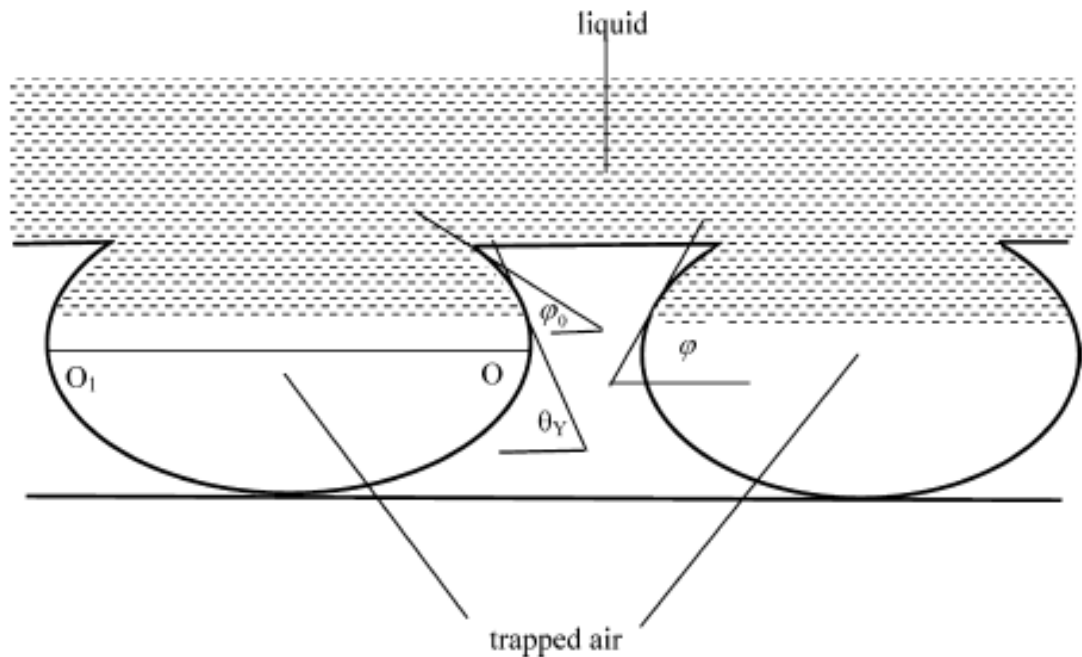


Figure 1. Geometrical air trapping on a hydrophilic relief with re-entrant topography; φ is the angle corresponding to the current liquid level, φ_0 is the angle corresponding to the initial liquid level, θ_Y is the Young angle [10].

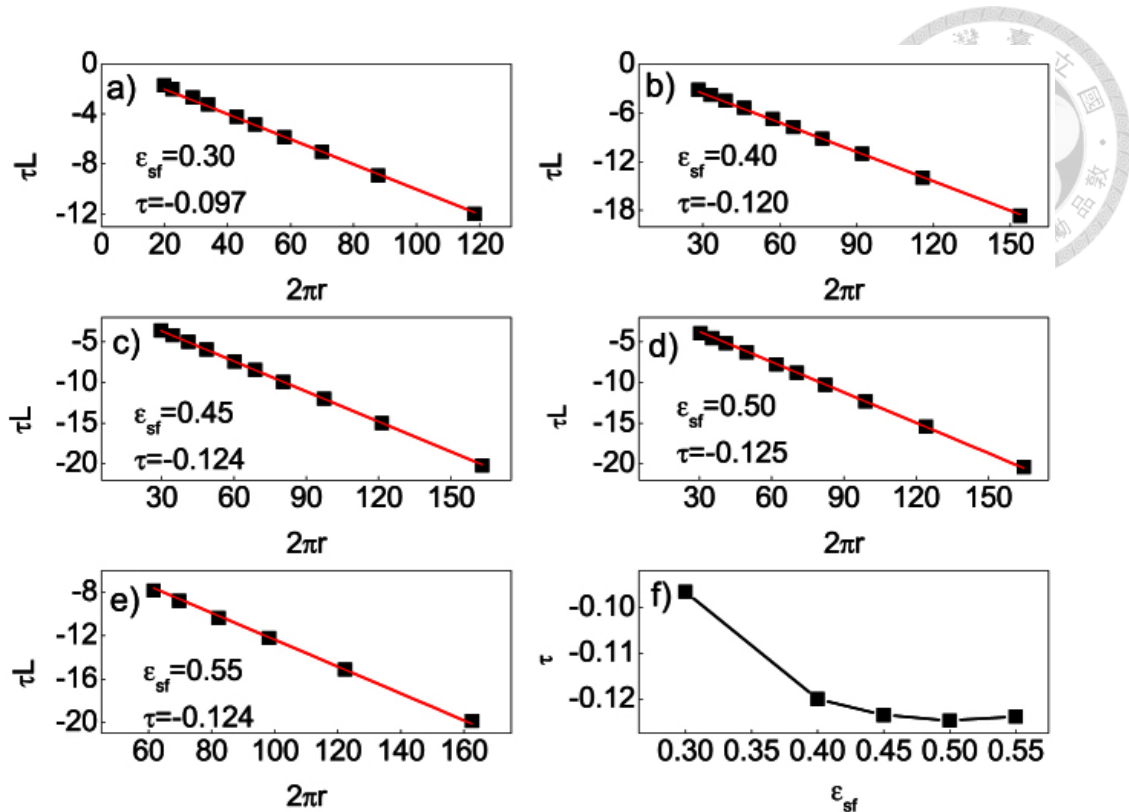


Figure 2. The determination of contact line tension. (a-e) The contact line energy τL versus the droplet circumference $2\pi r$ at different fluid-solid interaction strengths of ϵ_{sf} . (f) The obtained contact line tension τ versus the fluid-solid interaction ϵ_{sf} [11].

1.2.2. Azobenzene in interpenetrating polymer networks

During the past decade, an increasing interest in azobenzene dye has emerged. Azobenzene is a powerful material and it is conformable to incorporation into a wide variety of materials [12]. Azobenzene is a chemical compound consisting of two phenyl rings linked by an azo bond ($N=N$) and it is also a photosensitive mesogenic molecule that changes from a rod-like shape to a kinked shape upon irradiation at 365nm Ultraviolet (UV) light. One of the most interesting properties of azobenzene is the photoisomerization of trans and cis isomer [13]-[16]. These two isomers can be switched by a particular wavelength of light, as shown in Figure 3.

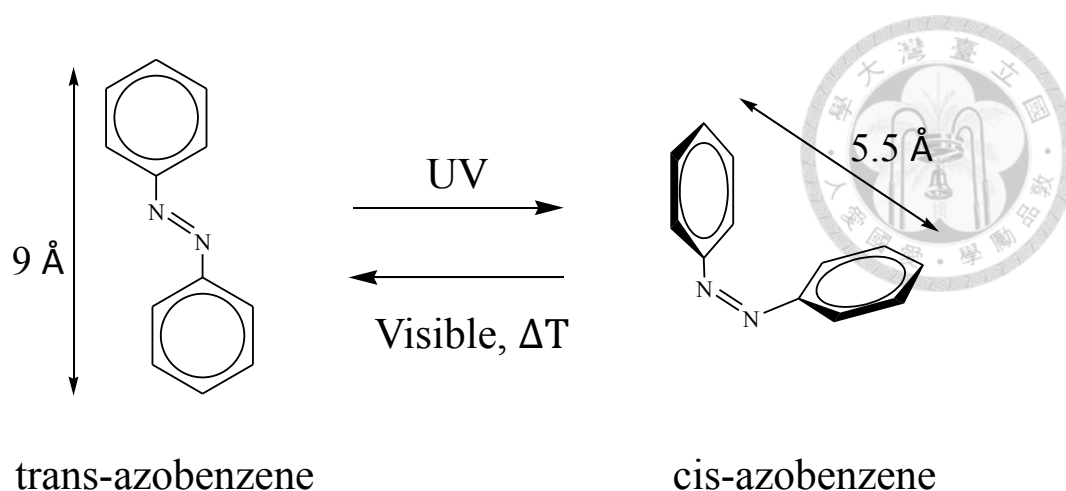


Figure 3. The photo-isomerization of azobenzene compounds.

The trans isomer of azobenzene is generally more stable than the cis isomer of azobenzene, but each isomer can be easily converted to each other by light irradiation of appropriate wavelength. As shown in Figure 3, trans isomer of azobenzene can be transformed to cis isomer of azobenzene by rotating or inverting a phenyl ring through the excitation with ultraviolet light which corresponds to the energy gap of the $\pi\text{-}\pi^*$ state for trans-to-cis conversion. In the same way, cis isomer of azobenzene can be reversely transformed to trans isomer of azobenzene through the excitation with green light which is equivalent to the energy gap of the $n\text{-}\pi^*$ state for trans-to-cis conversion or thermally stimulated.

In general, the two mechanisms of the trans-cis reaction are frequently discussed in research. The first mechanism is known as the rotation mechanism. When trans isomer of azobenzene was irradiated ultraviolet light, the $\text{N}=\text{N}$ double bond of trans isomer of azobenzene is opened and allowed the free rotation of one of the phenyl ring around the N-N axis. As shown in Figure 3, the trans isomer of azobenzene which is planar will change to the cis isomer of azobenzene which is three dimensional [16].

Miguel Camacho-Lopez et al. used the azobenzene and methylsiloxane to create the liquid-crystal elastomers [17]. This rubber can reversibly change its shape quickly, in

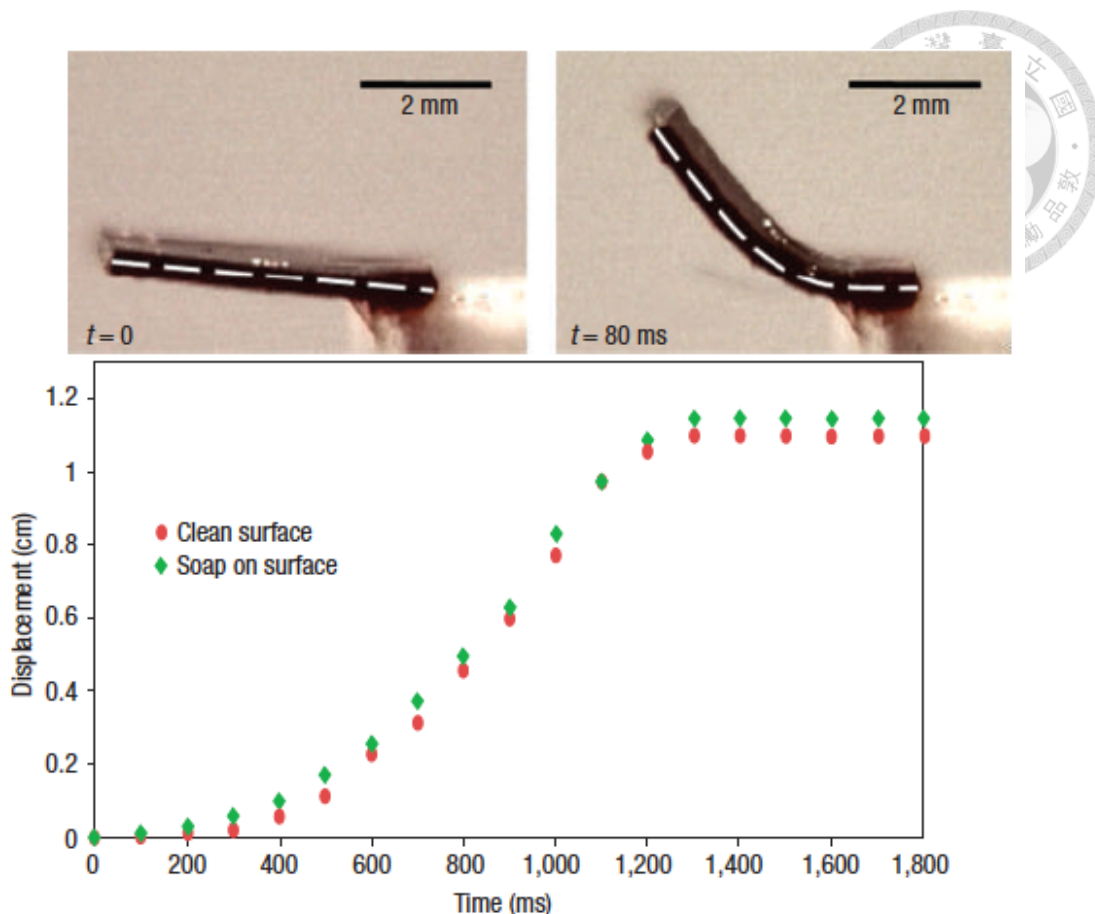


Figure 4. The optomechanical response of an LCE sample. Two frames from a video clip recording the bending and relaxation dynamics of the sample. The measured displacement of the LCE sample center from its initial rest position as a function of time from onset of illumination [17].

Figure 4. They demonstrated the rubber by dissolving, rather than covalently bonding, azobenzene dye into an LCE sample, its mechanical deformation in response to non-uniform illumination by visible light becomes very large and is more than two orders of magnitude faster than previously reported. Rapid light-induced deformations allow LCEs to interact with their environment in new and unexpected ways.

Hyun-Kyoung Kim et al. used a special way, semi-interpenetrating polymer network, to combine the azobenzene with other material, as the Figure 5 shows [18]. The method of interpenetrating polymer networks represents a unique class of materials in which two

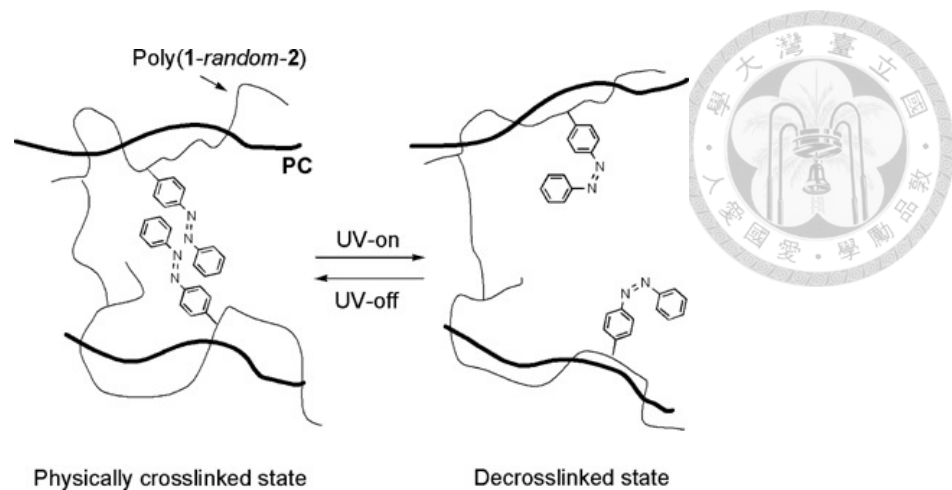


Figure 5. Model for the UV-induced change in the elasticity [18].

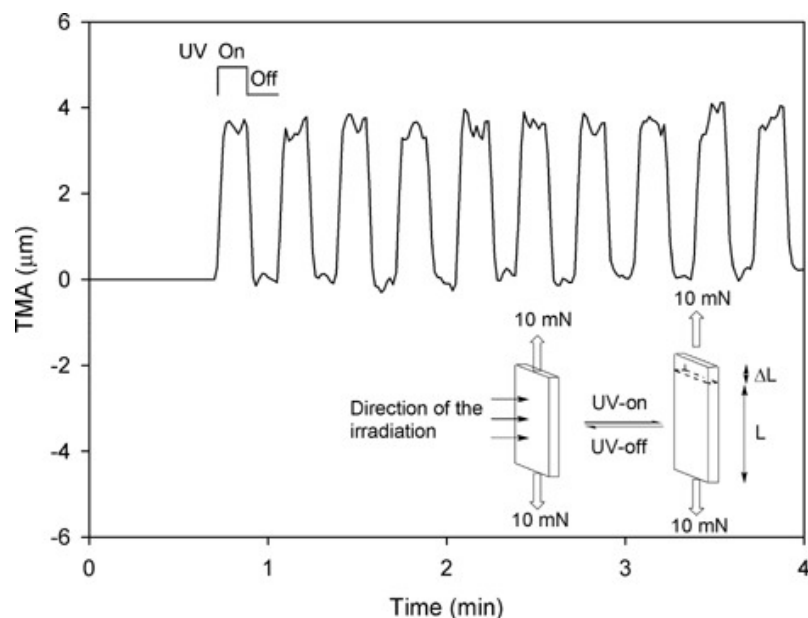


Figure 6. The reversible UV response of the length of the semi-IPN film at 25°C [18].

crosslinked polymers are held together by permanent topological entanglements [19]-[20]. From Figure 6, the semi-IPN film showed reversible deformation upon switching the UV irradiation on and off and responded with unprecedented rapidity. The photomechanical effect is attributed to a reversible change between the highly aggregated and dissociated states of the azobenzene groups.

Yizhong Huang et al. used the azobenzene to change the contact angle [21]. In Figure 8, the azobenzene moieties of azo-HPCs exhibited a reversible cis-to-trans isomerization

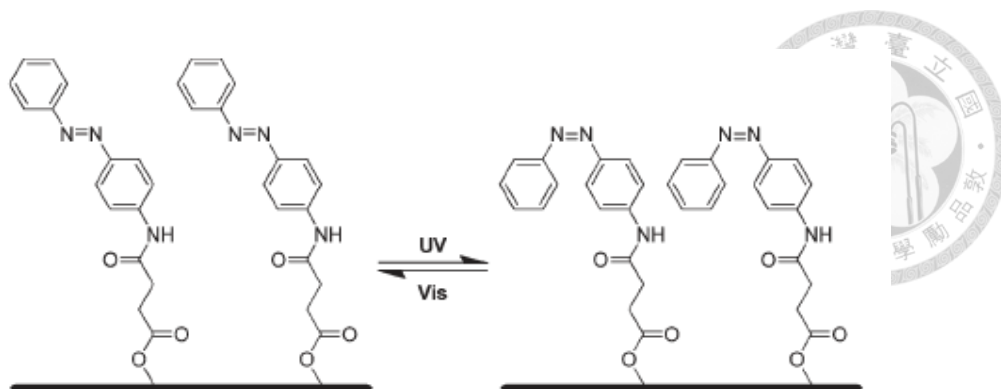


Figure 7. Photoisomerization of azobenzene moieties in the surface of the azo-HPC films [21].

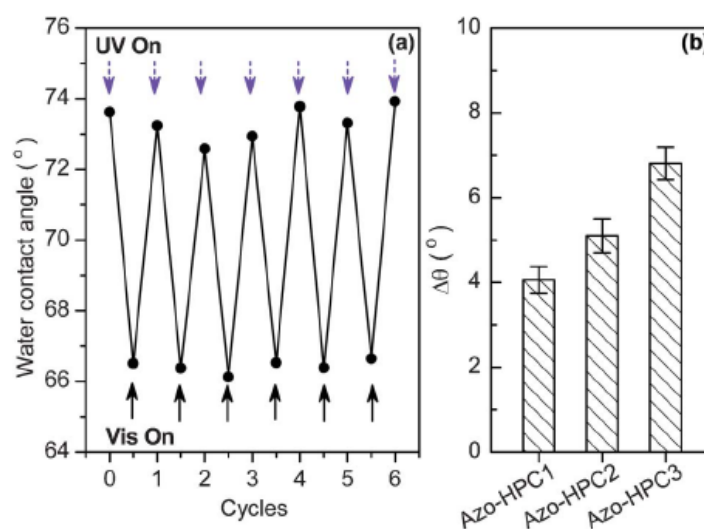


Figure 8. (a) The changes of contact angle of the azo-HPC3 film over several cycles of irradiation with UV light ($\lambda = 365$ nm) for 20 min and subsequently with visible light ($\lambda > 420$ nm) for 25 min. (b) The variation of the contact angle ($\Delta\theta$) of the azo-HPCs upon irradiation by UV and subsequently by visible light under the conditions of (a) [21].

transition upon irradiation with UV and visible light in both solution and solid state. The reversible trans-to-cis photoisomerization led to a change of the wettability of the azo-HPC films. Surface energy estimations suggest that tunable film wettability was attributed to the change of the dipole moment of the azobenzene moieties in the film surface.

.Chapter 2 Wetting behavior theories

2.1 Introduction



Wetting phenomena on a solid surface play an important role in many phase separation processes, for example, bitumen separation from tar sand, wetting and flotation of particles, agglomeration of solid particles by dispersed liquids, painting, printing, impregnation of textiles, and in many other areas of technology. Although significant developments in the theory of wetting process have occurred in recent years, the understanding of these phenomena is not complete.

Surface energy and surface roughness are two main factors to control the wetting behavior. Understanding the relation can help to design and optimize the textured surface. The theoretical explanation for the wetting phenomena has been offered by Young, Cassie and Wenzel for more than 70 years. In this chapter, for knowing the petal-effect, the line tension will be introduced to modified Young's and Wenzel's equation for a complete understanding of the wetting behavior and analyzing the experiments. The Gibbs free energy of Wenzel state is also presented to know the contact angle hysteresis more.

Only the simplest three-phase system being in thermodynamic equilibrium is considered with these following assumptions:

- ◆ the surface free energy (γ) is constant and independent of drop size
- ◆ this system is simplified to a spherical liquid droplet resting on the homogeneous, horizontal flat solid surface
- ◆ The temperature (T), pressure (P), volume (V), composition and chemical potential (μ) are constant.

2.2 Modified Young equation

In this chapter, the theoretical models of the wetting behavior are modified by line tension to improve the correction of the relationships between the roughness, contact angle, and contact angle hysteresis. The Young equation describes a force balance in the plane of the solid surface for three-phase systems in which the equilibrium contact angle is establish in order to resolve the interfacial tensions. This modified Young equation based on thermodynamic considerations is presented below.

The general model for the Young's equation is expressed like Figure 9. The free energy relations of three-phase system can be expressed as follows:

$$dW = \sum_i \frac{\partial W_i}{\partial A_i} dA_i + \sum_j \frac{\partial W_j}{\partial L_j} dL_j$$

$$dW = \frac{\partial W_{sl}}{\partial A_{sl}} dA_{sl} + \frac{\partial W_{sv}}{\partial A_{sv}} dA_{sv} + \frac{\partial W_{lv}}{\partial A_{lv}} dA_{lv} + \frac{\partial W_{\tau}}{\partial L_{\tau}} dL_{\tau} \quad (2. 1)$$

where W is the free energy, A is the area of flat surface, L is the length of the three-phase contact line; and the subscripts, s , l , v , correspond to solid, liquid, and vapor, so the A_{sl} means the interface area of solid-liquid phase, A_{sv} means the interface area of solid-vapor phase, and A_{sl} means the interface area of liquid-vapor phase. The eq (2. 1) can also be presented by dividing by dA_{sl} .

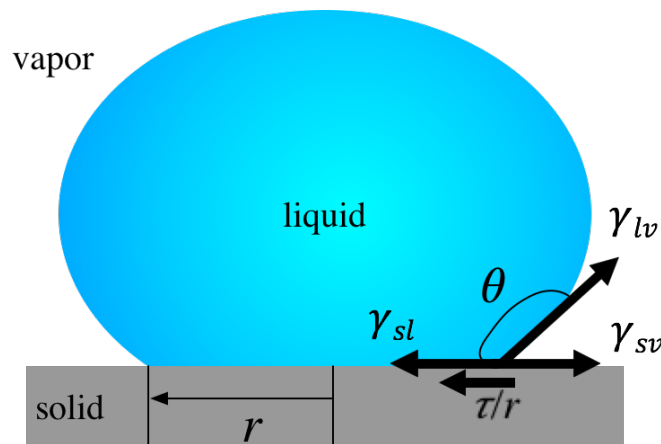
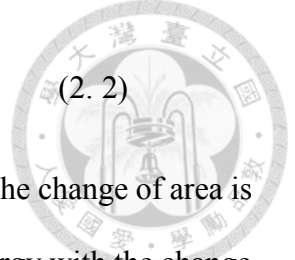


Figure 9. Droplet in contact with a flat solid surface.



$$\frac{dW}{dA_{sl}} = 0 = \frac{\partial W_{sl}}{\partial A_{sl}} + \frac{\partial W_{sv}}{\partial A_{sv}} \frac{dA_{sv}}{dA_{sl}} + \frac{\partial W_{lv}}{\partial A_{lv}} \frac{dA_{lv}}{dA_{sl}} + \frac{\partial W_{\tau}}{\partial L_{\tau}} \frac{dL_{\tau}}{dA_{sl}} \quad (2.2)$$

From this equation, the change of free energy corresponding to the change of area is the surface free energy (surface tension, γ), so the change of free energy with the change in the contact line can lead to the line free energy (line tension, τ) as shown below:

$$\frac{\partial W_{sl}}{\partial A_{sl}} = \gamma_{sl}$$

$$\frac{\partial W_{sv}}{\partial A_{sv}} = \gamma_{sv}$$

$$\frac{\partial W_{lv}}{\partial A_{lv}} = \gamma_{lv}$$

$$\frac{\partial W_{\tau}}{\partial L_{\tau}} = \tau$$

the following substitutions are effective under the conditions, θ is the contact angle, and the r is the base radius of the droplet.

$$dA_{sl} = -dA_{sv}$$

$$dA_{lv} = dA_{sl} \cos \theta$$

$$\frac{dL_{\tau}}{dA_{sl}} = \frac{1}{r}$$

Therefore, the modified equation (2.2) can be shown as:

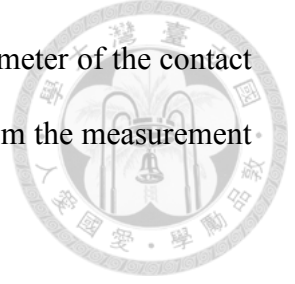
$$\cos \theta = \frac{\gamma_{sv} - \gamma_{sl}}{\gamma_{lv}} - \frac{\tau}{r\gamma_{lv}} \quad (2.3)$$

$$\cos \theta = \cos \theta^* - \frac{\tau}{r\gamma_{lv}} \quad (2.4)$$

Then, it is the modified Young's equation. The θ^* is the intrinsic contact angle, which is the contact angle for the original Young's equation.

The general equation was derived by Boruvka and Neumann in 1977 like: [22]

$$\gamma_{sv} - \gamma_{sl} = \gamma_{lv} \cos \theta + \gamma_{slv} \kappa_{gs}$$



Where the γ_{slv} is the line tension, τ , and the κ_{gs} is the geometric parameter of the contact line, which can be seen as the $1/r$. The line tension can be found from the measurement of contact angle and the radius of droplet by eq (2. 4).

2.3 Modified Wenzel equation

For rough solid surface, Wenzel followed the Young's equation by adding the roughness on the flat surface. Similar to the Young, Wenzel did not predict the effect of line free energy in the contact angle analysis. Consider the same thermodynamic consideration of three-phase system, and the Wenzel equation can be modified with the line tension term.

Figure 10a illustrates a droplet on a rough solid surface without air trapped at the liquid-solid interface. The wettability of this droplet can be described by the Wenzel's model.⁷ The modified Wenzel's equation, which relates the apparent contact angle, θ , for a droplet on a rough solid surface to the line tension, τ , is

$$dW = \frac{\partial W_{sl}}{\partial a_{sl}} da_{sl} + \frac{\partial W_{sv}}{\partial a_{sv}} da_{sv} + \frac{\partial W_{lv}}{\partial a_{lv}} da_{lv} + \frac{\partial W_{\tau}}{\partial l_{\tau}} dl_{\tau} \quad (2. 5)$$

Where W is the free energy, a is the area of rough surface, l is the length of the three-phase contact line; and the subscripts, s , l , v , correspond to solid, liquid, and vapor, so the

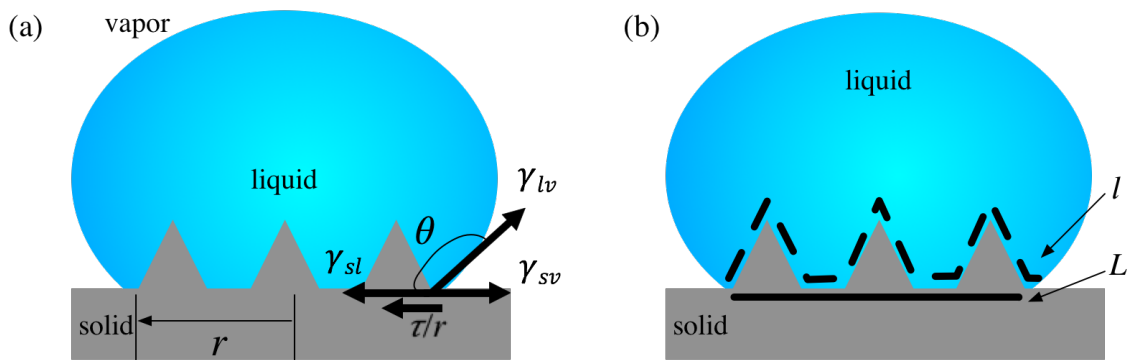


Figure 10. (a) Droplet in contact with rough solid surface. (b) l is the actual length of contact line; L is the apparent length.

a_{sl} means the interface area of solid-liquid phase, a_{sv} means the interface area of solid-vapor phase, and a_{sl} means the interface area of liquid-vapor phase.

Then, the eq (2. 5) is divided by apparent area which is the area of flat surface, dA_{sl} .

$$\frac{dW}{dA_{sl}} = \frac{\partial W_{sl}}{\partial a_{sl}} \frac{da_{sl}}{dA_{sl}} + \frac{\partial W_{sv}}{\partial a_{sv}} \frac{da_{sv}}{dA_{sl}} + \frac{\partial W_{lv}}{\partial a_{lv}} \frac{da_{lv}}{dA_{sl}} + \frac{\partial W_{\tau}}{\partial l_{\tau}} \frac{dl_{\tau}}{dL_{\tau}} \frac{dL_{\tau}}{dA_{sl}} \quad (2. 6)$$

The definitions of surface free energy (surface tension, γ) and line free energy (line tension, τ) used in eq (2. 2) are still valid for eq (2. 6).

$$\frac{\partial W_{sl}}{\partial a_{sl}} = \gamma_{sl}$$

$$\frac{\partial W_{sv}}{\partial a_{sv}} = \gamma_{sv}$$

$$\frac{\partial W_{lv}}{\partial a_{lv}} = \gamma_{lv}$$

$$\frac{\partial W_{\tau}}{\partial l_{\tau}} = \tau$$

For Wenzel system, the following substitutions can also be used, θ is the contact angle, and the r is the base radius of the droplet. There are two new parameters, surface roughness, λ , and the ratio of actual length of the three-phase contact line to the apparent, κ .

$$\frac{dA_{sv}}{dA_{sl}} = -1$$

$$\frac{da_{lv}}{dA_{lv}} = 1$$

$$\frac{dA_{lv}}{dA_{sl}} = \cos \theta$$

$$\frac{dL_{\tau}}{dA_{sl}} = \frac{1}{r}$$

$$\frac{da_{sl}}{dA_{sl}} = \frac{da_{sv}}{dA_{sv}} = \lambda$$

$$\frac{dl_{\tau}}{dL_{\tau}} = \kappa$$

So, the modified Wenzel is like:



$$\cos \theta = \lambda \cos \theta^* - \frac{\tau}{\gamma_{lv}} \kappa \frac{1}{r} \quad (2.7)$$

If the surface is flat, the λ and κ both equal to 1. Under this circumstance, eq (2.7) becomes the modified Young's equation, eq (2.4).

2.4 Modified Gibbs free energy of Wenzel's model

In this research, we experimentally characterize the line tension on micromachined surfaces and discuss its effect on the CA hysteresis. Particularly, the liquid-solid interaction that can be modeled by the modified Wenzel's equation is investigated. In addition, the Gibbs free energy is also introduced to evaluate the influence of line tension. By taking the line tension into account, the Gibbs free energy is

$$G = \gamma_{lv} a_{lv} + \gamma_{sl} a_{sl} + \gamma_{sv} a_{sv} + \tau l_{\tau} \quad (2.8)$$

where a is the area with the subscript 'sl' for the solid-liquid, 'sv' for the solid-vapor, and 'lv' for the liquid-vapor interface, respectively; l is the length of contact line. The following calculations can help to explain eq (2.8).

$$a_{lv} = 2\pi R^2 (1 - \cos \theta)$$

$$a_{sl} = \lambda \pi R^2 \sin^2 \theta$$

$$a_{sv} = A_{all} - \lambda \pi R^2 \sin^2 \theta$$

$$l_{\tau} = 2\kappa \pi R \tau \sin \theta$$

The R is the radius of droplet and set the A_{all} equal 0 to simplify the equation.

$$G = \gamma_{lv} [2\pi R^2 (1 - \cos \theta)] + \gamma_{sl} (\lambda \pi R^2 \sin^2 \theta) + \gamma_{sv} (-\lambda \pi R^2 \sin^2 \theta) + 2\kappa \pi R \tau \sin \theta$$

or

$$G = \lambda \pi R^2 \sin^2 \theta (\gamma_{sl} - \gamma_{sv}) + \gamma_{lv} [2\pi R^2 (1 - \cos \theta)] + 2\kappa \pi R \tau \sin \theta \quad (2.9)$$

For general analyzing, the Gibbs free energy can be further normalized. The volume of droplet is introduced to replace the R .



$$V = \frac{\pi R^3}{3} (1 - \cos \theta)^2 (2 + \cos \theta) \Rightarrow R^2 = \left(\frac{3V}{\pi} \right)^{\frac{2}{3}} \left[(1 - \cos \theta)^2 (2 + \cos \theta) \right]^{\frac{2}{3}}$$

Take it into eq (2. 9)

$$G = \pi \left(\frac{3V}{\pi} \right)^{\frac{2}{3}} \left[(1 - \cos \theta)^2 (2 + \cos \theta) \right]^{\frac{2}{3}} \left[\lambda \sin^2 \theta (\gamma_{SL} - \gamma_{SV}) + 2(1 - \cos \theta) \gamma_{LV} \right] \\ + 2\kappa\pi \left(\frac{3V}{\pi} \right)^{\frac{1}{3}} \left[(1 - \cos \theta)^2 (2 + \cos \theta) \right]^{\frac{1}{3}} \tau \sin \theta$$

Then, this equation can be

$$G^* = \frac{G}{\sqrt[3]{9V^2\pi\gamma_{LV}}} = \frac{2 - \lambda \cos \theta^* (1 + \cos \theta)}{\left[(1 - \cos \theta) (2 + \cos \theta)^2 \right]^{\frac{1}{3}}} + \frac{2\kappa\tau}{\sqrt[3]{\frac{3V}{\pi}\gamma_{LV}}} \frac{\sin \theta}{\left[(1 - \cos \theta)^2 (2 + \cos \theta) \right]^{\frac{1}{3}}} \quad (2. 10)$$

This equation is the modified of hysteresis process, but this approach neglects the pressure and the interaction between the solid and liquid and are valid under fine structure which means much smaller than droplet. The strength of hysteresis can be calculated by the surface roughness (λ), so we can know how to design the right surface with excellent characteristic if we know the contact angle at smooth surface.

Now, the sign of ΔG^* indicates the direction of a chemical reaction and determine if a reaction is spontaneous or not.

- ◆ $\Delta G^* < 0$: reaction is spontaneous in the direction written
- ◆ $\Delta G^* = 0$: the system is at equilibrium and there is no net change either in forward or reverse direction.
- ◆ $\Delta G^* > 0$: reaction is not spontaneous and the process proceeds spontaneously in the reserve direction. To drive such a reaction, the system needs to be inputted enough free energy.

.Chapter 3 Evolution of three-phase line tension on petal-like contact angle hysteresis



3.1 Introduction

In nature, all primary parts of plants are covered by a cuticle that interfaces with environment. In most cases, the cuticle forms a hydrophobicity surface [23, 24]. In particular, the lotus leaves have ultra-hydrophobic surfaces and self-cleaning properties which are known as the “lotus effect” [25, 26]. The contact angle (CA) of water droplet on the surface is large ($\sim 160^\circ$), and the CA hysteresis is very small (usually $< 10^\circ$). On the other hand, rose petals also show super-hydrophobic with CA as large as 151° , but the droplet will be pinned by the surface and presents higher CA hysteresis ($40\text{--}50^\circ$) which is referred to as “petal effect” [27]. These two effect are separated into early Cassie-Baxter and Wenzel models by the size of structure [28, 29]; from these models, there are two regimes of wetting on a rough surface: a homogeneous regime with solid-water interface and a composite regime with a three-phase solid-water-vapor interface. Wetting on rough surfaces is a complex problem which has attracted significant attention from investigation [28–42]. These models were modified by line tension which was first introduced by Gibbs to be more general [43–46]. The line tension is defined as the excess free energy of a three-phase solid-liquid-vapor system per unit length of contact line [47, 48]. However, it remains controversial largely because the direct measurement of the line tensions of droplets has not been possible [49–52]. The experimental values in the literature range over 7 orders of magnitude from 10^{-12} to 10^{-5} J/m, and both positive and negative line tensions were reported [49, 52–54]. A positive line tension operates to constrict the length of the three-phase line, whereas the negative tends to expand it; it means that the line tension will try to pin the contact line and to impede the motion of the droplet.

Hysteresis is the phenomenon that the droplet is pinned on the surface when it attempts to move, but the role of the line tension in hysteresis has not been well understood.

Figure 11a illustrates a droplet on a rough solid surface without air trapped at the liquid-solid interface. The wettability of this droplet can be described by the Wenzel's model.⁷ The modified Wenzel's equation, which relates the apparent contact angle, θ , for a droplet on a rough solid surface to the line tension, τ , is [49, 55]

$$\cos \theta = \lambda \cos \theta^* - \kappa \frac{\tau}{\gamma_{lv} r} \quad (2.7)$$

with γ_{lv} the liquid-vapor interface tension, τ the line tension, r the base radius of contact area, and θ^* the intrinsic contact angle. λ is the ratio of actual interfacial area to the apparent area of the geometrical interface. κ is the ratio of actual length of the three-phase contact line to the apparent. If the surface is flat, the λ and κ both equal to 1. Under this circumstance, eq 1 becomes the modified Young's equation: [48, 49, 55]

$$\cos \theta = \cos \theta^* - \frac{\tau}{\gamma_{lv} r} \quad (2.4)$$

which indicates that the line tension should vanish when the droplet is at static equilibrium. When the droplet attempts to move, its contact with the solid substrate is described by the advancing (θ_A) and receding angle (θ_R), respectively. These angles are affected by the line tension according to eq (2.7), implying that the line tension plays a role in the contact angle hysteresis.

The advancing and receding angles are the maximum and minimum CA, respectively. Experimentally, these angles can be measured by increasing or decreasing the volume of the droplet (Figure 11b), and the CA hysteresis (θ_H) can be evaluated by

$$\theta_H = \theta_A - \theta_R \quad (3.1)$$

The static, advancing and receding states of the droplet give different line tensions according to eq (2.7). In addition, the effect of line tension can be modulated with design

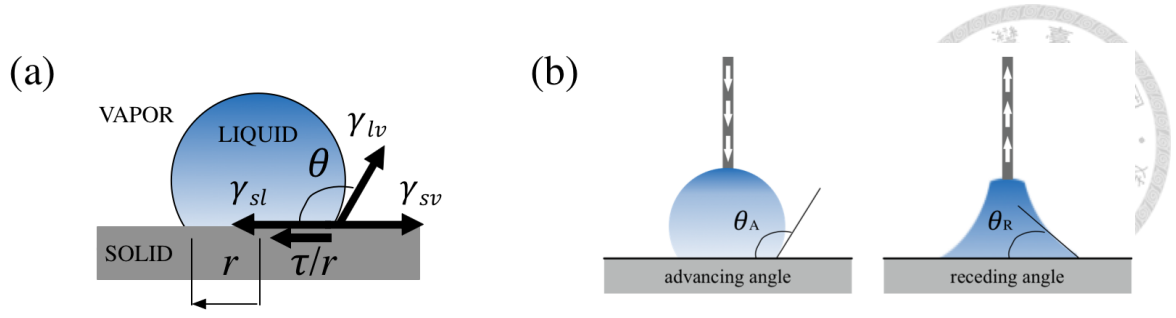


Figure 11. (a) Droplet in contact with a solid surface. (b) Advancing and receding angles.

of the solid surface (κ), the droplet surface tension (γ_{lv}), and the droplet size (r). This characteristic is worth investigating as a micro-engineered solid surface with well-controlled hysteresis is often of interest in medical or industrial applications [56-58].

In this paper, we experimentally characterize the line tension on micromachined surfaces and discuss its effect on the CA hysteresis. Particularly, the liquid-solid interaction that can be modeled by the modified Wenzel's equation is investigated. In addition, the Gibbs free energy is also introduced to evaluate the influence of line tension. By taking the line tension into account, the Gibbs free energy is [33, 57]

$$G = \gamma_{LV}a_{LV} + \gamma_{SL}a_{SL} + \gamma_{SV}a_{SV} + \tau l \quad (2.8)$$

where a is the area with the subscript 'SL' for the solid-liquid, 'SV' for the solid-vapor, and 'LV' for the liquid-vapor interface, respectively; l is the length of contact line. The Gibbs free energy can be further normalized as

$$G^* \equiv \frac{G}{(9V^2\pi)^{1/3} \gamma_{LV}} = \frac{2 - \lambda \cos \theta^* (1 + \cos \theta)}{[(1 - \cos \theta)(2 + \cos \theta)^2]^{1/3}} + \frac{2\kappa\tau \sin \theta}{\gamma_{LV} [3V(1 - \cos \theta)^2 (2 + \cos \theta) / \pi]^{1/3}} \quad (2.10)$$

where V is the droplet volume. We design surface structure of the solid substrate with different \mathcal{R} 's to verify the modulated effect of line tension. Specifically, the CA and droplet radius (r) are measured, and the line tension is determined through eq (2.7). The

results of experiment will facilitate the better understanding of line tension and its role in designing a CA hysteresis.



3.2 Experiment

3.2.1 Materials and fabrication

Polydimethylsiloxane (PDMS; Sil-More Industrial Ltd.) was adopted as the substrate material with various microstructure lengths (L) and duty ratios (DR , $DR=D/L$, D : distance.) Its structure is shown in Figure 12a and 12b. With this periodic structure, the ratio, λ , of actual interfacial area to the apparent area of the geometrical interface can be designed by

$$\lambda = \frac{4\sqrt{3} + (DR^2 + 4DR)}{(2 + DR)^2} \quad (3.2)$$

It represents the surface roughness of the engineered surface. The ratio, κ , of actual length of the three-phase contact line to the apparent becomes

$$\kappa = \frac{\sqrt{3} + DR}{1 + DR} \quad (3.3)$$

PDMS is elected for its high hydrophobicity, biocompatibility, and tunability of material properties [60]. The PDMS microstructures were fabricated by spin-coating and then curing PDMS solution on an array of pyramid cavities that were created on silicon wafer as a replication mold. These cavities were etched on silicon nitride (Si_3N_4) wafer using bulk micromachining techniques (Figure 12c). The SPR-220 photoresist was spun on the Si_3N_4 wafer and then UV-exposed under a patterned mask. After this photolithography step, reactive ion etching (RIE) was conducted to remove the portion of the Si_3N_4 that was not protected by the photoresist. Then, anisotropic etching of the single-crystal silicon wafer was carried out in heated KOH solution, forming the pyramid cavities. Eight L 's and five DR 's were produced for the systematic experiment. The L 's ranges from 15

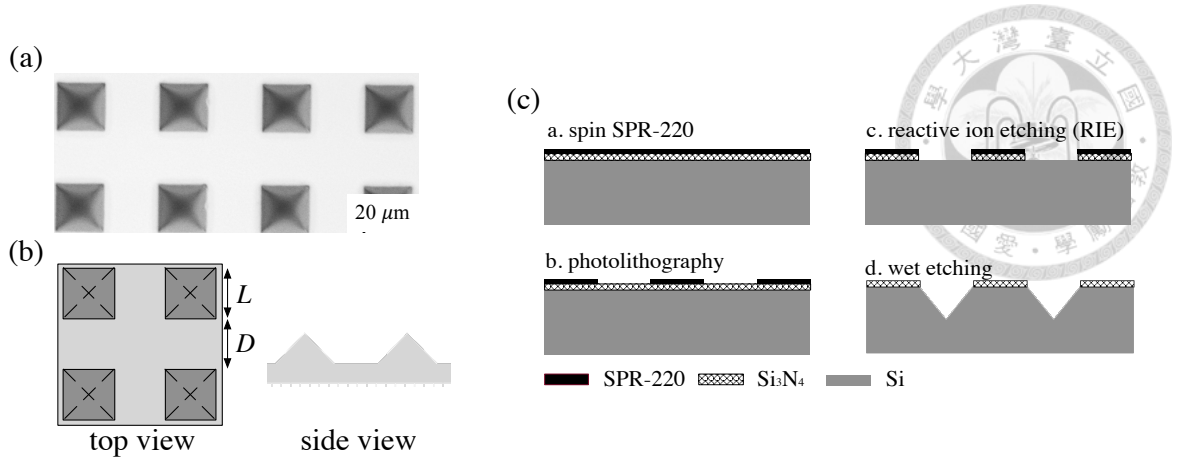


Figure 12. (a) Microscopic image of a fabricated PDMS surface. (b) Schematic view of the surface. (c) Process flow for fabricating the silicon mold.

to $50\ \mu\text{m}$ at the increment of $5\ \mu\text{m}$ and is referred to as L15~L50 in the experiment, respectively. Each L has five DR 's, that is referred to DR1~DR5 in the experiment for $DR=1,2,3,4,5$, respectively. Figure 2a shows a microscopy image of one of the fabricated surfaces.

3.2.2 Measurement of contact angles

The measurement of contact angles was conducted by using VCA Optima (AST Products, Inc.) The static contact angle was measured by analyzing the droplet image that was captured by the CCD camera. Deionized water (DI water) was used as the probe liquid. The droplets of $0.5\ \mu\text{L}$ was deposited on the textured surface with an area of approximately $10\ \text{mm} \times 10\ \text{mm}$ by a syringe. This radius of contact area of the droplet on the textured surface was larger than $0.3\ \text{mm}$ so we assumed that the contact angle did not change obviously by the radius from 0.3 to $0.7\ \text{mm}$.³⁰ In this paper, we change the volume of the droplet by using a syringe to characterize the dynamic contact angle. During the test, the syringe needle was kept at the middle of the droplet to minimize its effect on the contact angle at the droplet-substrate interface. We measured the advancing angle (θ_A) and receding angle (θ_R) by expanding and contracting droplet separately (Figure 13).

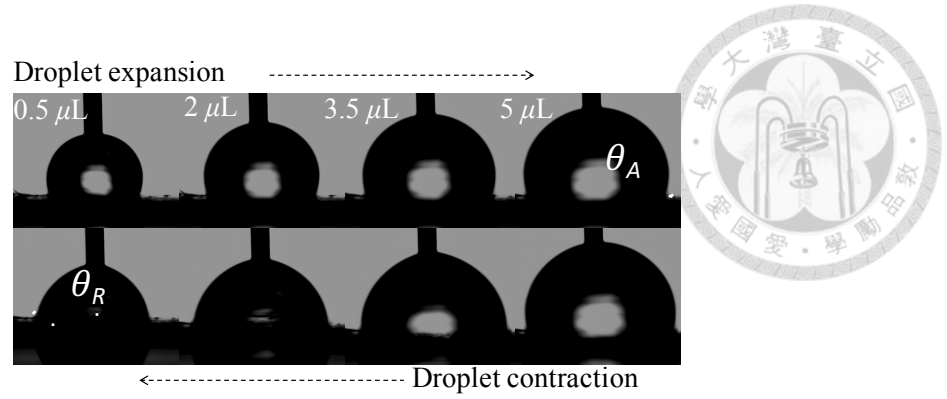


Figure 13. Images of expansion and contraction of the DI water droplet on the flat PDMS surface. The droplet volume was increased from 0.5 μL to 5 μL at 0.5 μL increment and then decreased.

3.3 Results and discussion

3.3.1 Static contact angle

The static contact angles of DI water on the textured surface are summarized in Table 1 by structure length (L). The standard deviation obtained from five independent experiments is also shown. For the cases of $L=0$, the surface is flat. Therefore, the intrinsic contact angle is found to be $107.2 \pm 1.1^\circ$. For a fixed structure length other than $L=0$, increasing DR from 1 to 5 yields decreasing surface roughness, \mathcal{A} , of 1.33, 1.18, 1.12, 1.08, and 1.06, respectively. For $L=15 \mu\text{m}$, the contact angle decreases from $128.5 \pm 1.5^\circ$ to $118.8 \pm 2.1^\circ$ as the surface roughness decreases from 1.33 to 1.06. This result is in agreement with the Wenzel's state. Figure 14a compares the measurement with the apparent contact angle from the Wenzel's model in eq (2.7) by ignoring the line tension term for $\mathcal{A}=1.33$ and 1.06 (see in the Supporting information for other \mathcal{A} 's). It is obvious that the measurement is larger than the angle predicted by the Wenzel's model if the line tension is not considered. The deviation can be used to extract the line tension by fitting the full eq (2.7) with the measurement, as shown in Figure 14b. The obtained line tension does not fluctuate much with various surface roughness. Therefore, the line tension can

be considered constant when the droplet is at static state. Its average is $4.48 \pm 0.22 \mu\text{J/m}$, close to the line tension on gold surface with self-assembled monolayers of alkanethiols³⁹, but five-order larger than that on silicon surface.³⁰

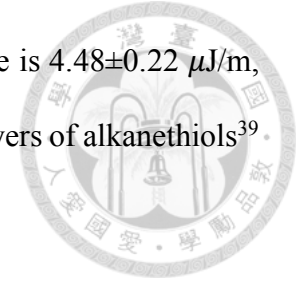


Table 1. Measured contact angle of DI water on textured surfaces.

Structure length, L (μm)	Contact angle ($^\circ$)				
	$DR=1$ (DR1)	$DR=2$ (DR2)	$DR=3$ (DR3)	$DR=4$ (DR4)	$DR=5$ (DR5)
	$\lambda=1.33$	$\lambda=1.18$	$\lambda=1.12$	$\lambda=1.08$	$\lambda=1.06$
	$\kappa=1.37$	$\kappa=1.24$	$\kappa=1.18$	$\kappa=1.15$	$\kappa=1.12$
0	107.2 ± 1.1	107.2 ± 1.1	107.2 ± 1.1	107.2 ± 1.1	107.2 ± 1.1
15	128.5 ± 1.5	122.9 ± 2.1	120.7 ± 1.6	119.3 ± 2.4	118.8 ± 2.1
20	128.1 ± 1.1	122.3 ± 2.2	120.8 ± 0.9	119.6 ± 1.3	117.0 ± 2.1
25	129.3 ± 0.9	123.2 ± 1.4	121.8 ± 1.5	119.3 ± 1.5	118.2 ± 1.8
30	128.7 ± 1.5	123.6 ± 2.0	119.8 ± 2.6	117.3 ± 1.0	116.3 ± 1.2
35	127.8 ± 3.3	123.5 ± 2.8	118.2 ± 1.8	117.2 ± 1.3	115.3 ± 2.6
40	128.8 ± 2.5	122.8 ± 1.3	120.9 ± 2.6	119.2 ± 2.3	117.3 ± 3.2
45	127.9 ± 1.9	123.7 ± 2.1	118.2 ± 2.3	117.2 ± 1.1	115.3 ± 1.9
50	127.0 ± 2.3	121.4 ± 1.6	120.1 ± 1.7	118.0 ± 1.4	118.1 ± 2.5

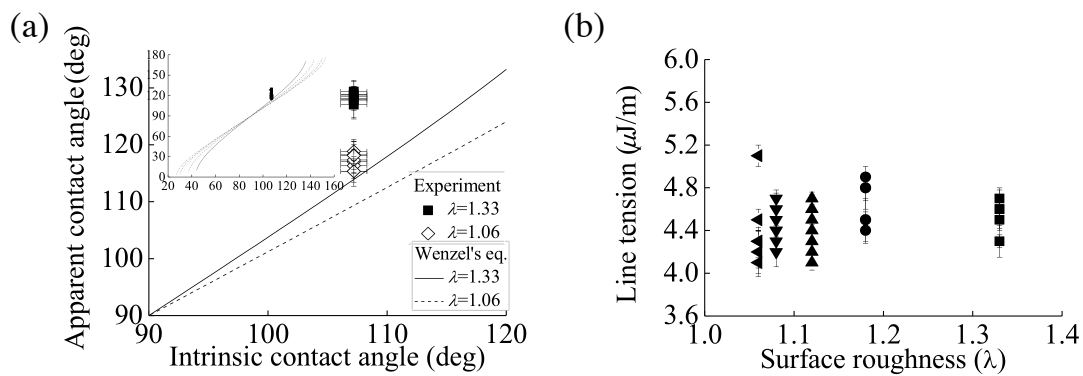


Figure 14. (a) The relationship between the apparent contact angle and intrinsic contact angle by ignoring the effect of line tension. The inset shows the measurement and Wenzel's equation for all λ 's. (b) Extracted line tension at different surface roughness.

3.3.2 Contact angle hysteresis

Table 2 shows the measured CA hysteresis, as defined by eq (3.1), of DI water on the textured surface by structure length and surface roughness. On the flat surface, the CA hysteresis is $23.0 \pm 1.3^\circ$. For $L=15 \mu\text{m}$, the CA hysteresis decreases from $62.1 \pm 2.1^\circ$ to $30.1 \pm 1.9^\circ$ as the surface roughness decreases from 1.33 to 1.06. The effect of structure length, L , is not obvious on the relatively smoother surface such as $\lambda=1.06$ ($DR=5$). At large DR , there are fewer structures underneath the droplet so that the form factor of the structures plays little role at the solid-liquid interface. On the other hand, the structure length dominates the solid-liquid interface on a rough surface. For the cases of $\lambda=1.33$ ($DR=1$), the CA hysteresis decreases from $62.1 \pm 2.1^\circ$ to $47.1 \pm 2.6^\circ$ as the structure length increases from $15 \mu\text{m}$ to $50 \mu\text{m}$. Given the same surface roughness, the smaller structure length yields higher CA hysteresis.

The case of $L=15 \mu\text{m}$, $\lambda=1.33$, and $\kappa=1.37$ is taken as an example to discuss the role of the line tension (see more results of experiment in the Supporting information). Its contact angle, radius of three-phase contact line, and line tension are shown in Figure 15. In the experiment, the droplet volume was increased from $0.5 \mu\text{L}$ to $5 \mu\text{L}$ at $0.5 \mu\text{L}$ increment and then decreased, as indicated by the arrows in the figure. When the droplet volume increases from $0.5 \mu\text{L}$ to $4 \mu\text{L}$, the contact angle increases from 126.4° to 137.1° , as shown in Figure 5a. When the droplet volume exceeds $4 \mu\text{L}$, the measured contact angle becomes a constant, which is defined as the advancing angle. In Figure 15a, the advancing angle, θ_A , is 137.1° as marked by the upper dashed line. The radius of the contact line increases from 0.49 mm to 1.02 mm when the droplet volume increases from $0.5 \mu\text{L}$ to $4 \mu\text{L}$, as shown in Figure 5b. Given the radius, the line tension can be calculated from eq 1. It increases from $4.9 \mu\text{J/m}$ to $18.3 \mu\text{J/m}$ as the droplet volume increases from $0.5 \mu\text{L}$ to $4 \mu\text{L}$, as shown in Figure 5c.

Table 2. Measured contact angle hysteresis of DI water on textured surfaces

Structure length, L (μm)	Contact angle hysteresis ($^\circ$)				
	$DR=1$ (DR1)	$DR=2$ (DR2)	$DR=3$ (DR3)	$DR=4$ (DR4)	$DR=5$ (DR5)
	$\lambda=1.33$	$\lambda=1.18$	$\lambda=1.12$	$\lambda=1.08$	$\lambda=1.06$
	$\kappa=1.37$	$\kappa=1.24$	$\kappa=1.18$	$\kappa=1.15$	$\kappa=1.12$
0	23.0 ± 1.3	23.0 ± 1.3	23.0 ± 1.3	23.0 ± 1.3	23.0 ± 1.3
15	62.1 ± 2.1	41.9 ± 0.8	34.2 ± 2.2	32.1 ± 3.1	30.1 ± 1.9
20	57.9 ± 1.2	41.1 ± 1.1	33.0 ± 0.9	32.3 ± 1.6	29.2 ± 3.2
25	53.4 ± 3.3	38.3 ± 1.7	35.2 ± 2.5	31.4 ± 1.1	30.1 ± 4.2
30	52.9 ± 0.9	40.5 ± 2.3	36.2 ± 1.8	33.1 ± 3.4	30.3 ± 3.6
35	50.5 ± 1.9	39.0 ± 2.7	34.5 ± 4.7	33.2 ± 1.9	30.6 ± 1.6
40	49.4 ± 3.1	41.0 ± 2.9	37.5 ± 3.1	32.3 ± 3.3	30.4 ± 2.0
45	48.3 ± 1.1	38.2 ± 1.2	35.9 ± 1.0	30.5 ± 0.8	28.2 ± 1.4
50	47.1 ± 2.6	37.1 ± 2.4	32.0 ± 1.6	30.3 ± 2.4	28.0 ± 3.8

When the droplet volume decreases from $5 \mu\text{L}$ to $0.5 \mu\text{L}$, the contact angle decreases from 137.1° to 74.6° , as shown in Figure 15a. The measured contact angle becomes a constant when the droplet volume is smaller than $1.5 \mu\text{L}$. This constant is defined as the receding angle, as marked by the lower dashed line in Figure 15a. It should be noted that the radius of contact line remains unchanged at first until the droplet volume becomes smaller than $1.5 \mu\text{L}$. The radius decreases from 1.02 mm to 0.78 mm when the droplet recedes from $1.5 \mu\text{L}$ to $0.5 \mu\text{L}$, as shown in Figure 15b. By applying the results of the experiment into eq (2.7), the line tension at the receding state can also be calculated, as shown in Figure 15c. The line tension changes sign from $18.3 \mu\text{J/m}$ to $-35.7 \mu\text{J/m}$ as the droplet recedes from $5 \mu\text{L}$ to $1 \mu\text{L}$. It then increases slightly to $-28.5 \mu\text{J/m}$ at the droplet volume of $0.5 \mu\text{L}$.

Figure 15d shows the extracted line tension versus the radius of contact line. Both the radius of contact line and the line tension increases with increasing the droplet volume. When the droplet volume starts to decrease at $5 \mu\text{L}$, the line tension pins the radius of

droplet at 1.02 mm whereas the line tension changes sign. This pinning effect vanishes when the droplet volume becomes smaller than 1.5 μL , as which the contact angle becomes constant.

From Liu et al. [48], the line tension changes with different fluid-solid interactions, and its sign plays a key role in maintaining the thermodynamics equilibrium at a given contact angle. A positive line tension implies that the enthalpy of the surface tension is larger than that given by the contact line. In Figure 15d, the hysteresis of the line tension versus the radius of the contact line can be separated into three states. At the first state, the line tension is positive and increases from 0.005 mJ/m to 0.018 mJ/m when the radius of the contact line increases from 0.49 mm to 1.02 mm. At the second step of reducing the droplet volume, the contact line pins the droplet so that the radius remains unchanged. Meanwhile, the line tension decreases from 0.018 mJ/m to -0.035 mJ/m, which reduces the contact angle. This pinning effect causes the CA hysteresis, and the sign change of the line tension is observed. The radius started to reduce when the line tension starts to increase at the third step, as indicated in Figure 15d. Meanwhile, the contact angle becomes a constant, which is referred to as the receding angle of 74.6°, as shown in Figure 15a.

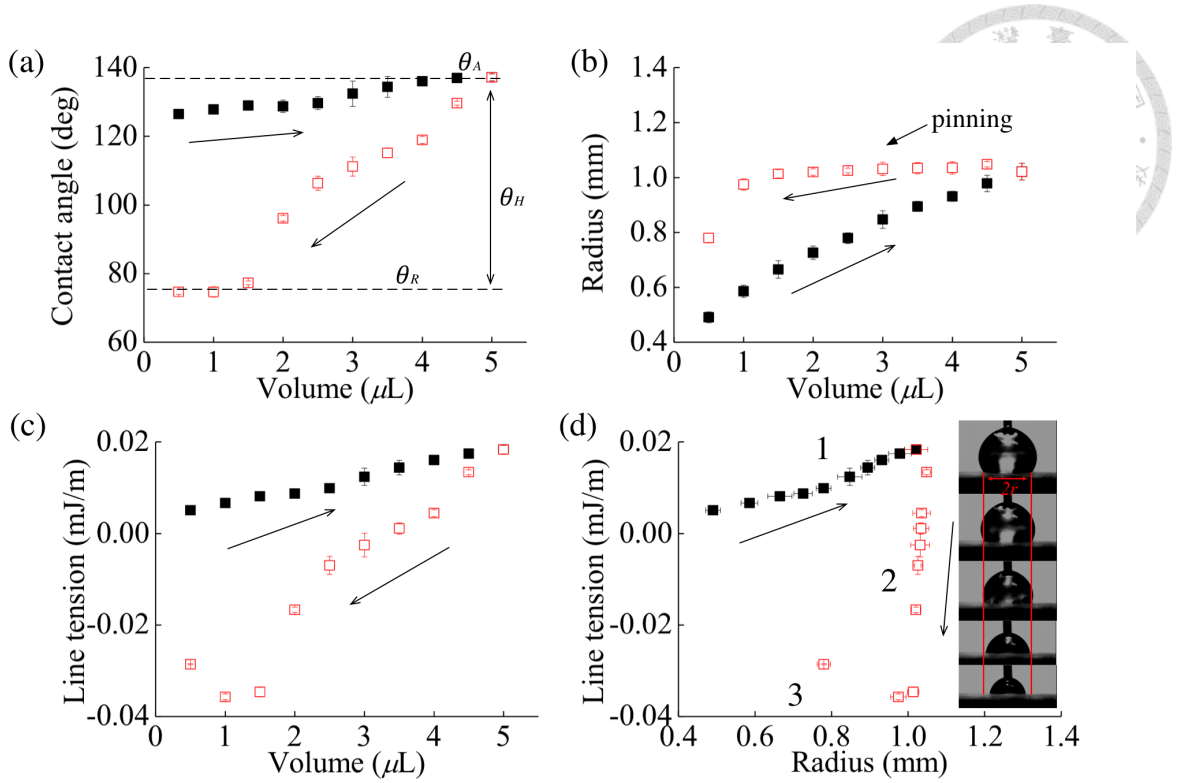


Figure 15. The measurement results of $\lambda=1.33$ and $\kappa=1.37$. (a) Contact angle hysteresis. (b) Radius of contact line versus droplet volume. (c) Line tension versus droplet volume. (d) Line tension versus radius of contact line.

3.3.3 Hysteresis of Gibbs free energy

The correlation between the variation of the Gibbs free energy and the CA hysteresis can be evaluated by the definition of eq (2.10). By fixing the structure length at $L=15 \mu\text{m}$, the effect of surface roughness, $\lambda=1.33, 1.12, 1.06$ on such correlation is discussed (see more results of experiment in the Supporting information). The Gibbs energy (G^*) can also be separated into three steps like the same steps in Figure 5(d). For $\lambda=1.33$ in Figure 6(a), at the first step as the droplet volume increases, the G^* increases slightly from 1.59 to 1.65 as the contact line radius increases from 0.49 mm to 0.93 mm. It then keeps at 1.65 for larger contact line radius. Similarly in Figures 6(b) and 6(c) for $\lambda=1.12$ and 1.06, the G^* increases with contact line radius when the droplet advances. When the droplet volume starts to decrease at the second step in Figure 6(a), the G^* decreases from 1.65

to 0.61. Meanwhile, the contact line pins the droplet so that the contact line radius is fixed at 1.01 mm as shown. As the droplet continues to recede at the third step, the G^* decreases from 0.61 to 0.47 with the contact line radius decreasing from 1.01 mm to 0.97 mm, as shown in Figure 16a. The G^* does not change if the contact line radius becomes smaller than 0.97 mm.

The results of experiment indicate that the line tension reduces the Gibbs energy at the second step as the droplet volume starts to decrease. The line tension also makes the Gibbs energy almost unchanged when the droplet advances or recedes with constant contact angle. It is noticed that the Gibbs energy decreases, $\Delta G < 0$, for the droplet to advance first and then recede. Thus, the occurrence of the CA hysteresis is spontaneous. From Figures 15d and 16a, it is found that the line tension increases to maintain the advancing contact angle as the droplet volume keeps increasing. At the contraction state of the droplet, the line tension plays a dominant role in the CA hysteresis. It also reduces the Gibbs energy to maintain the receding contact angle as the droplet volume keeps decreasing.

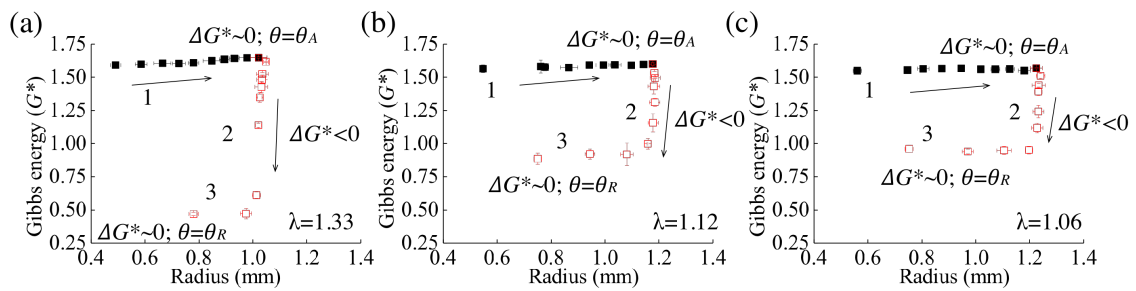


Figure 16. Gibbs energy (G^*) of $L=15 \mu\text{m}$ with (a) $\lambda=1.33$. (b) $\lambda=1.12$. (c) $\lambda=1.06$. $\Delta G \sim 0$ for θ is equal to advancing angle and receding angle.

3.3.4 Ratio of the actual length of the contact line to the apparent (κ)



Generally, increasing the surface roughness also increases the ratio, κ , of actual length of the three-phase contact line to the apparent. In our cases, the increment of surface roughness increases the contact angle and the interfacial tension at the liquid-vapor surface. It causes the line tension to increase and to pin the droplet. For the droplet to advance and recede on the substrate with the structure length of $L=15\ \mu\text{m}$, the measured line tension and contact angle are shown in Figure 17. The maximum radius for the cases of $\kappa=1.37$, 1.15, and 1.12 is 1.01, 1.20, and 1.23 mm, respectively. To reach the same droplet volume, the maximum radius of the contact line decreases as the surface roughness increases. However, the perimeter, $2\pi r\kappa$, of the droplet remains almost unchanged as it is 8.68, 8.66, and 8.66 mm for $\kappa=1.37$, 1.15, and 1.12, respectively. That is, all these surfaces pin the droplet with the same perimeter. However, Figure 17a indicates that larger κ causes larger magnitude of line tension in both the advancing and receding states. It is also noticed that the larger κ causes smaller droplet footprint. These results indicate that enlarging κ would make the effect of line tension more prominent, also magnifying the hysteresis of the Gibbs energy, as shown in Figure 16.

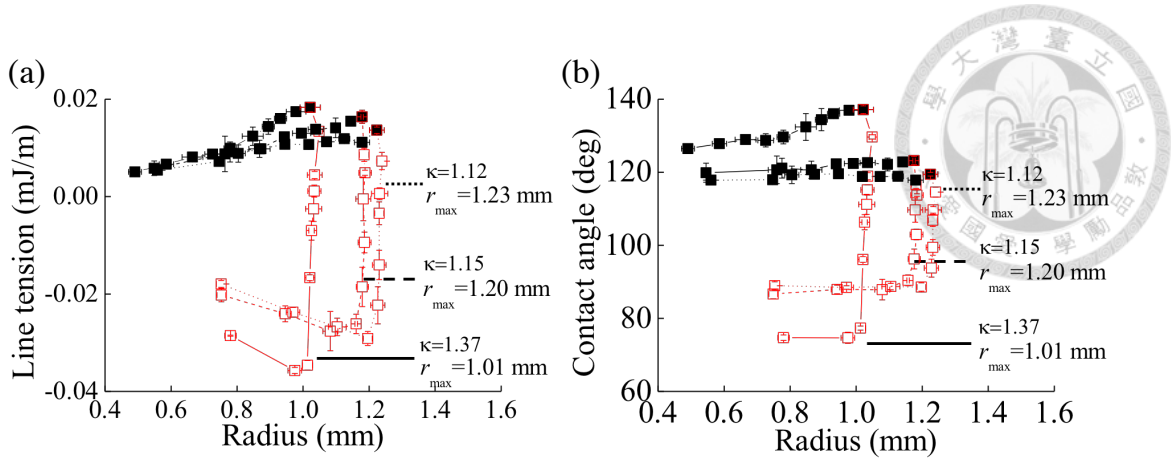


Figure 17. (a) Extracted line tension versus the radius of three-phase contact line for $L=15 \mu\text{m}$. Measured contact angle versus the radius of three-phase contact line.

3.3.5 Effect of structure length

From eq (2.7), the measurement of the CA hysteresis, $\cos\theta_R - \cos\theta_A$, can be written as

$$\cos\theta_R - \cos\theta_A = \frac{\kappa}{\gamma_{LV}} \left(\frac{\tau_A}{r_A} - \frac{\tau_R}{r_R} \right) \quad (3.4)$$

In this study, all the experiments were conducted at the same temperature so that $\gamma_{LV}=72.8 \text{ mJ/m}^2$ is fixed. From eq (3.4), the measurement of CA hysteresis is proportional to the ratio, κ , of actual length of the three-phase contact line to the apparent. Figures 18 and 19a verify the linear relationship between the $\cos\theta_R - \cos\theta_A$ and the ratio κ for different structure lengths. The advancing and receding angles were measured from the insets of Figure 18. The slopes of the linear regression in Figure 8 are 1.32, 1.23, 1.19 and 1.16 for $L=25, 30, 35$, and $40 \mu\text{m}$, respectively. Interestingly, the proportional constant between the $\cos\theta_R - \cos\theta_A$ and the ratio κ decreases when the structure length increases, as shown in Figure 19b. The error bars in Figure 19b show the first standard deviation of five-time experiment. A linear approximation of Figure 19b can be written as

$$(\cos\theta_R - \cos\theta_A) / \kappa = \alpha(1 - L / L_0) \quad (3.5)$$

Particularly for the cases of $\kappa=1.12\sim 1.37$ and $L=0\sim 50\text{ }\mu\text{m}$, it is found that $\alpha=1.86$ and $L_0=109.4\text{ }\mu\text{m}$. Equation (3,5) provides an empirical tool for modulating the CA hysteresis on a micromachined surface.

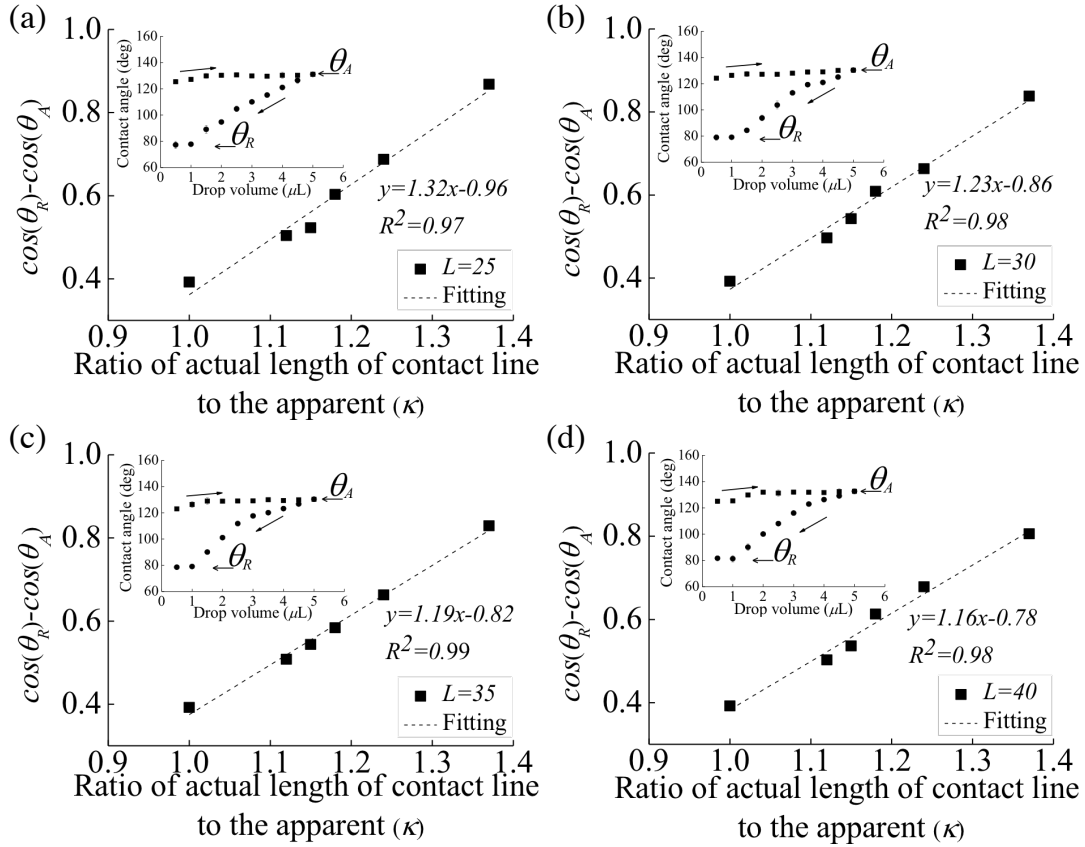


Figure 18. CA hysteresis versus κ for different structure lengths: (a) $L=25\text{ }\mu\text{m}$. (b) $L=30\text{ }\mu\text{m}$. (c) $L=35\text{ }\mu\text{m}$. (d) $L=40\text{ }\mu\text{m}$.

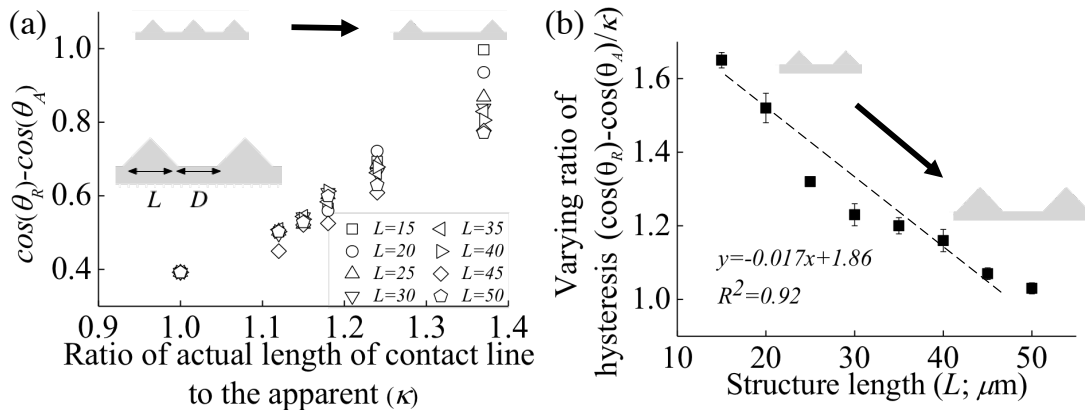


Figure 19. (a) Results of different structure lengths with different surface roughness. (b) The relationship between the contact angle hysteresis and the structure length.

3.4 Conclusion

This paper experimentally investigated the role of line tension in the contact angle hysteresis of a droplet on different micromachined surfaces. The line tension changes sign from the advancing to the receding state, causing the contact angle hysteresis. The surface tension dominates the contact angle in the advancing state while the line tension in the receding state. By the results on the different characteristic length of the surface structure, the surface roughness affects the static contact angle mainly. The ratio (κ) of actual length of the three-phase contact line to the apparent and the structure length (L) mainly affect the line tension in the receding state. Accordingly, an empirical equation has been developed to modulate the line tension and hence the contact angle hysteresis. By changing κ and L , the static contact angle can be altered from $107 \pm 1.1^\circ$ to $129.3 \pm 0.9^\circ$. The contact angle hysteresis changed grade from $23.1 \pm 1.3^\circ$ to $62.1 \pm 2.1^\circ$. These results shall facilitate the design of biomimetic petal-like surfaces.

3.5 Experiment Results of other structures

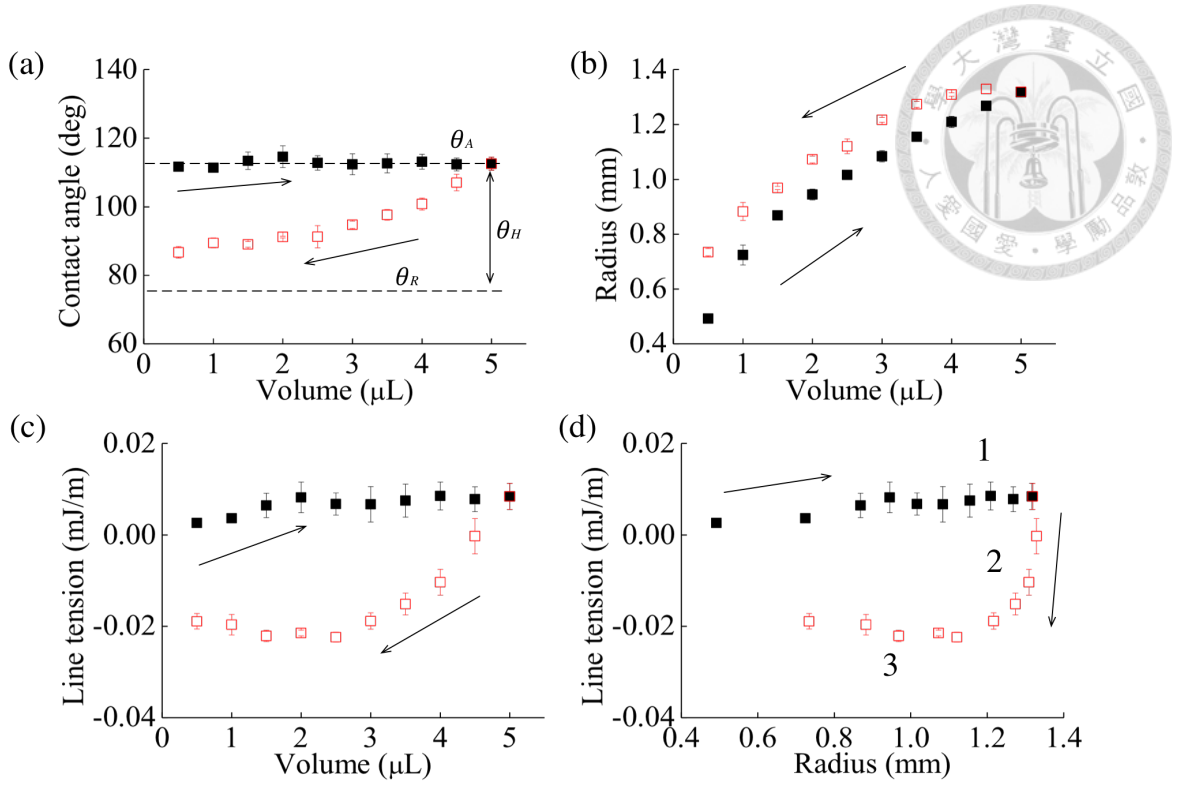


Figure 20. The measurement results of flat surface ($L=0$). (a) Contact angle hysteresis. (b) Radius of contact line versus droplet volume. (c) Line tension versus droplet volume. (d) Line tension versus radius of contact line.

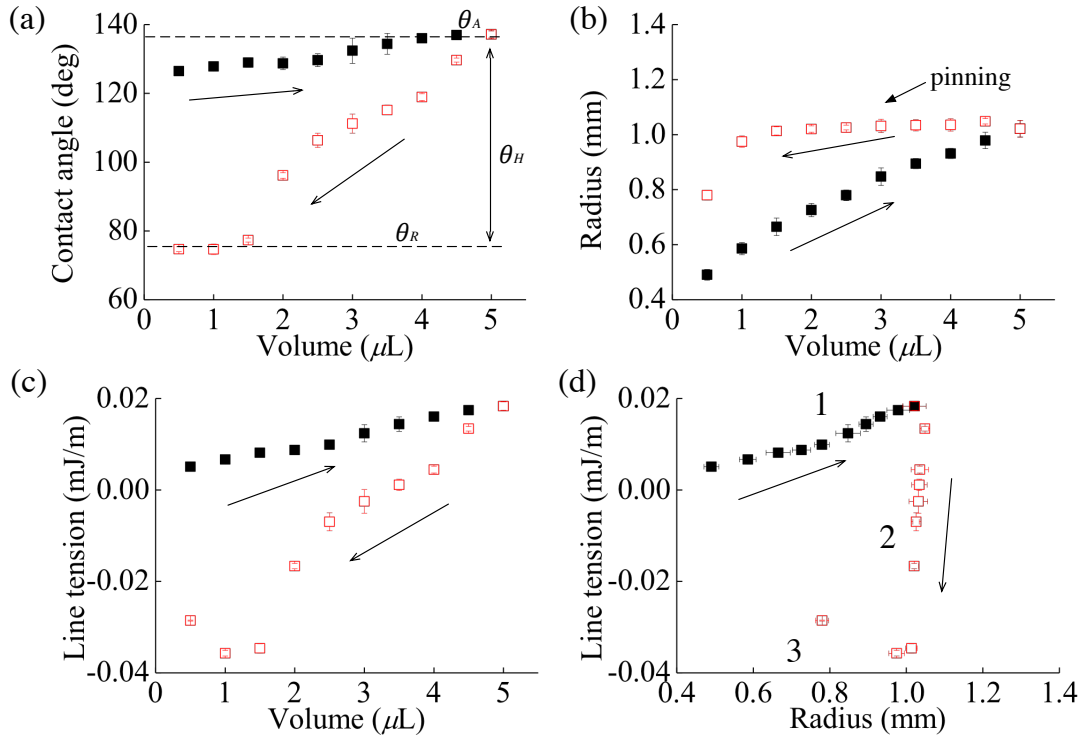


Figure 21. The measurement results of $L=15 \mu\text{m}$, $\lambda=1.33$ and $\kappa=1.37$. (a) Contact angle hysteresis. (b) Radius of contact line versus droplet volume. (c) Line tension versus droplet volume. (d) Line tension versus radius of contact line.

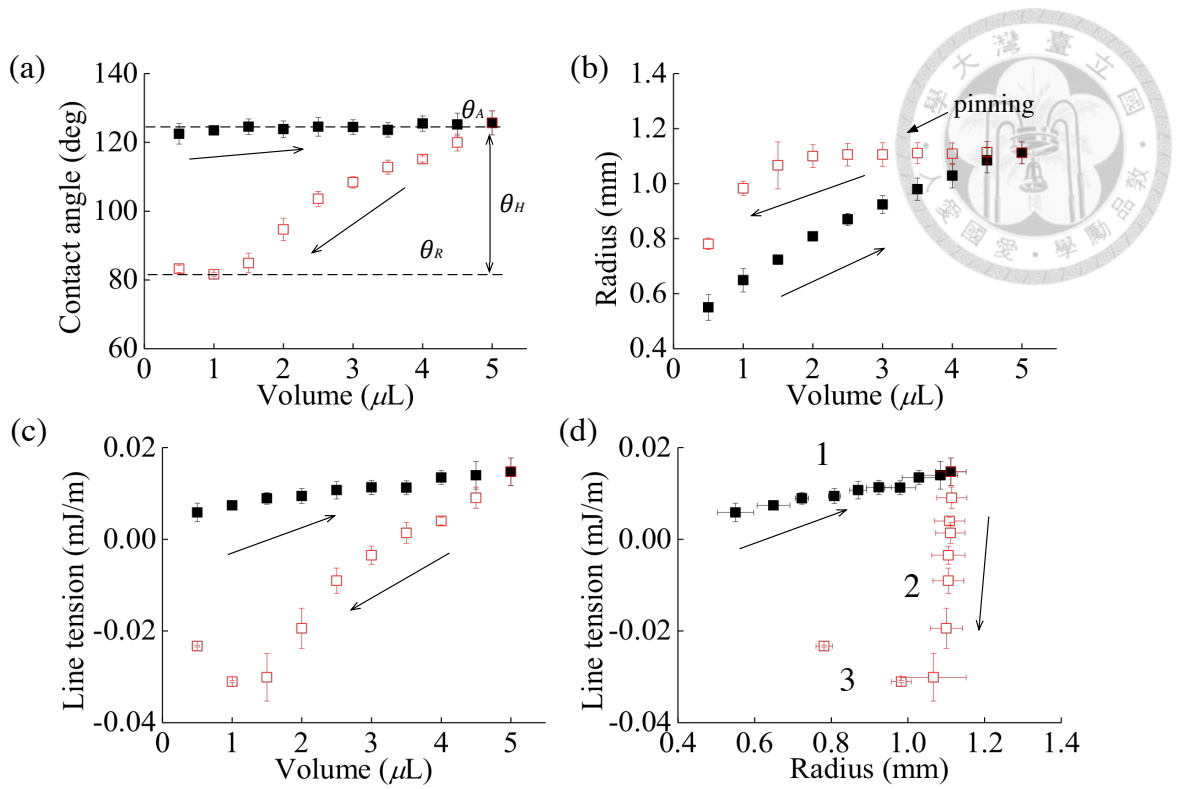


Figure 22. The measurement results of $L=15 \mu\text{m}$, $\lambda=1.18$ and $\kappa=1.24$. (a) Contact angle hysteresis. (b) Radius of contact line versus droplet volume. (c) Line tension versus droplet volume. (d) Line tension versus radius of contact line.

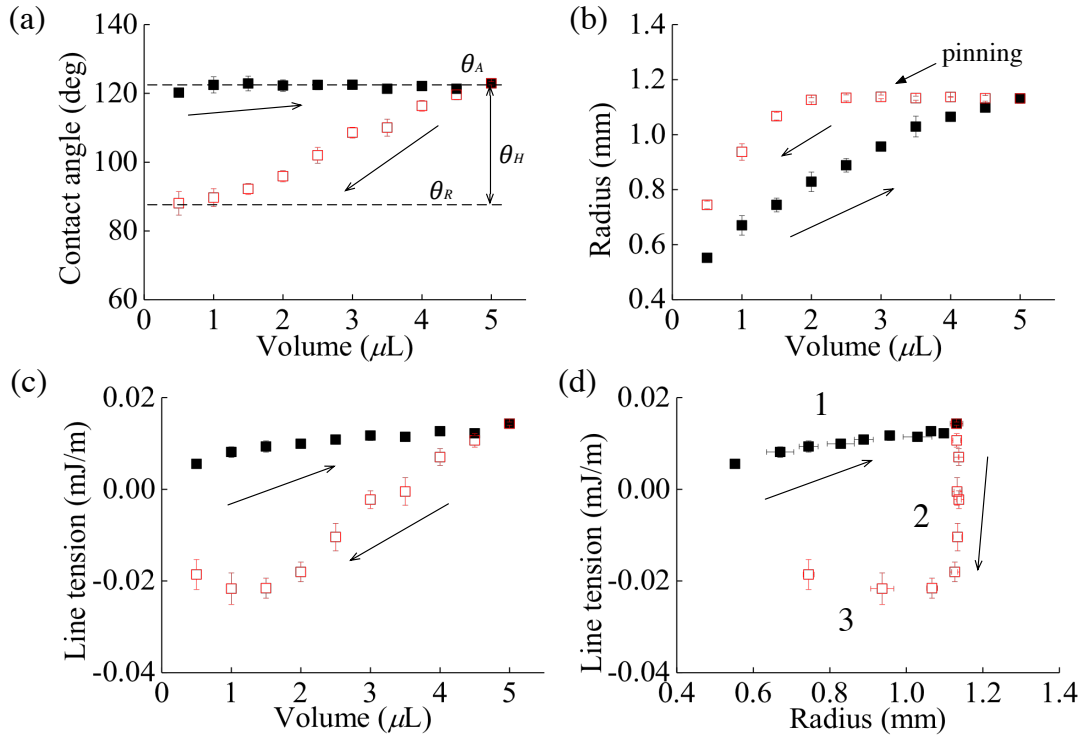


Figure 23. The measurement results of $L=15 \mu\text{m}$, $\lambda=1.12$ and $\kappa=1.18$. (a) Contact angle hysteresis. (b) Radius of contact line versus droplet volume. (c) Line tension versus droplet volume. (d) Line tension versus radius of contact line.

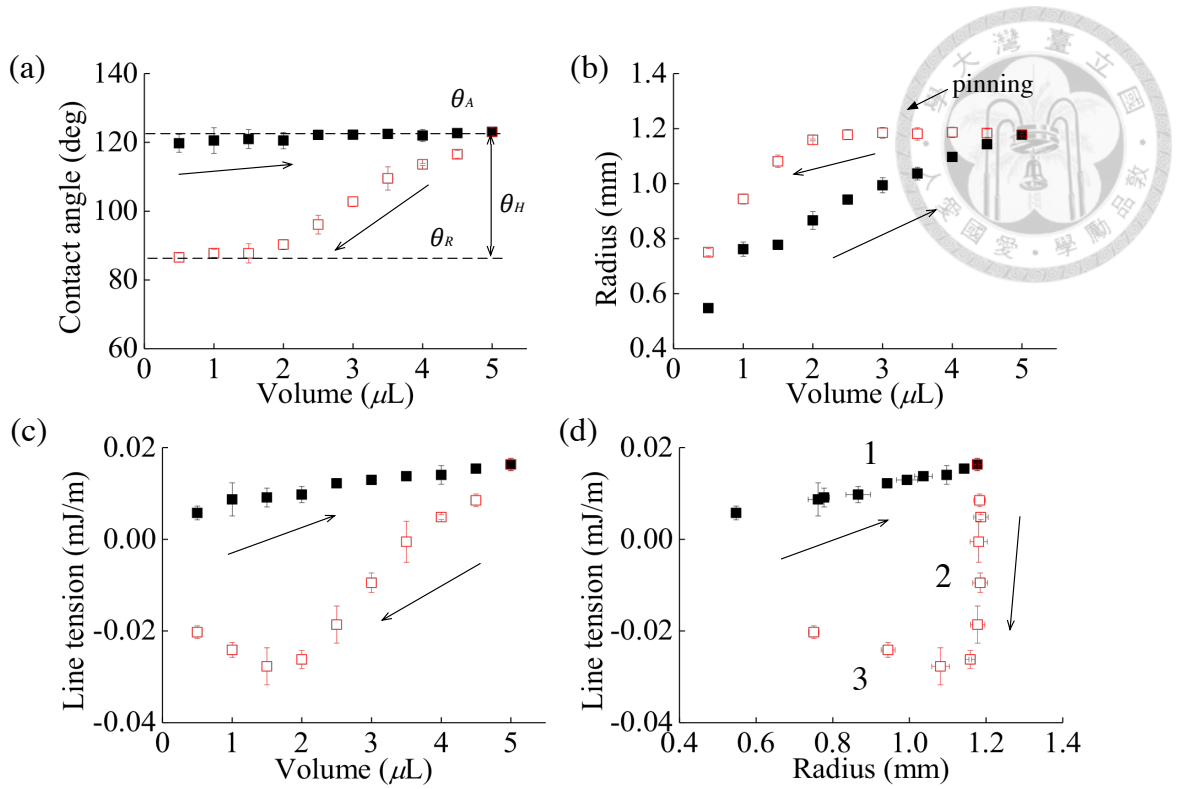


Figure 24. The measurement results of $L=15\ \mu\text{m}$, $\lambda=1.08$ and $\kappa=1.15$. (a) Contact angle hysteresis. (b) Radius of contact line versus droplet volume. (c) Line tension versus droplet volume. (d) Line tension versus radius of contact line.

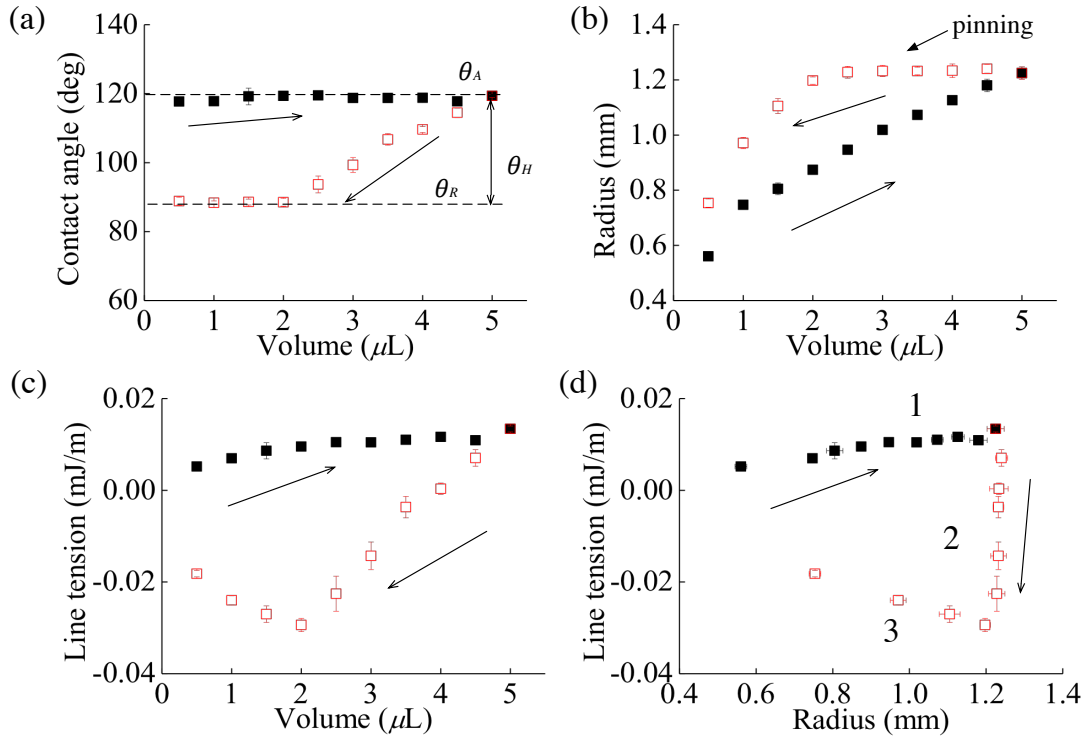


Figure 25. The measurement results of $L=15\ \mu\text{m}$, $\lambda=1.06$ and $\kappa=1.12$. (a) Contact angle hysteresis. (b) Radius of contact line versus droplet volume. (c) Line tension versus droplet volume. (d) Line tension versus radius of contact line.

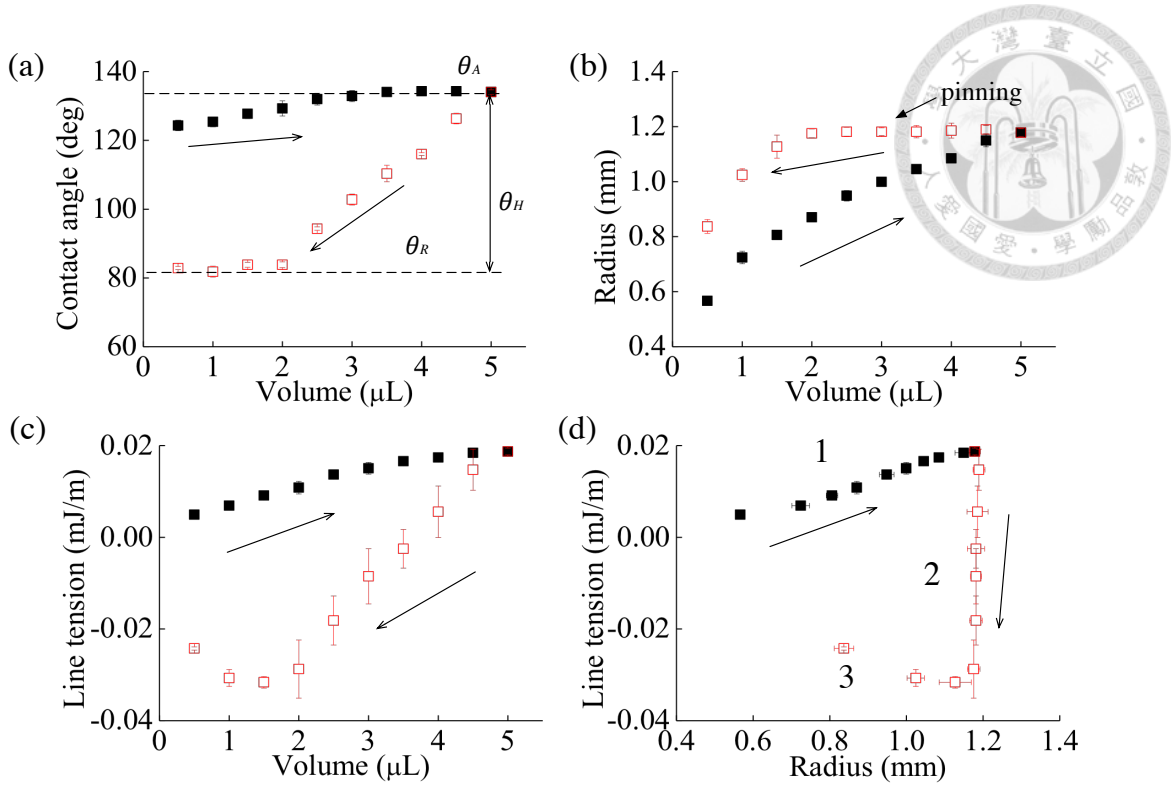


Figure 26. The measurement results of $L=20\ \mu\text{m}$, $\lambda=1.33$ and $\kappa=1.37$. (a) Contact angle hysteresis. (b) Radius of contact line versus droplet volume. (c) Line tension versus droplet volume. (d) Line tension versus radius of contact line.

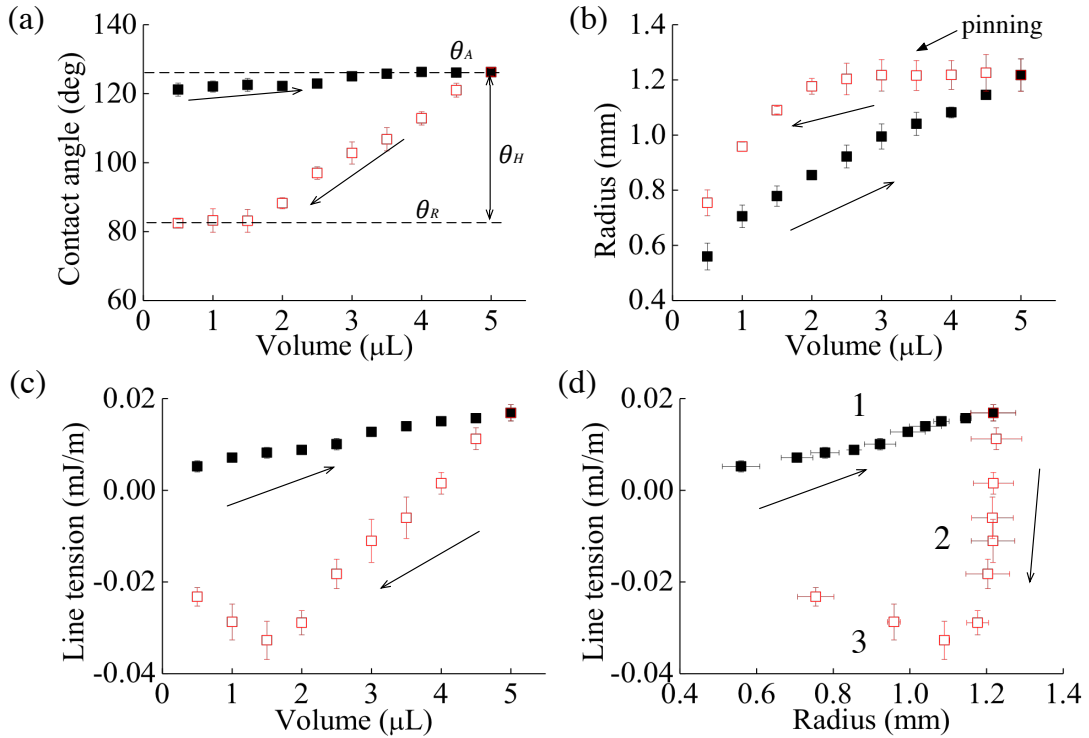


Figure 27. The measurement results of $L=20\ \mu\text{m}$, $\lambda=1.18$ and $\kappa=1.24$. (a) Contact angle hysteresis. (b) Radius of contact line versus droplet volume. (c) Line tension versus droplet volume. (d) Line tension versus radius of contact line.

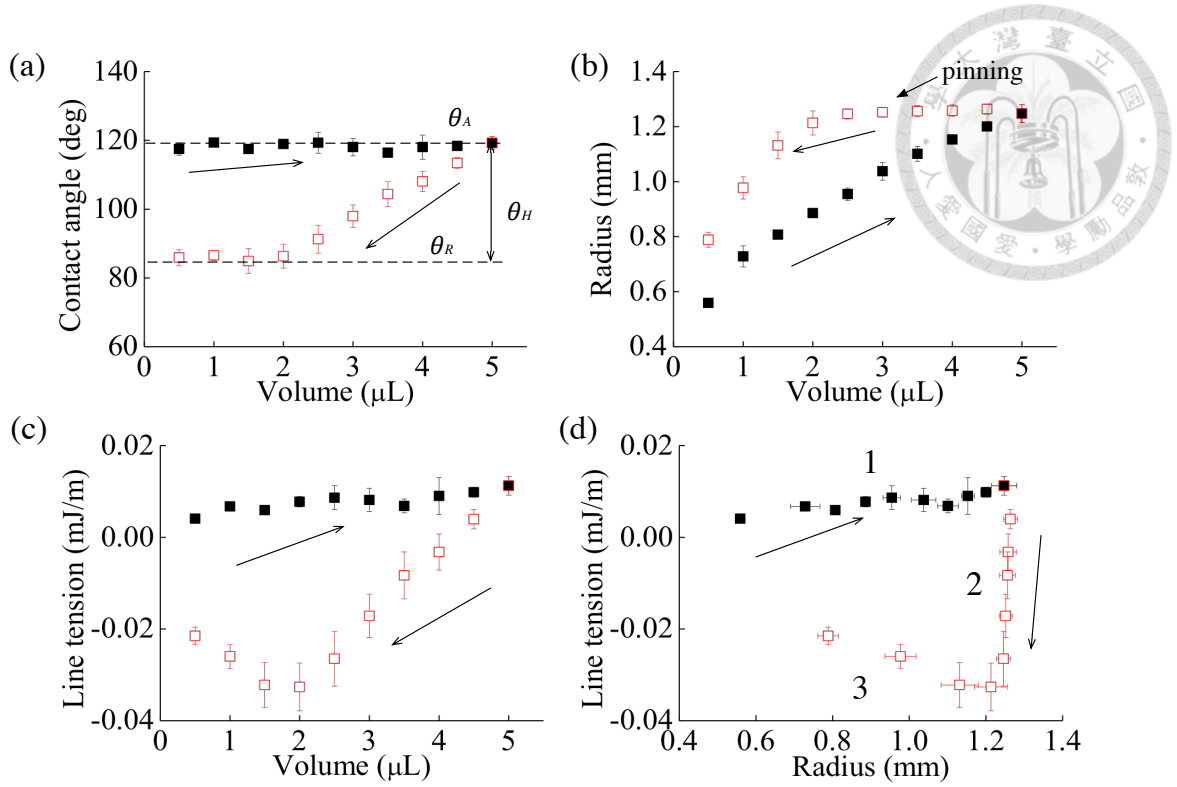


Figure 28. The measurement results of $L=20\ \mu\text{m}$, $\lambda=1.12$ and $\kappa=1.18$. (a) Contact angle hysteresis. (b) Radius of contact line versus droplet volume. (c) Line tension versus droplet volume. (d) Line tension versus radius of contact line.

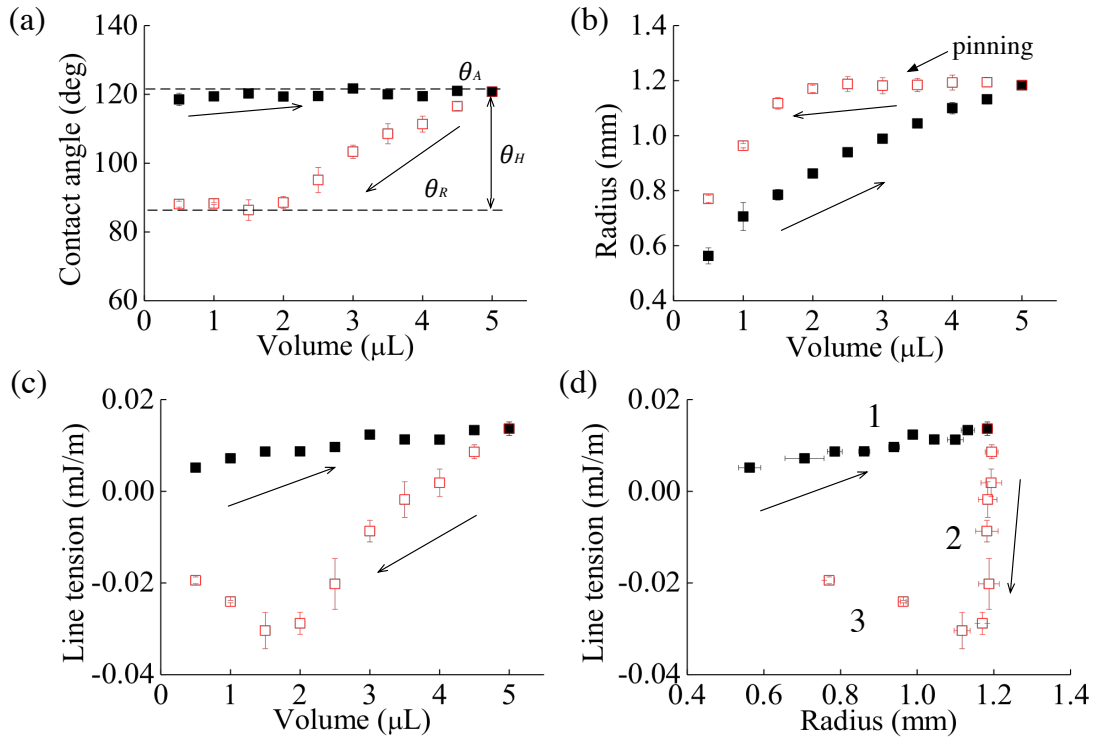


Figure 29. The measurement results of $L=20\ \mu\text{m}$, $\lambda=1.08$ and $\kappa=1.15$. (a) Contact angle hysteresis. (b) Radius of contact line versus droplet volume. (c) Line tension versus droplet volume. (d) Line tension versus radius of contact line.

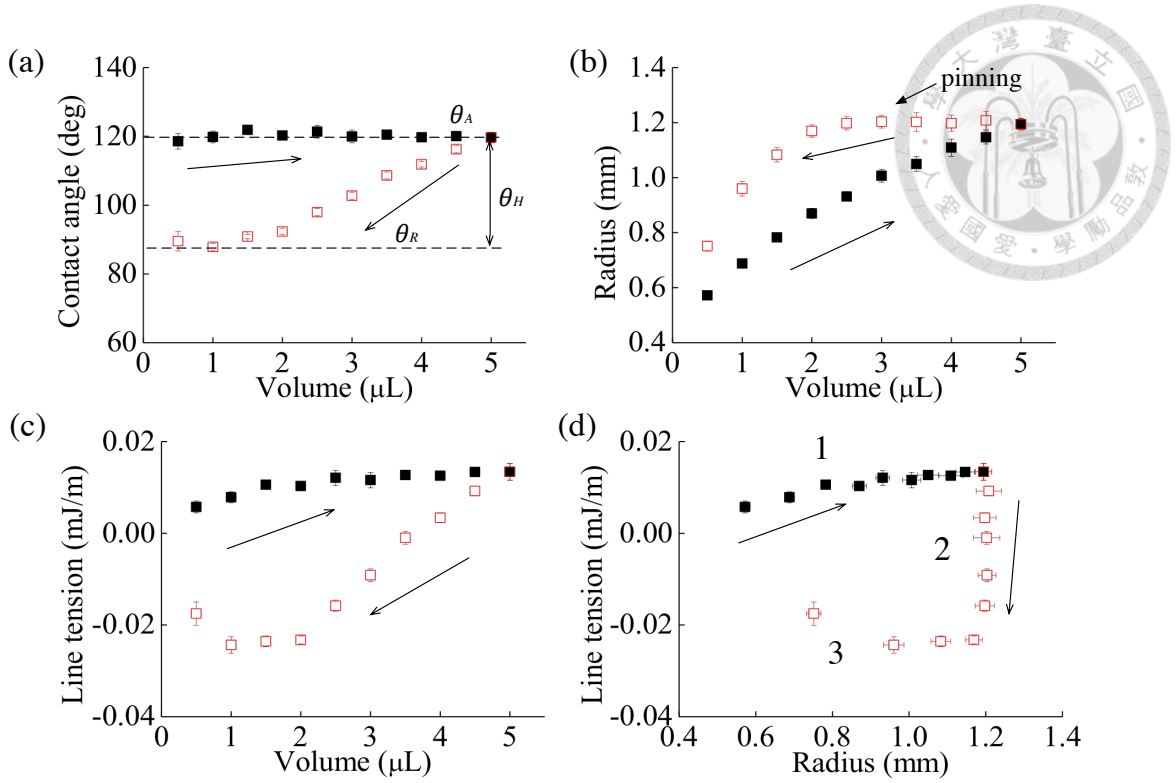


Figure 30. The measurement results of $L=20\ \mu\text{m}$, $\lambda=1.06$ and $\kappa=1.12$. (a) Contact angle hysteresis. (b) Radius of contact line versus droplet volume. (c) Line tension versus droplet volume. (d) Line tension versus radius of contact line.

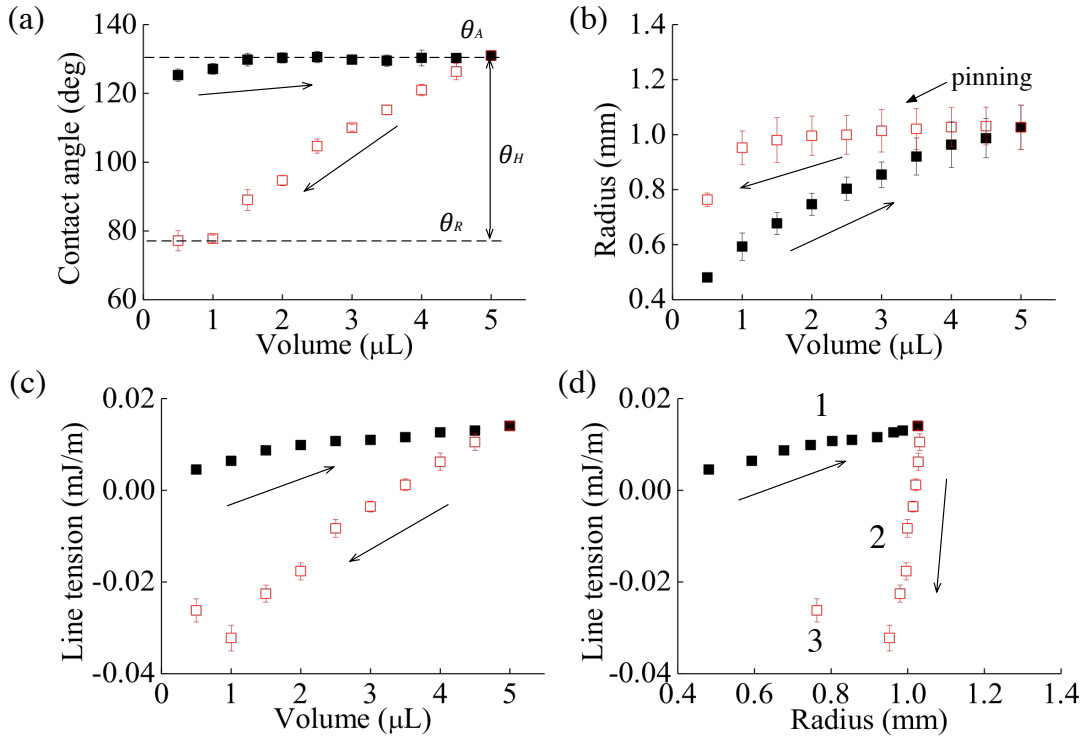


Figure 31. The measurement results of $L=25\ \mu\text{m}$, $\lambda=1.33$ and $\kappa=1.37$. (a) Contact angle hysteresis. (b) Radius of contact line versus droplet volume. (c) Line tension versus droplet volume. (d) Line tension versus radius of contact line.

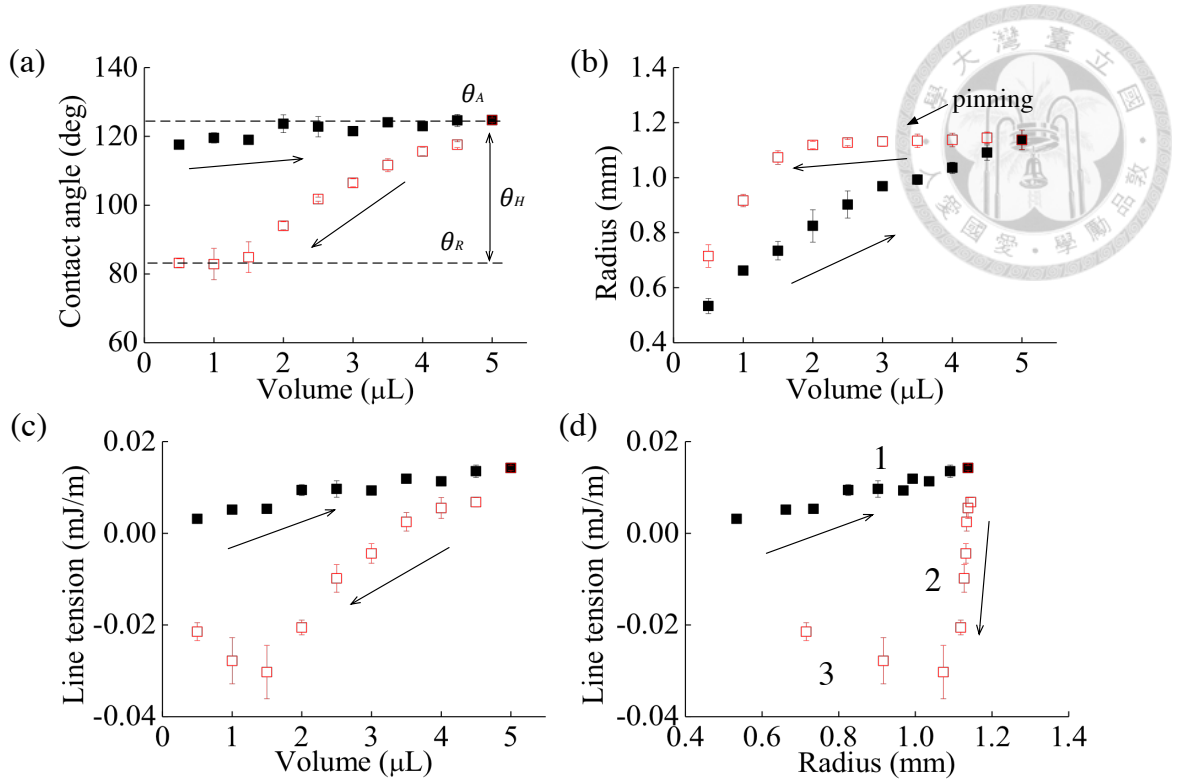


Figure 32. The measurement results of $L=25\ \mu\text{m}$, $\lambda=1.18$ and $\kappa=1.24$. (a) Contact angle hysteresis. (b) Radius of contact line versus droplet volume. (c) Line tension versus droplet volume. (d) Line tension versus radius of contact line.

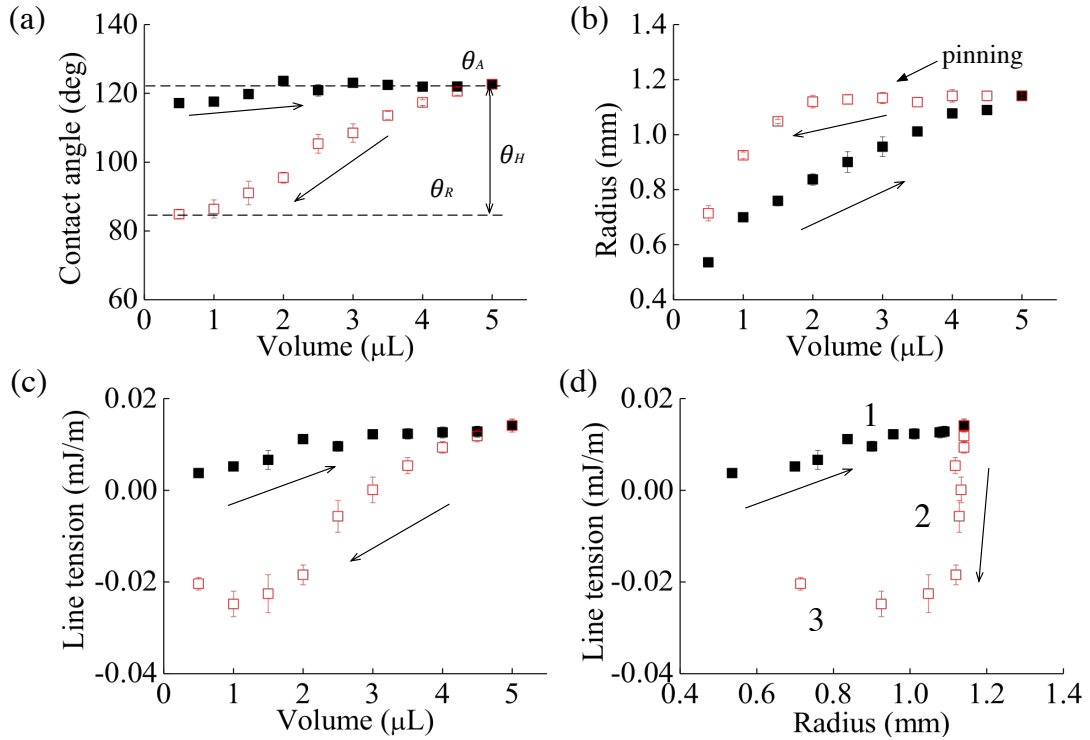


Figure 33. The measurement results of $L=25\ \mu\text{m}$, $\lambda=1.12$ and $\kappa=1.18$. (a) Contact angle hysteresis. (b) Radius of contact line versus droplet volume. (c) Line tension versus droplet volume. (d) Line tension versus radius of contact line.

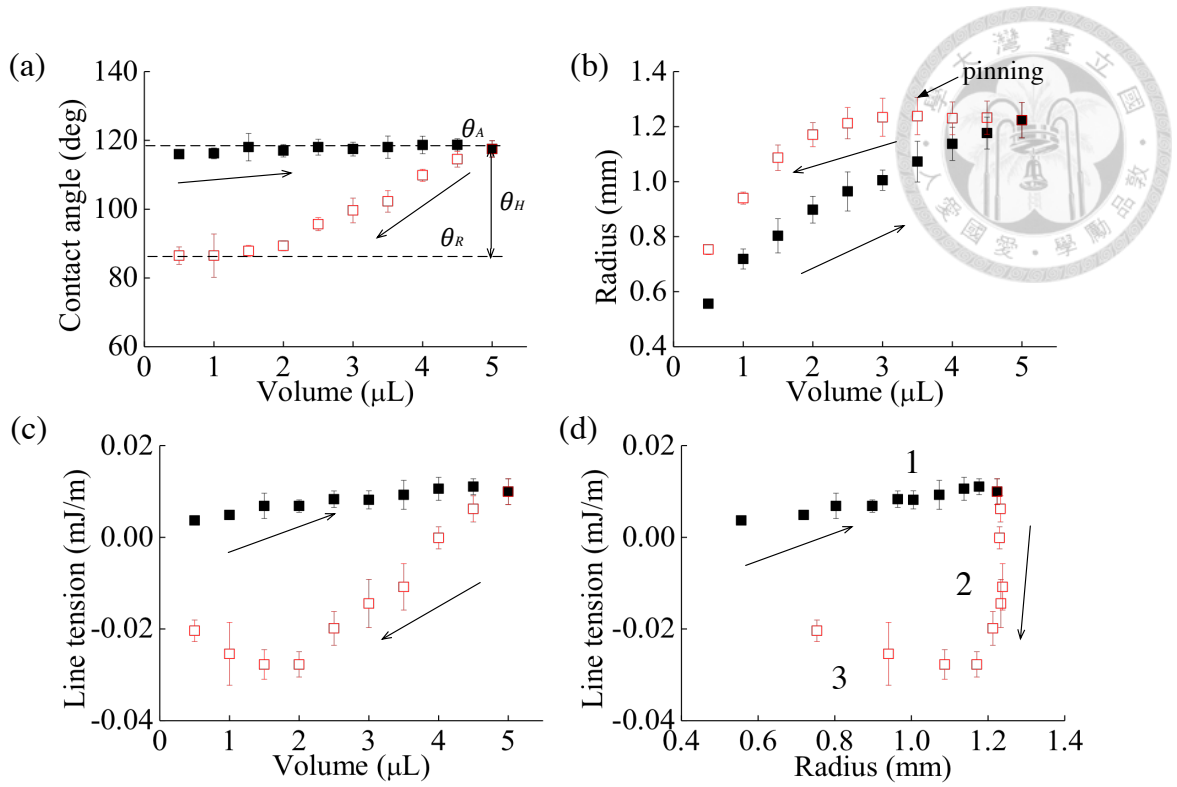


Figure 34. The measurement results of $L=25\ \mu\text{m}$, $\lambda=1.08$ and $\kappa=1.15$. (a) Contact angle hysteresis. (b) Radius of contact line versus droplet volume. (c) Line tension versus droplet volume. (d) Line tension versus radius of contact line.

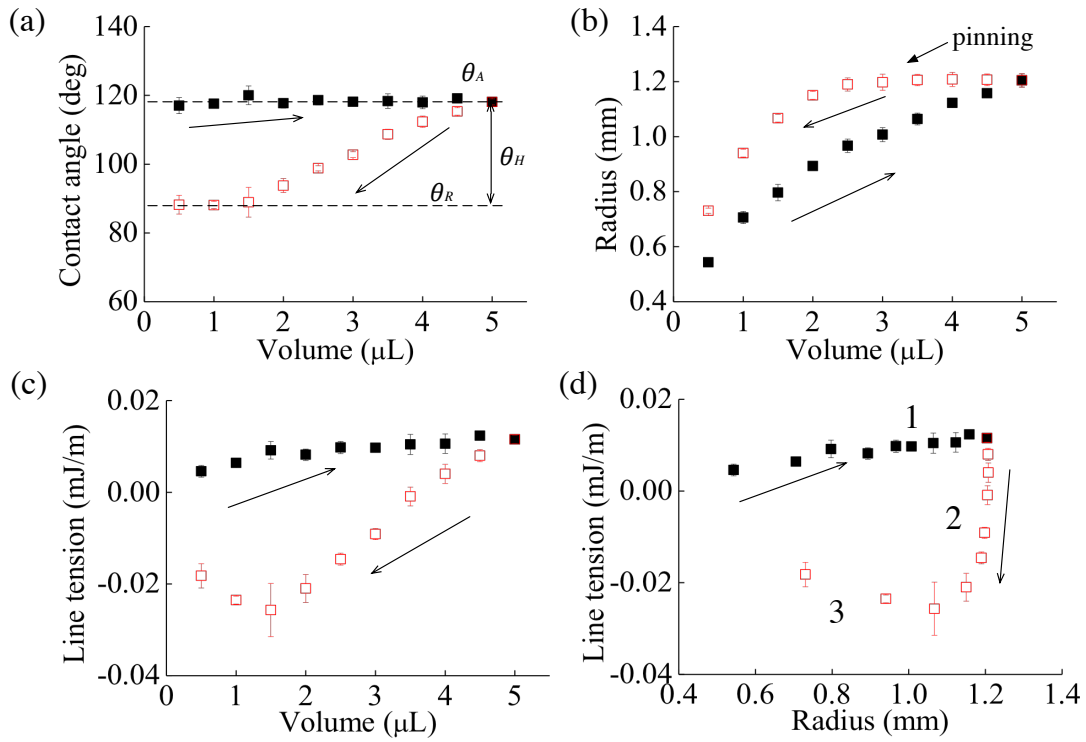


Figure 35. The measurement results of $L=25\ \mu\text{m}$, $\lambda=1.06$ and $\kappa=1.12$. (a) Contact angle hysteresis. (b) Radius of contact line versus droplet volume. (c) Line tension versus droplet volume. (d) Line tension versus radius of contact line.

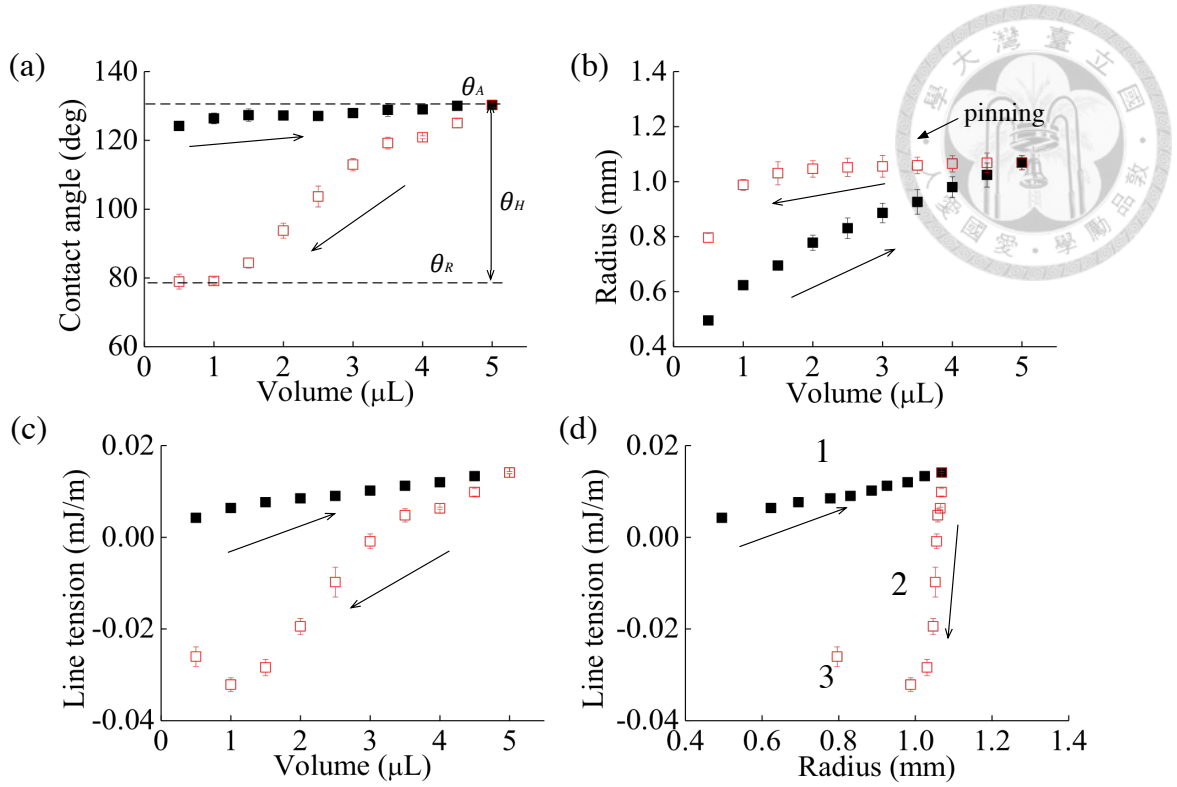


Figure 36. The measurement results of $L=30\ \mu\text{m}$, $\lambda=1.33$ and $\kappa=1.37$. (a) Contact angle hysteresis. (b) Radius of contact line versus droplet volume. (c) Line tension versus droplet volume. (d) Line tension versus radius of contact line.

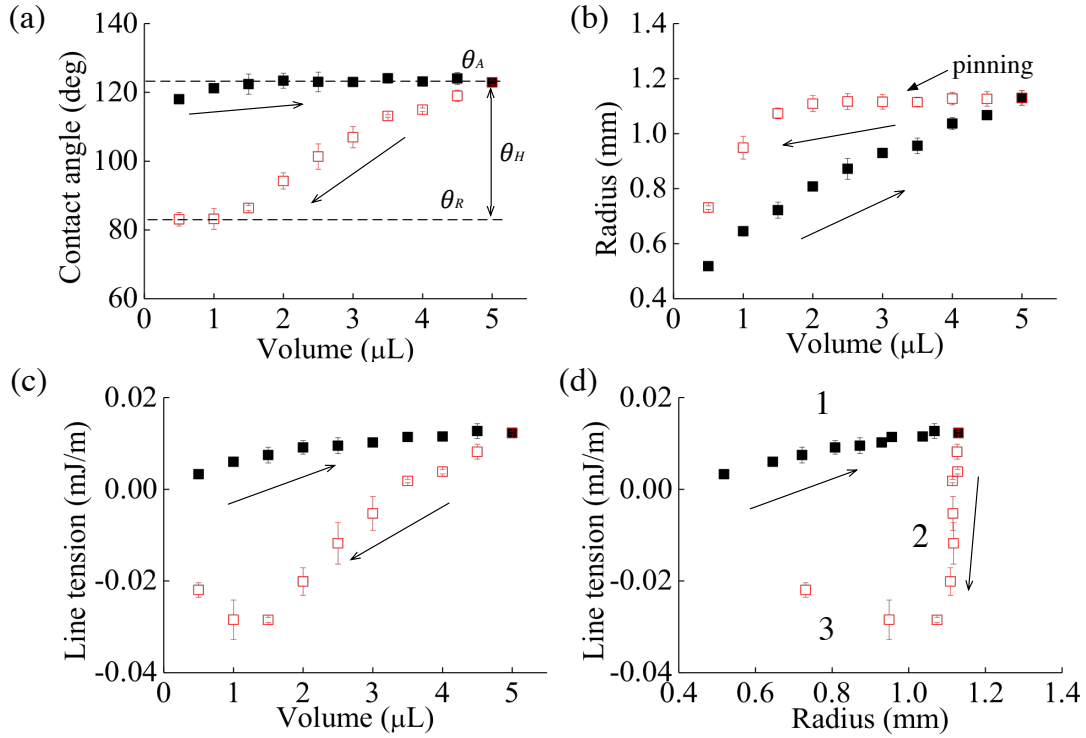


Figure 37. The measurement results of $L=30\ \mu\text{m}$, $\lambda=1.18$ and $\kappa=1.24$. (a) Contact angle hysteresis. (b) Radius of contact line versus droplet volume. (c) Line tension versus droplet volume. (d) Line tension versus radius of contact line.

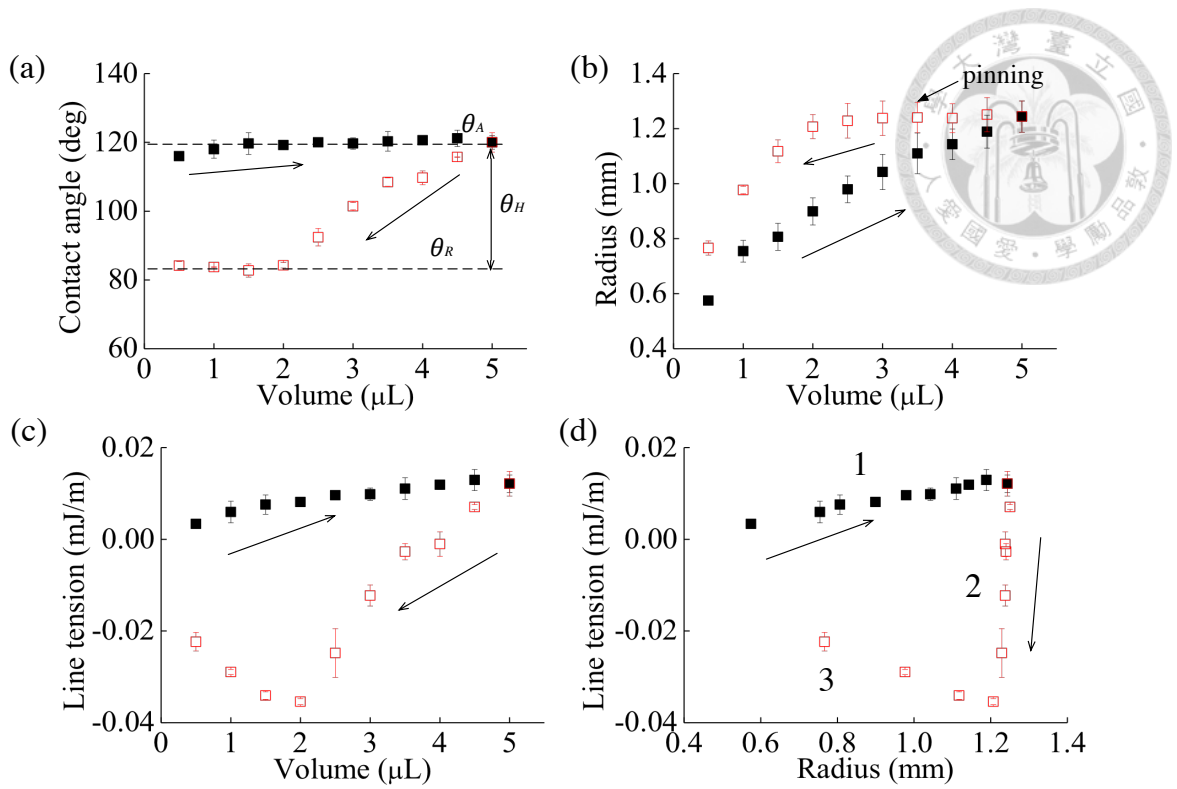


Figure 38. The measurement results of $L=30\ \mu\text{m}$, $\lambda=1.12$ and $\kappa=1.18$. (a) Contact angle hysteresis. (b) Radius of contact line versus droplet volume. (c) Line tension versus droplet volume. (d) Line tension versus radius of contact line.

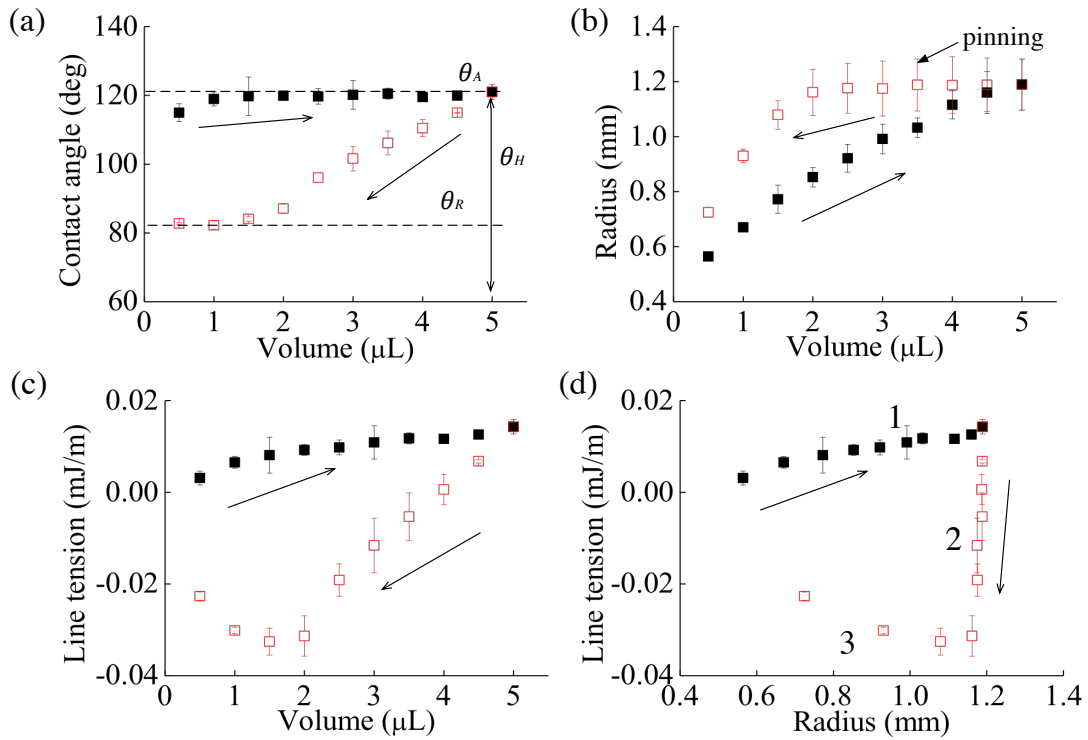


Figure 39. The measurement results of $L=30\ \mu\text{m}$, $\lambda=1.08$ and $\kappa=1.15$. (a) Contact angle hysteresis. (b) Radius of contact line versus droplet volume. (c) Line tension versus droplet volume. (d) Line tension versus radius of contact line.

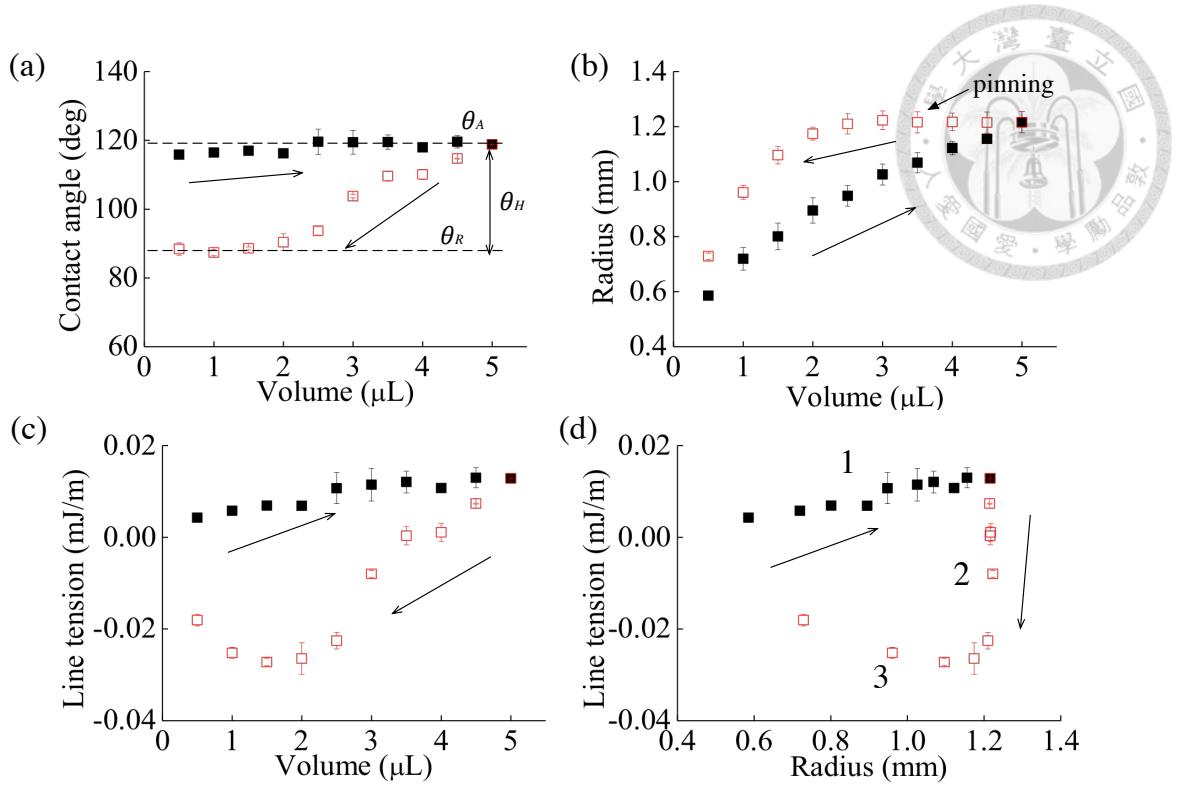


Figure 40. The measurement results of $L=30\ \mu\text{m}$, $\lambda=1.06$ and $\kappa=1.12$. (a) Contact angle hysteresis. (b) Radius of contact line versus droplet volume. (c) Line tension versus droplet volume. (d) Line tension versus radius of contact line.

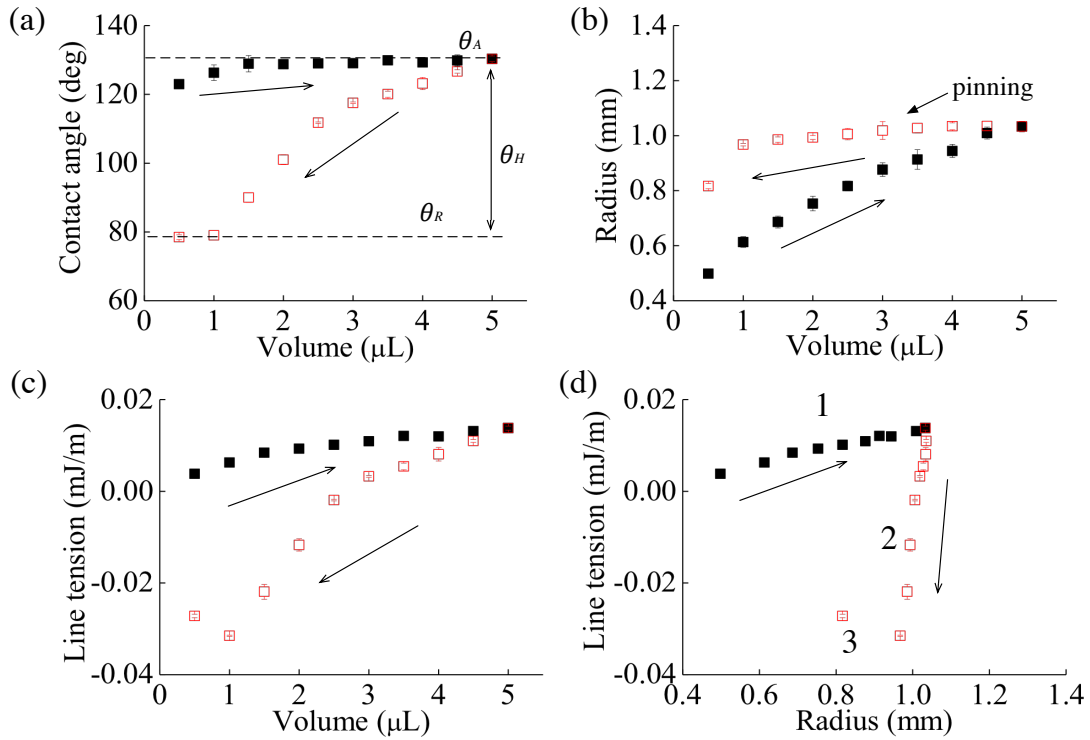


Figure 41. The measurement results of $L=35\ \mu\text{m}$, $\lambda=1.33$ and $\kappa=1.37$. (a) Contact angle hysteresis. (b) Radius of contact line versus droplet volume. (c) Line tension versus droplet volume. (d) Line tension versus radius of contact line.

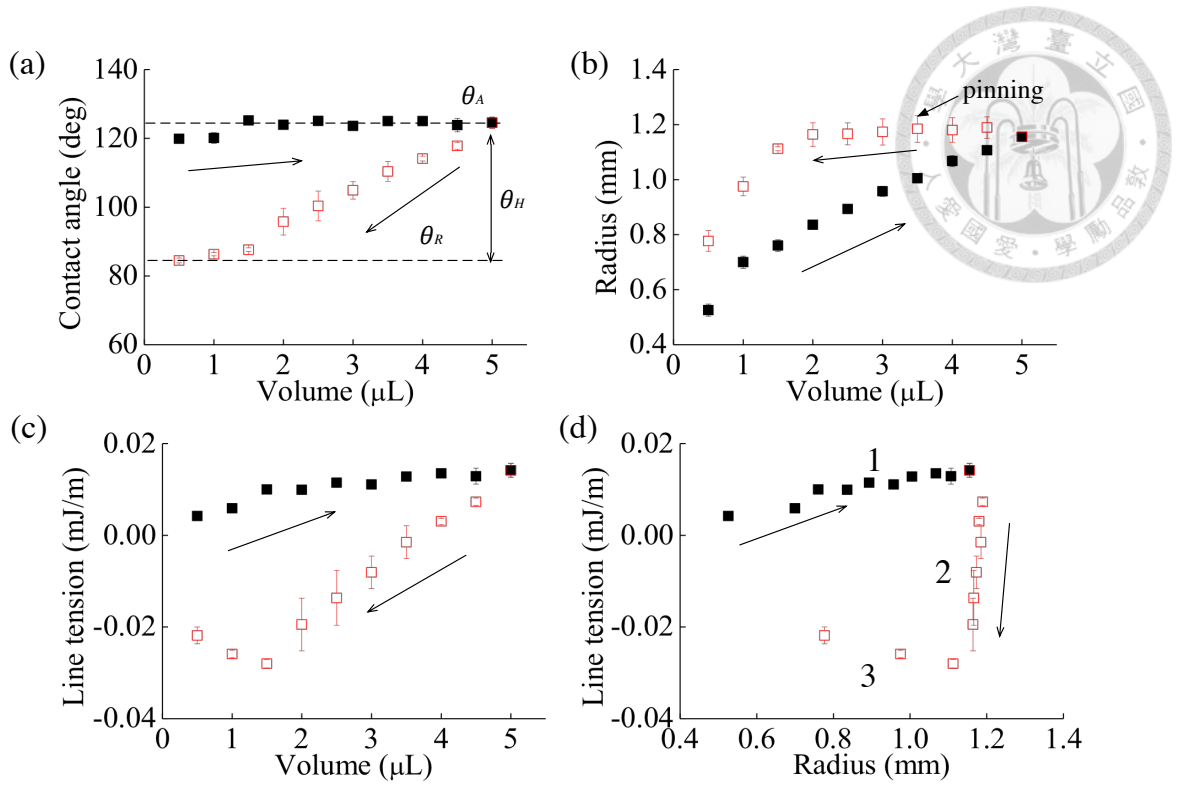


Figure 42. The measurement results of $L=35\ \mu\text{m}$, $\lambda=1.18$ and $\kappa=1.24$. (a) Contact angle hysteresis. (b) Radius of contact line versus droplet volume. (c) Line tension versus droplet volume. (d) Line tension versus radius of contact line.

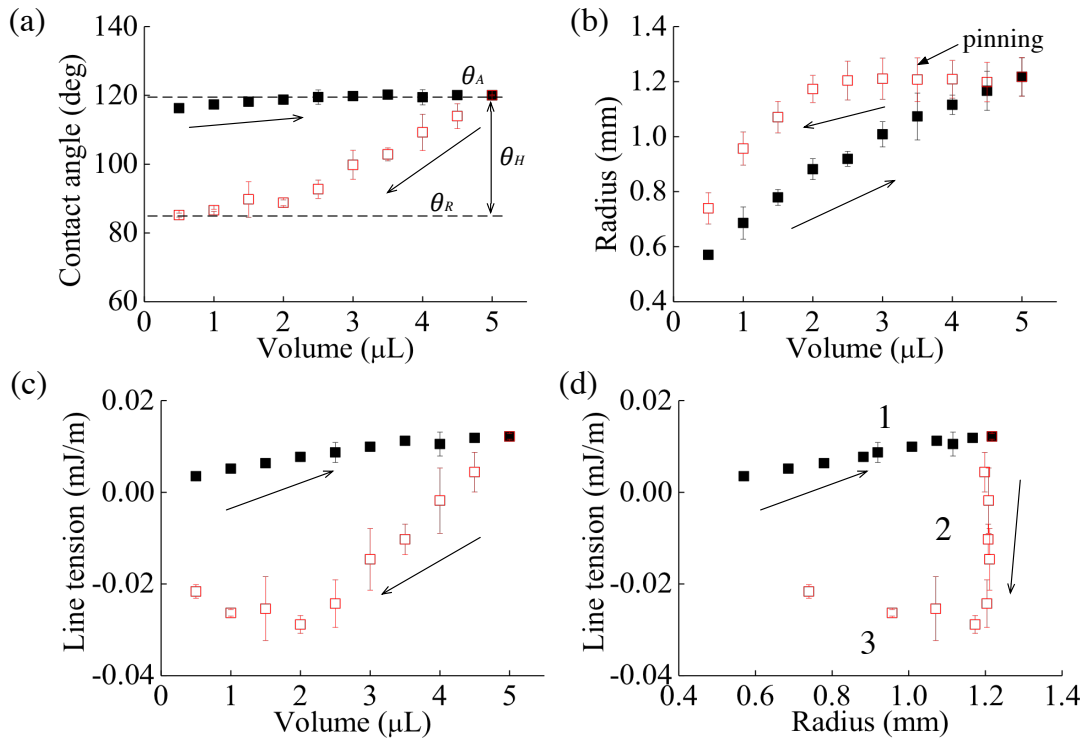


Figure 43. The measurement results of $L=35\ \mu\text{m}$, $\lambda=1.12$ and $\kappa=1.18$. (a) Contact angle hysteresis. (b) Radius of contact line versus droplet volume. (c) Line tension versus droplet volume. (d) Line tension versus radius of contact line.

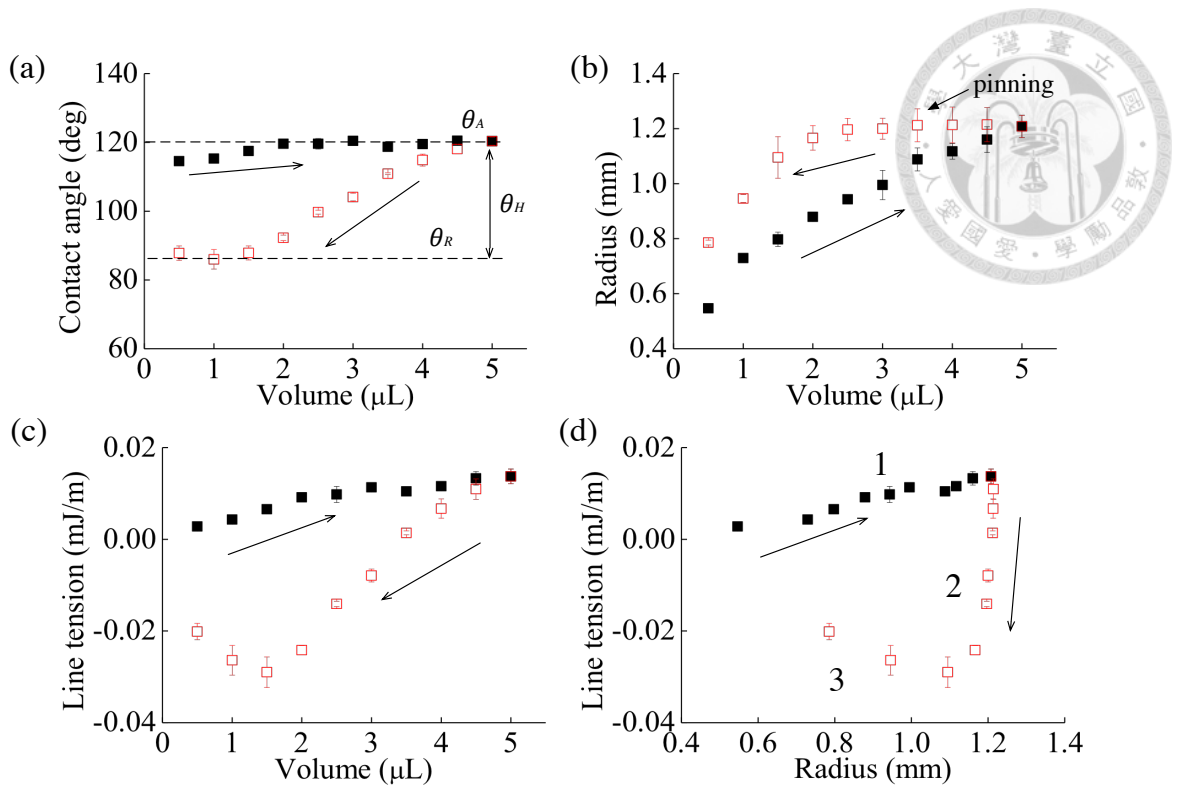


Figure 44. The measurement results of $L=35\ \mu\text{m}$, $\lambda=1.08$ and $\kappa=1.15$. (a) Contact angle hysteresis. (b) Radius of contact line versus droplet volume. (c) Line tension versus droplet volume. (d) Line tension versus radius of contact line.

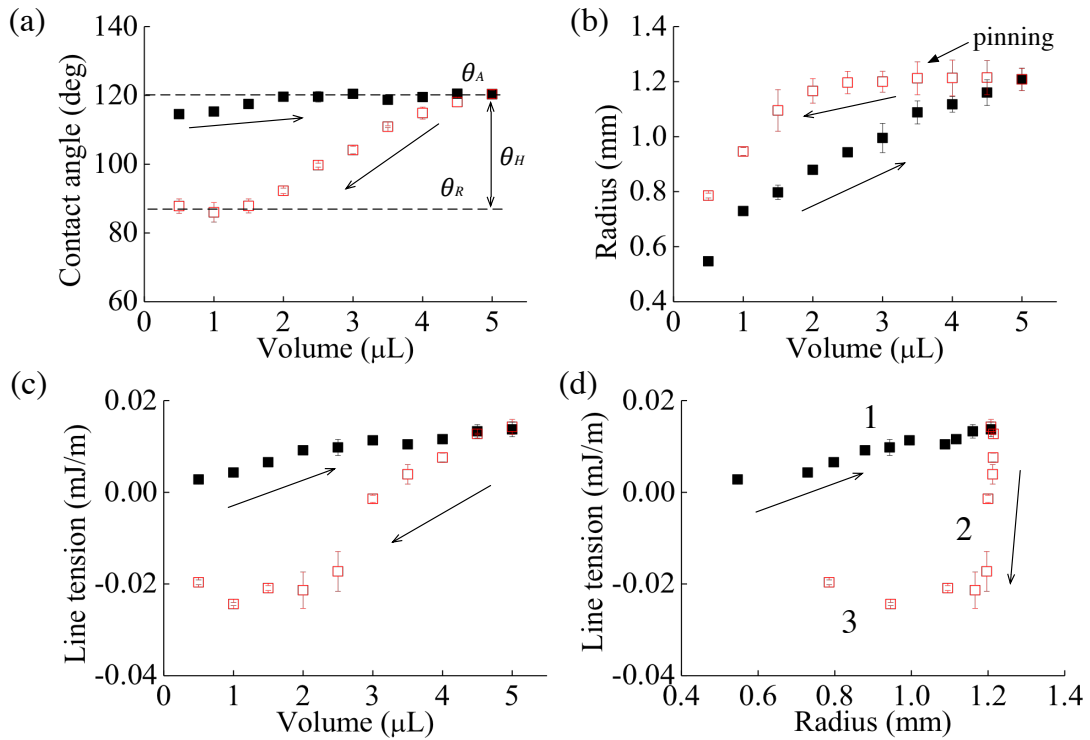


Figure 45. The measurement results of $L=35\ \mu\text{m}$, $\lambda=1.06$ and $\kappa=1.12$. (a) Contact angle hysteresis. (b) Radius of contact line versus droplet volume. (c) Line tension versus droplet volume. (d) Line tension versus radius of contact line.

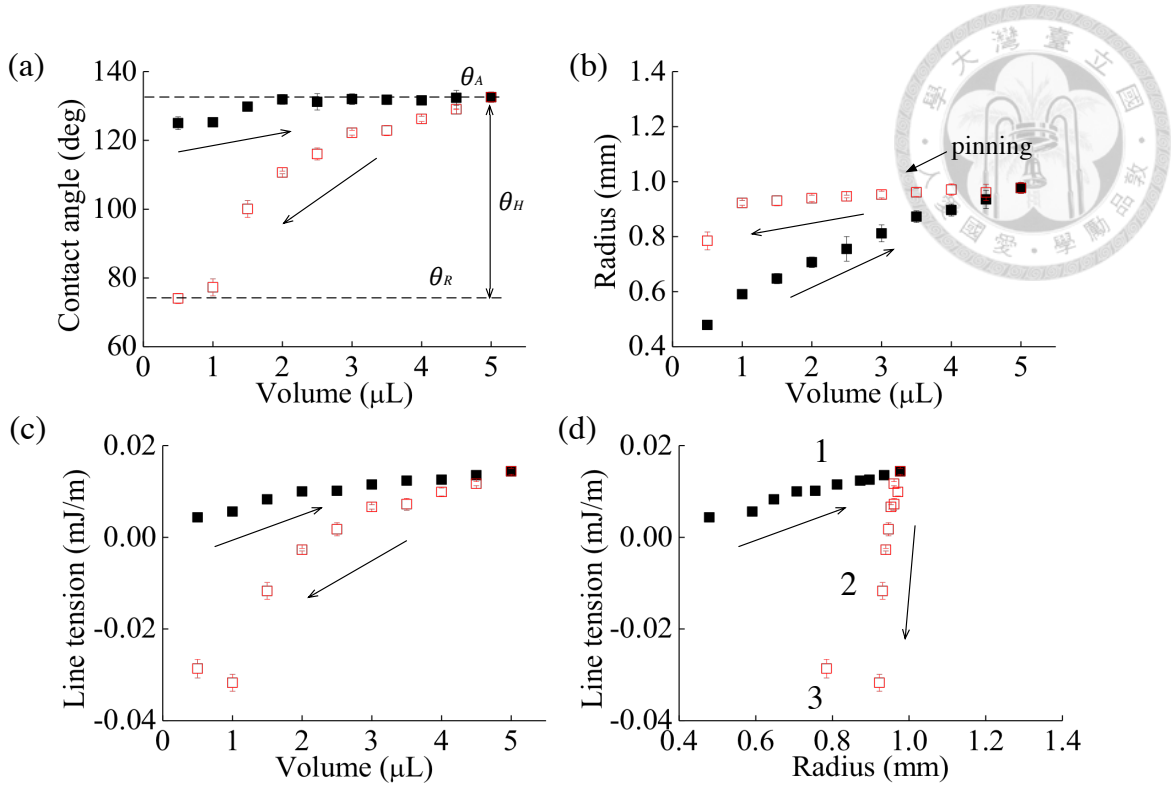


Figure 46. The measurement results of $L=40\ \mu\text{m}$, $\lambda=1.33$ and $\kappa=1.37$. (a) Contact angle hysteresis. (b) Radius of contact line versus droplet volume. (c) Line tension versus droplet volume. (d) Line tension versus radius of contact line.

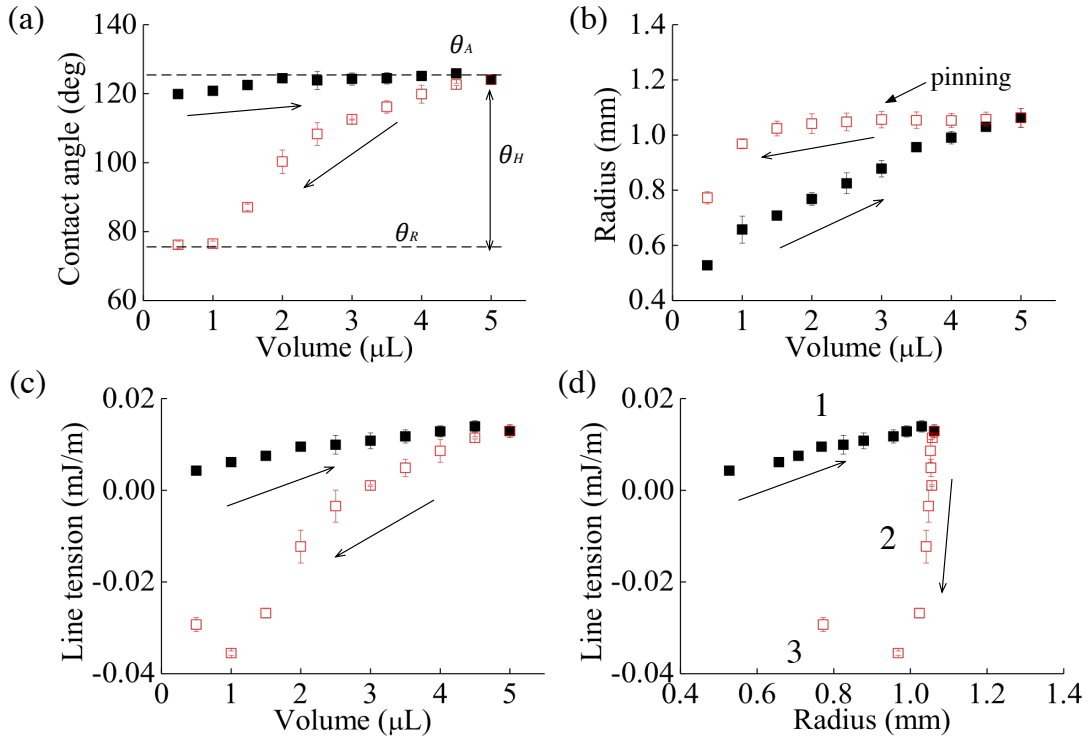


Figure 47. The measurement results of $L=40\ \mu\text{m}$, $\lambda=1.18$ and $\kappa=1.24$. (a) Contact angle hysteresis. (b) Radius of contact line versus droplet volume. (c) Line tension versus droplet volume. (d) Line tension versus radius of contact line.

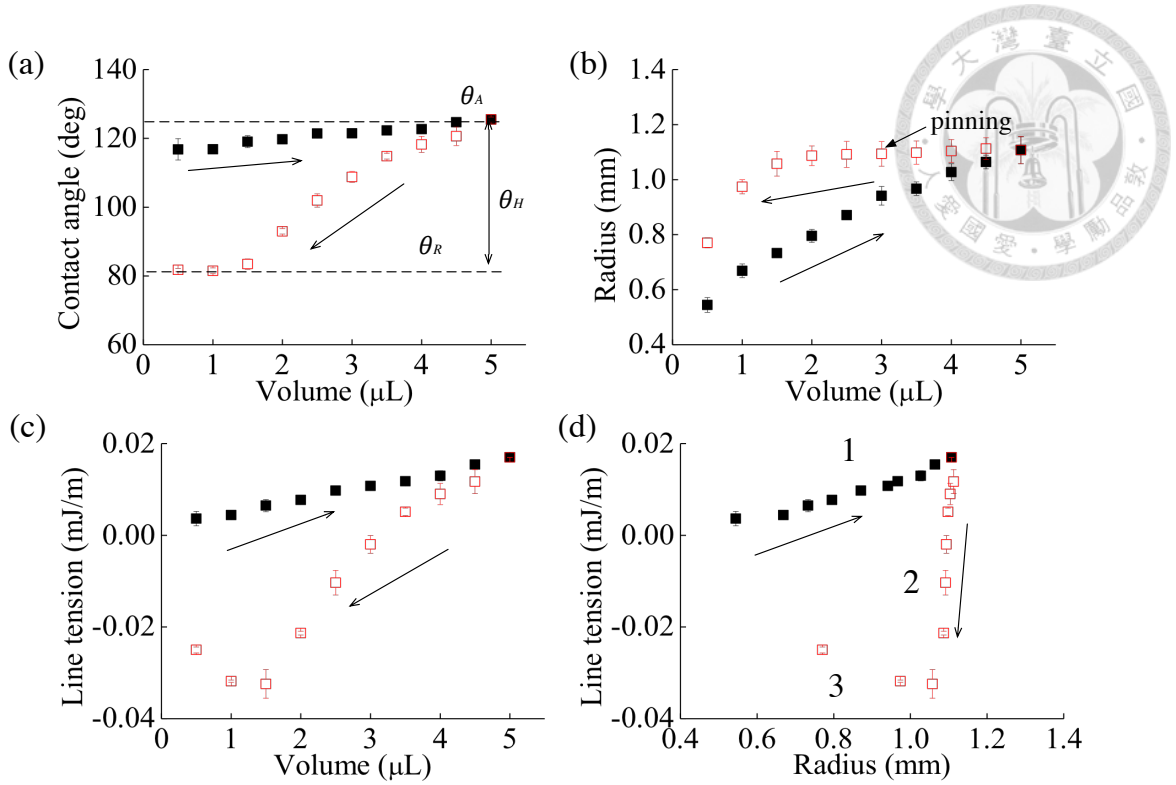


Figure 48. The measurement results of $L=40\ \mu\text{m}$, $\lambda=1.12$ and $\kappa=1.18$. (a) Contact angle hysteresis. (b) Radius of contact line versus droplet volume. (c) Line tension versus droplet volume. (d) Line tension versus radius of contact line.

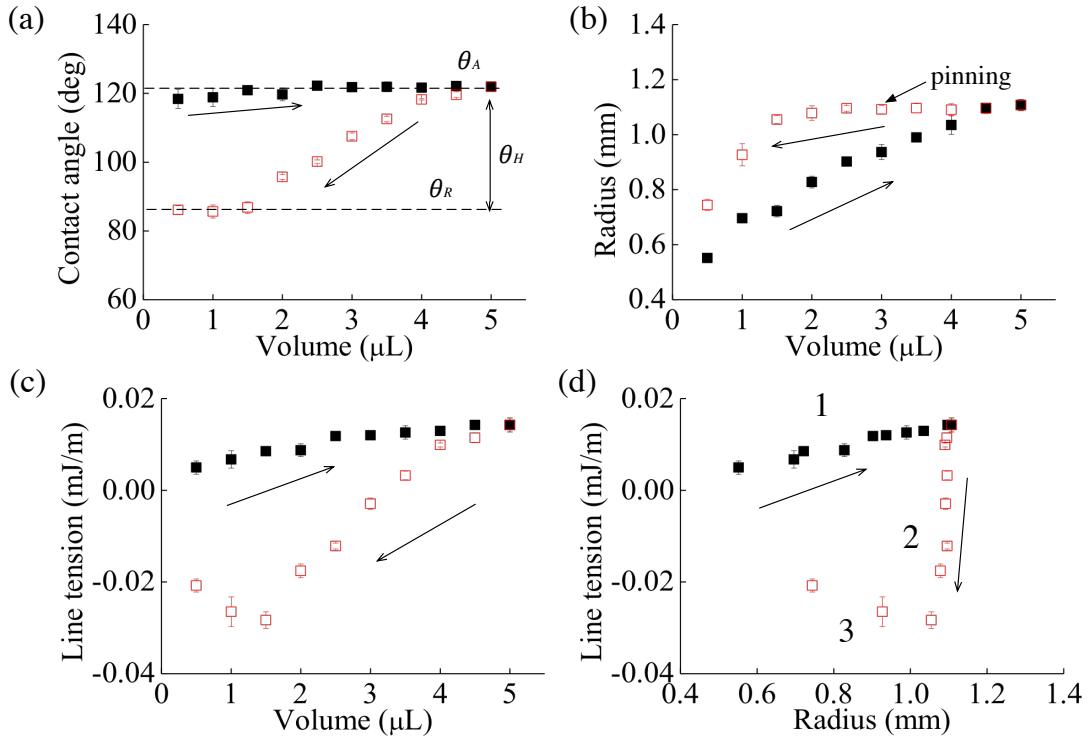


Figure 49. The measurement results of $L=40\ \mu\text{m}$, $\lambda=1.08$ and $\kappa=1.15$. (a) Contact angle hysteresis. (b) Radius of contact line versus droplet volume. (c) Line tension versus droplet volume. (d) Line tension versus radius of contact line.

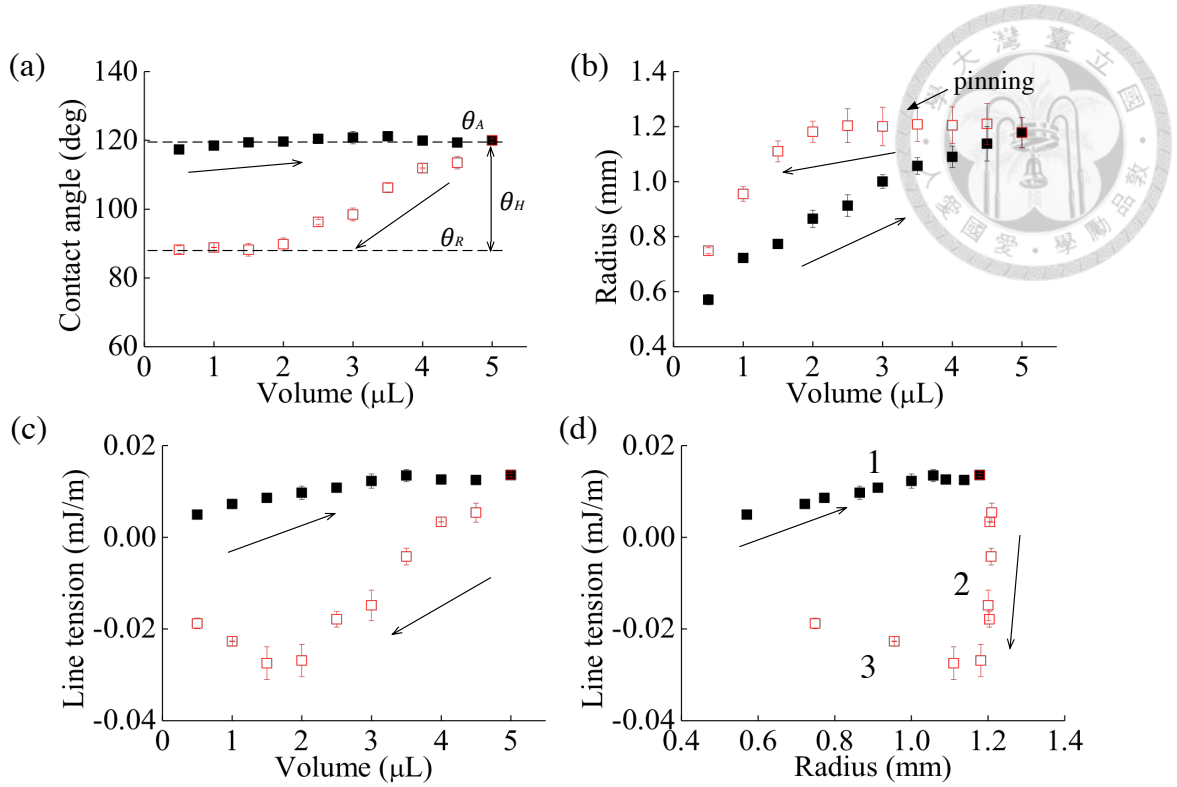


Figure 50. The measurement results of $L=40\ \mu\text{m}$, $\lambda=1.06$ and $\kappa=1.12$. (a) Contact angle hysteresis. (b) Radius of contact line versus droplet volume. (c) Line tension versus droplet volume. (d) Line tension versus radius of contact line.

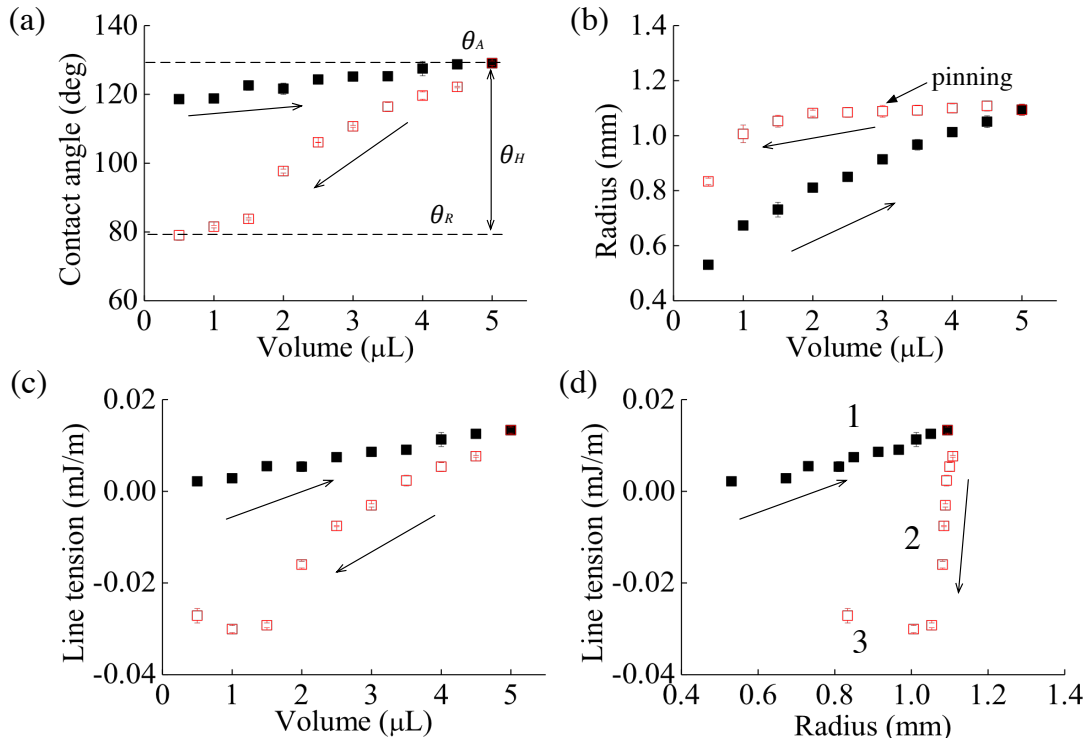


Figure 51. The measurement results of $L=45\ \mu\text{m}$, $\lambda=1.33$ and $\kappa=1.37$. (a) Contact angle hysteresis. (b) Radius of contact line versus droplet volume. (c) Line tension versus droplet volume. (d) Line tension versus radius of contact line.

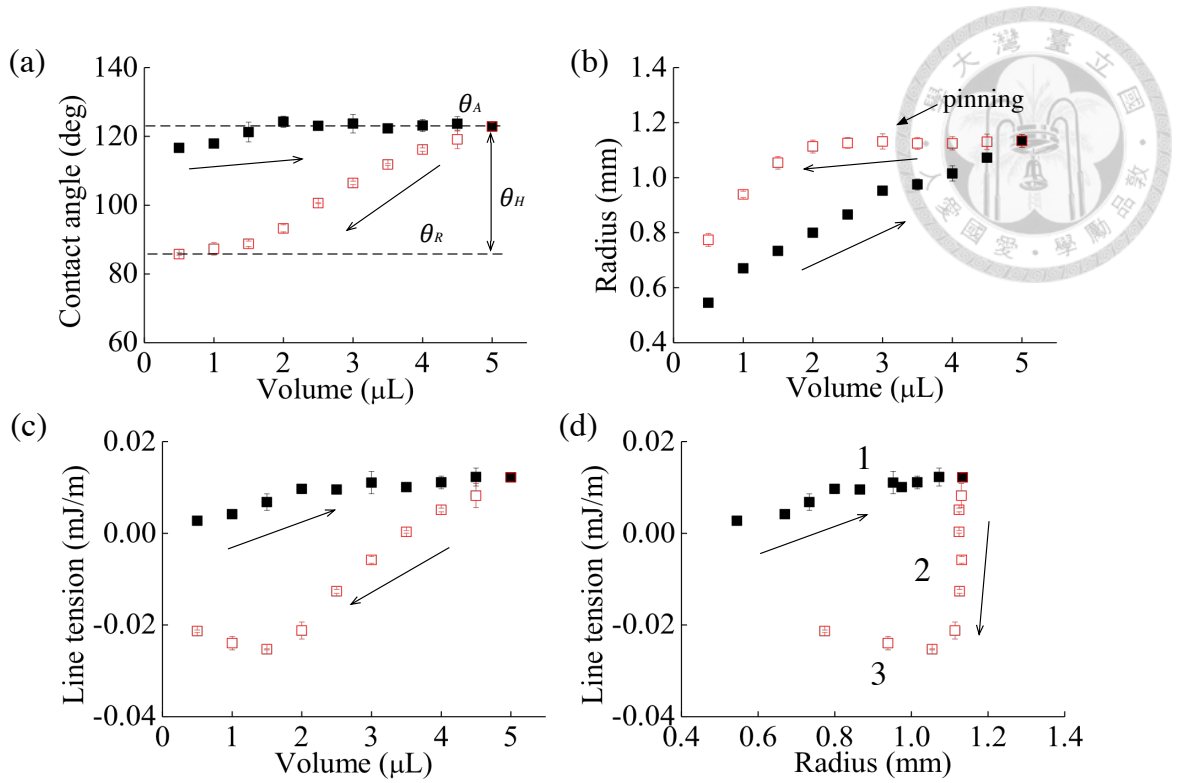


Figure 52. The measurement results of $L=45 \mu\text{m}$, $\lambda=1.18$ and $\kappa=1.24$. (a) Contact angle hysteresis. (b) Radius of contact line versus droplet volume. (c) Line tension versus droplet volume. (d) Line tension versus radius of contact line.

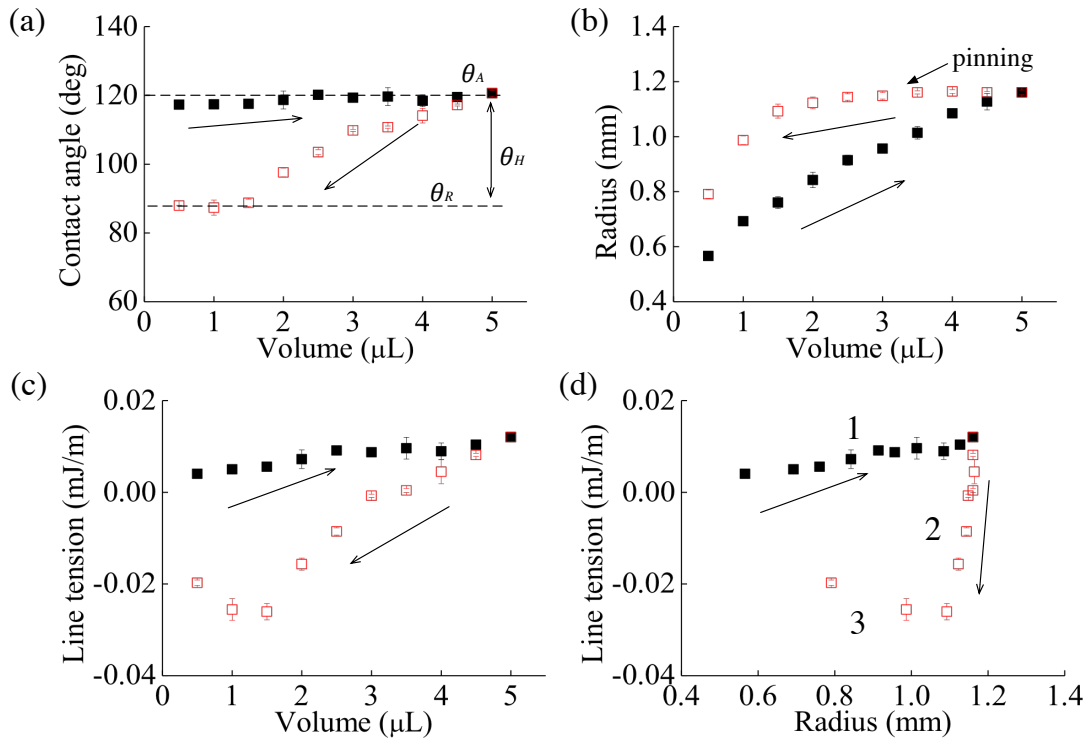


Figure 53. The measurement results of $L=45 \mu\text{m}$, $\lambda=1.12$ and $\kappa=1.18$. (a) Contact angle hysteresis. (b) Radius of contact line versus droplet volume. (c) Line tension versus droplet volume. (d) Line tension versus radius of contact line.

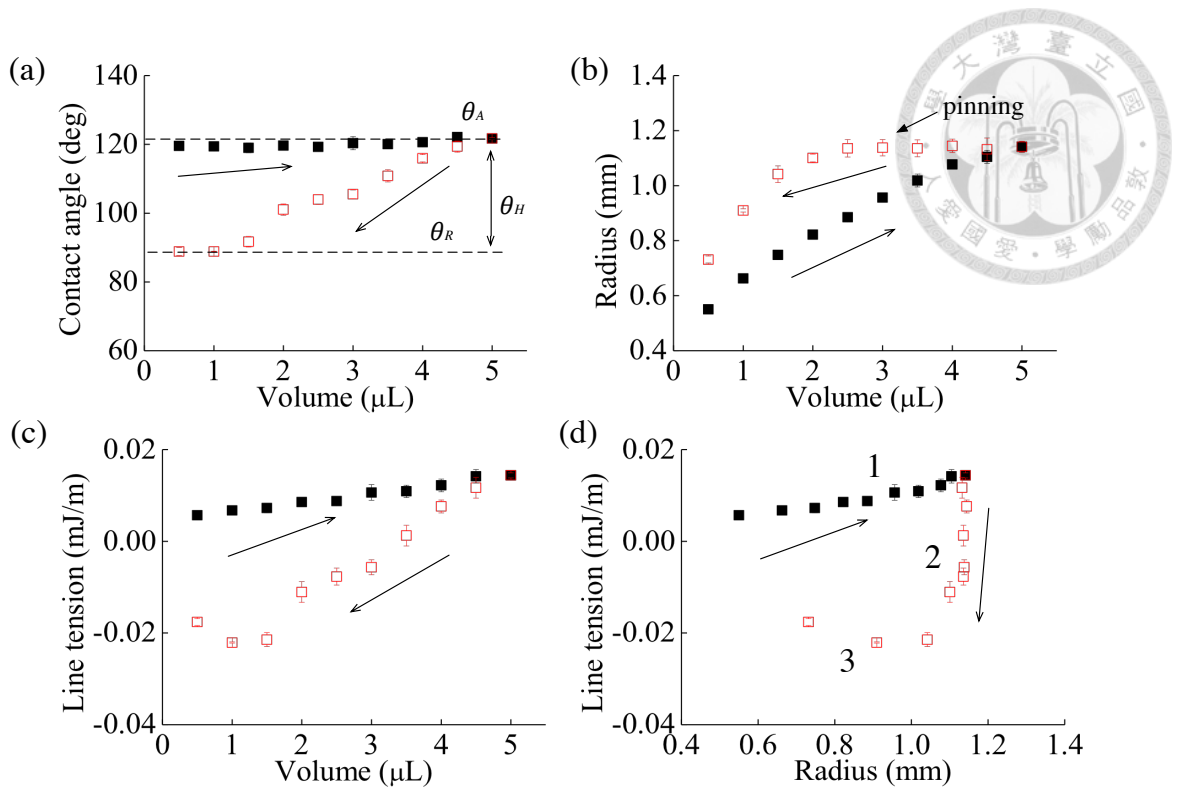


Figure 54. The measurement results of $L=45\ \mu\text{m}$, $\lambda=1.08$ and $\kappa=1.15$. (a) Contact angle hysteresis. (b) Radius of contact line versus droplet volume. (c) Line tension versus droplet volume. (d) Line tension versus radius of contact line.

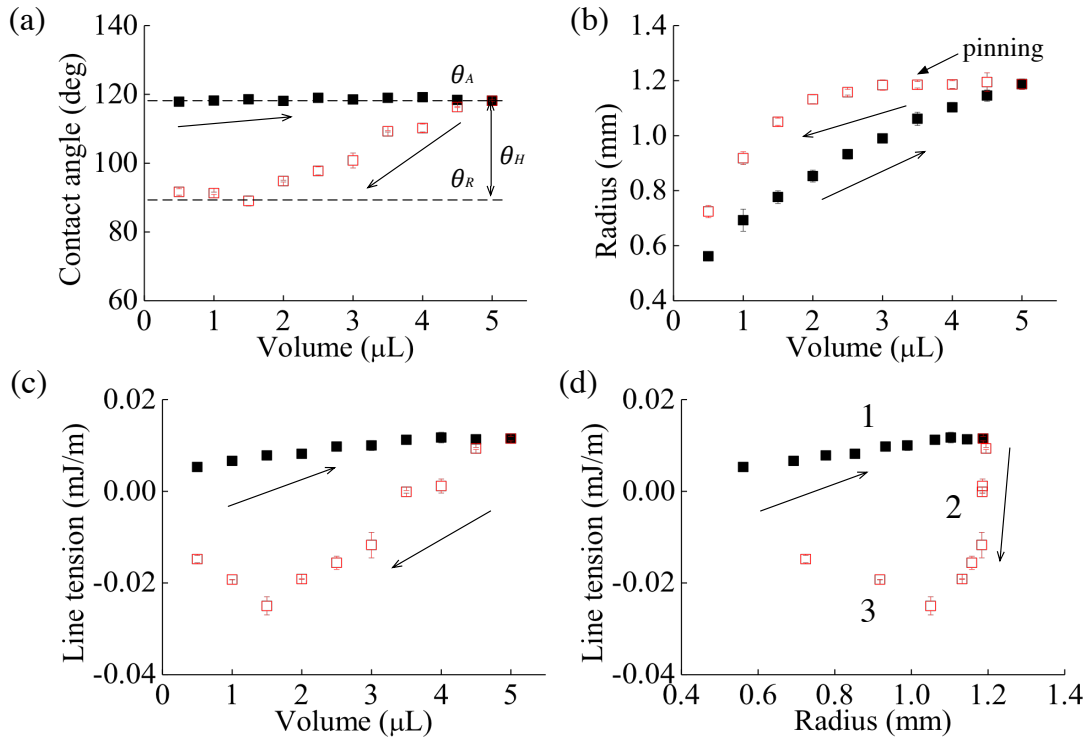


Figure 55. The measurement results of $L=45\ \mu\text{m}$, $\lambda=1.06$ and $\kappa=1.12$. (a) Contact angle hysteresis. (b) Radius of contact line versus droplet volume. (c) Line tension versus droplet volume. (d) Line tension versus radius of contact line.

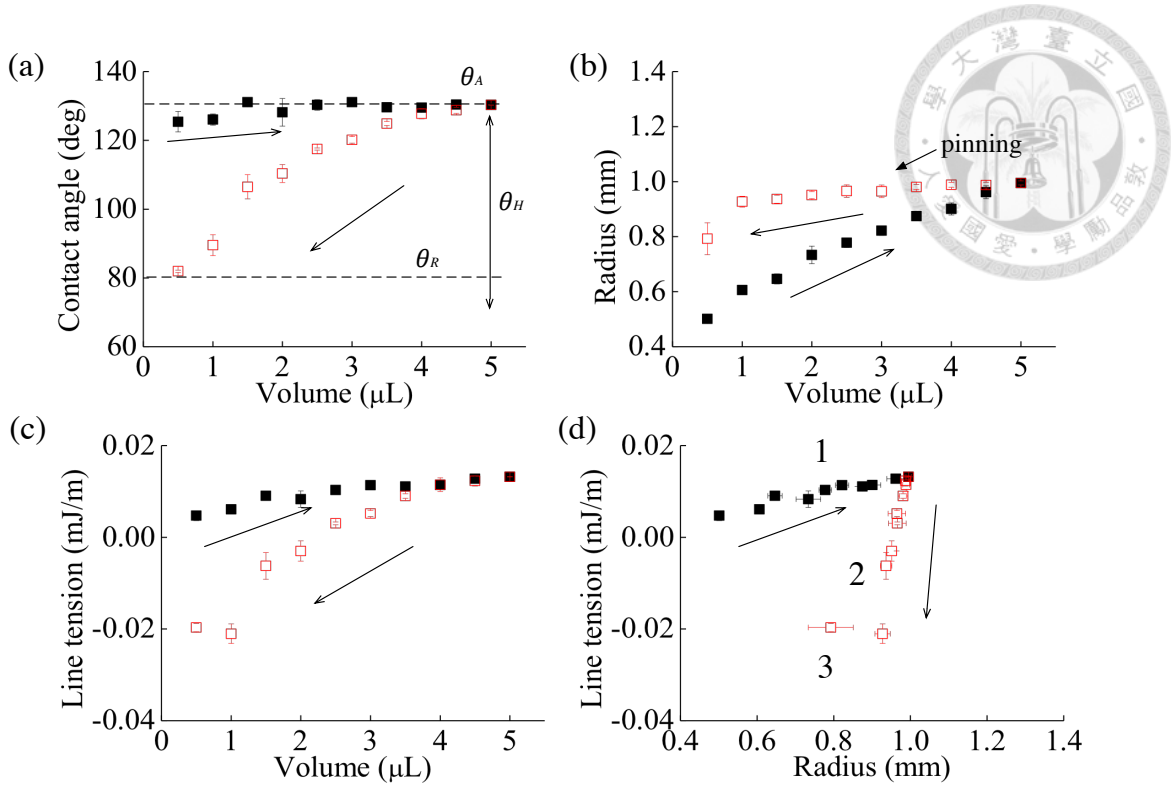


Figure 56. The measurement results of $L=50\ \mu\text{m}$, $\lambda=1.33$ and $\kappa=1.37$. (a) Contact angle hysteresis. (b) Radius of contact line versus droplet volume. (c) Line tension versus droplet volume. (d) Line tension versus radius of contact line.

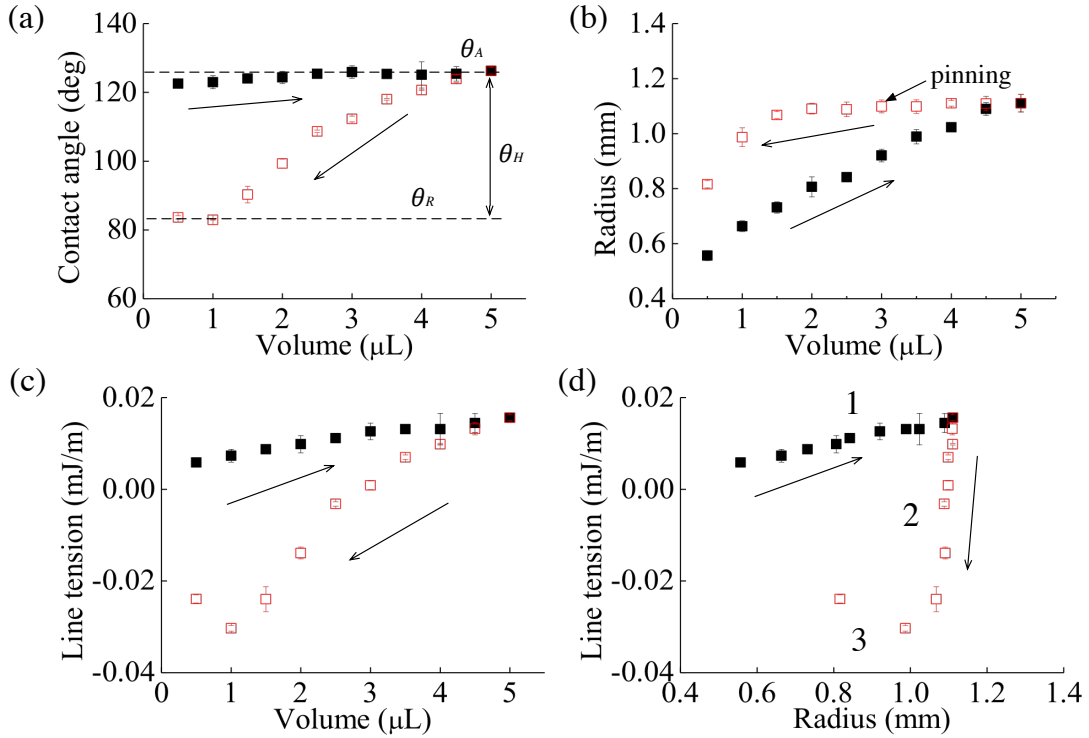


Figure 57. The measurement results of $L=50\ \mu\text{m}$, $\lambda=1.18$ and $\kappa=1.24$. (a) Contact angle hysteresis. (b) Radius of contact line versus droplet volume. (c) Line tension versus droplet volume. (d) Line tension versus radius of contact line.

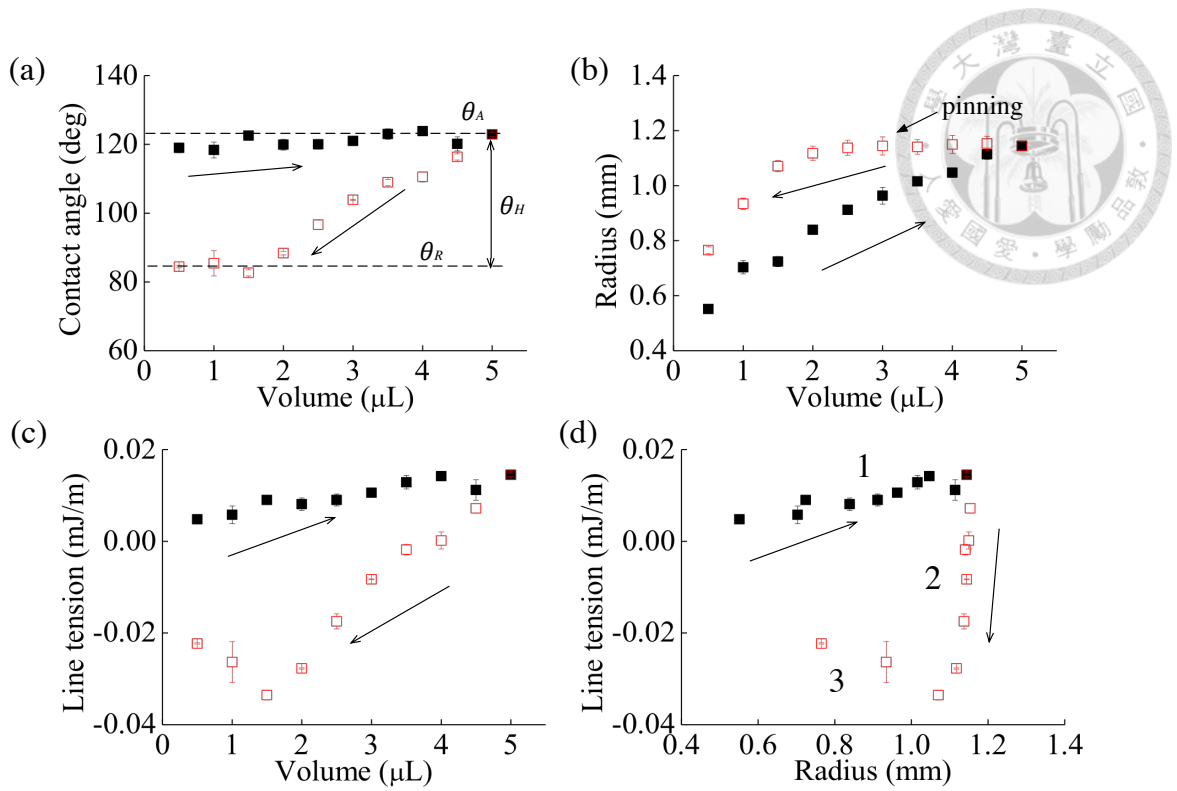


Figure 58. The measurement results of $L=50\ \mu\text{m}$, $\lambda=1.12$ and $\kappa=1.18$. (a) Contact angle hysteresis. (b) Radius of contact line versus droplet volume. (c) Line tension versus droplet volume. (d) Line tension versus radius of contact line.

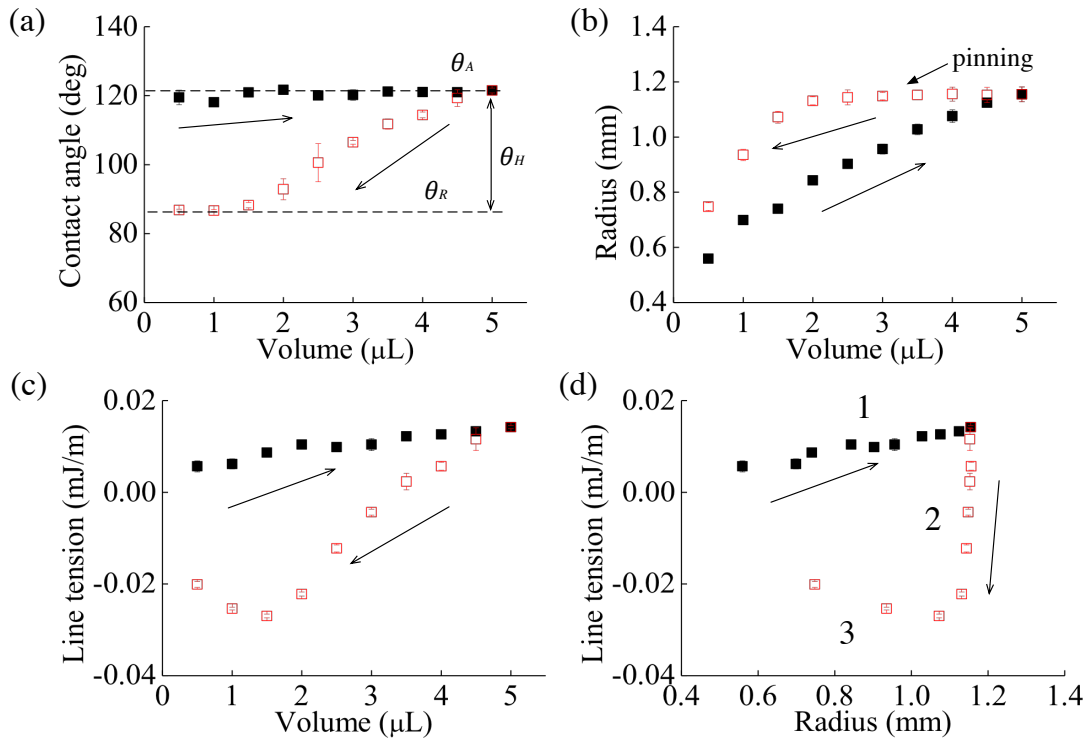


Figure 59. The measurement results of $L=50\ \mu\text{m}$, $\lambda=1.08$ and $\kappa=1.15$. (a) Contact angle hysteresis. (b) Radius of contact line versus droplet volume. (c) Line tension versus droplet volume. (d) Line tension versus radius of contact line.

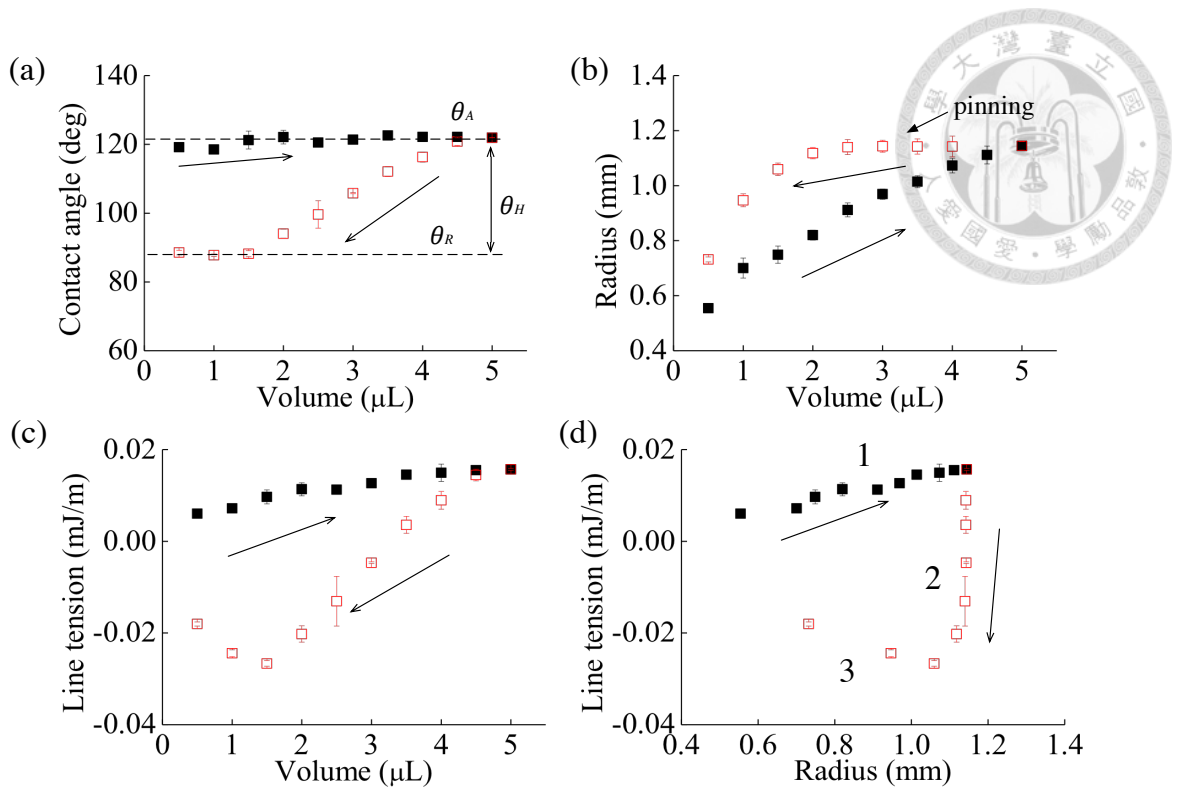


Figure 60. The measurement results of $L=50 \mu\text{m}$, $\lambda=1.06$ and $\kappa=1.12x$. (a) Contact angle hysteresis. (b) Radius of contact line versus droplet volume. (c) Line tension versus droplet volume. (d) Line tension versus radius of contact line.

.Chapter 4 Photo-controllable contact angle hysteresis

on an artificial Azo-IPN petal



4.1 Introduction

The droplet-solid interaction has been widely explored for applications in self-cleaning, anti-icing, anti-fouling, and microfluidics [62-65]. Heterogeneous surfaces have been modeled [66-72] and engineered to mimic the lotus-effect [23], featuring super-hydrophobicity with low droplet hysteresis, and the petal effect [73-74], known as hydrophobicity with high droplet adhesion. The hydrophobicity and hysteresis can be measured by the static contact angle and contact angle hysteresis, respectively, of a droplet on its resting surface. A petal-like surface can attain a large volume of droplet by forming a large contact angle and contact angle hysteresis. The sliding velocity of a droplet on an inclined surface can also be controlled by exploiting the contact angle hysteresis. To manipulate the droplet dynamics on an engineered surface, it is of great interest to actively modulate the aforementioned surface properties. However, reversibly changing the contact angle hysteresis remains challenging.

To realize controllable contact angle and its hysteresis, this paper presents the development of a photo-responsive artificial petal and its validation test. Specifically, the hierarchical structure of nano-folding on micro-hills was copied from a rose petal and made of photo-responsive polymer.

4.2 Material and fabrication

Azobenzene (Azo) moiety, which has reversible trans-to-cis isomerization under UV (typically 365 nm) and visible light (in the range of 400-550 nm) exposure [75-76], is used to develop the interpenetrating polymer network (IPN) in the photo-responsive

artificial petal. The formation of such an interlocked structure allows us to prepare a wide range of homogeneous polymer mixtures with versatile advantageous properties [79-82]. The photo-responsive Azo-IPN is prepared from the copolymer of azobenzene moiety (AZ-CP) and polydimethylsiloxane (PDMS; Sil-More Industrial Ltd.). The AZ-CP copolymer is synthesized by mixing 0.5 mM of azo dye Disperse Red I Methacrylate (azo; Sigma-Aldrich), 0.3 mM of 1,3,5-tris(undec-10-en-1-yloxy) benzene (TB; Sigma-Aldrich), and 3 mM of 4-Methoxyphenyl 4-(3-buten-1-yloxy) benzoate (MB; Sigma-Aldrich) in 3 mL toluene with azobisisobutyronitrile (AIBN; Sigma-Aldrich). Polydimethylsiloxane is then added and stir-mixed for one hour to form IPN structure. Next, we prepare a petal mold by depositing parylene onto a Tineke rose petal for 3 hours and remove the petal with acetone. The Azo-IPN solvent is spin-coated onto the mold and thermally cured at 90 °C. The cured Azo-IPN artificial petal is peeled off from the parylene mold. Figure 61 shows the successful creation of cavities on the parylene mold with micro-hills of $\sim 22\ \mu\text{m}$ base diameter and nano-folds of $\sim 83\ \text{nm}$ characteristic width. Comparing with real rose (Figure 62), these fine features are intactly transferred onto the Azo-IPN surface.

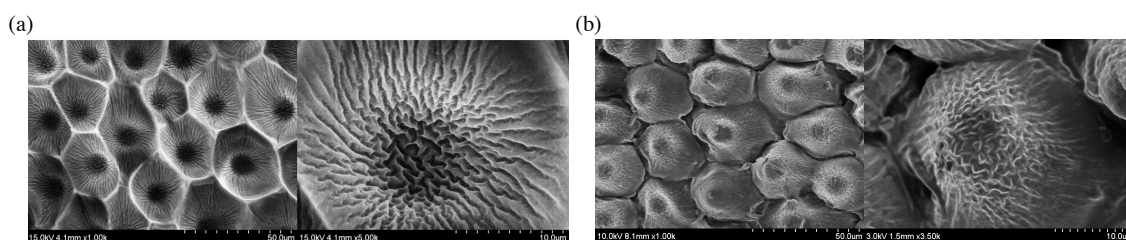


Figure 61. Top-view images, taken with scanning electron microscopy, of the micro-hills and nano-folds on: (a) the cavities in the parylene mold, (b) the Azo-IPN artificial petal.

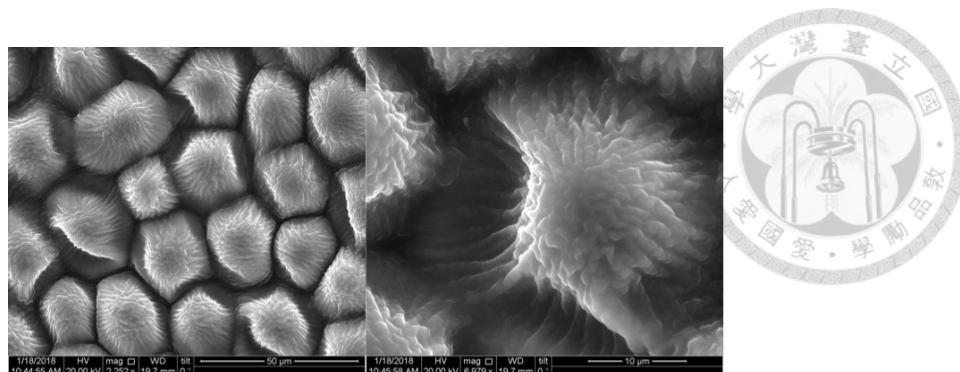


Figure 62. Top-view images, taken with scanning electron microscopy of real rose petal.

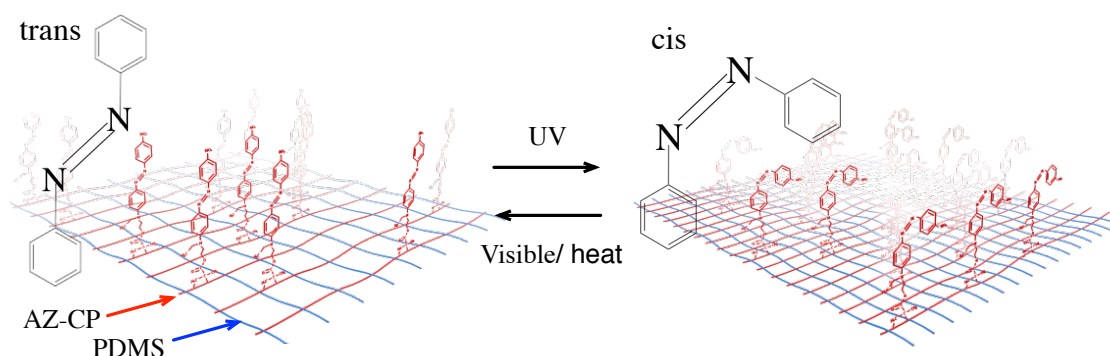


Figure 63. Schematic transition of trans-cis isomerization on the surface of the Azo-IPN artificial petal.

The dipole moment of trans- and cis-azobenzene is $\mu_{\text{trans}}=3.42$ D and $\mu_{\text{cis}}=5.72$ D, respectively [71]. If the dipole moment of azobenzene transfers from low to high, the surface free energy increases correspondingly to diminish the contact angle. The contact angle also changes with the state of the nitrogen double bond ($\text{N}=\text{N}$), as illustrated in Figure 63. When the azobenzene moieties are in their trans consistent, the hydrophobic benzene rings extend out from the petal surface. Upon UV exposure, the azobenzene moieties turn into their cis form in which the nitrogen double bonds are exposed, associating water molecules with hydrogen bonds to make the fabricated petal surface more hydrophilic. By applying heat or visible-light exposure, the azobenzene can be transformed back to its trans consistent, restoring its surface free energy.

We exposed the petal to UV-light of 365 nm wavelength and 15 mW/cm² intensity and measured its absorption spectrum as shown in Figure 64a. The UV-visible spectra confirm the photo-responsivity of Azo-IPN; how the peak moves from 465 nm to 420 nm over time confirms that the accumulated UV exposure dose changes the petal surface free energy during the trans-cis transition. By subsequently applying the green light of 530 nm wavelength, which provides relative high absorption rate for the cis-azobenzene, and 20 mW/cm² intensity, the absorption spectrum measured over time reveals a reversed peak evolution back to 465 nm, validating the speculated reversible cis-trans transition, as shown in Figure 64b.

4.3 Measurement procedure of the contact angle hysteresis

We deposited a drop of 0.5 μ L deionized water on both a real rose petal and the fabricated artificial petal using a syringe. A lateral CCD camera image was analyzed to measure the static contact angle as $129.4 \pm 1.5^\circ$ and $135.2 \pm 1.6^\circ$ for the real and the artificial petal, respectively, as summarized in Table 3. The error represents the standard deviation of five-time measurement on different locations of each sample. The contact angle of the artificial petal decreased to $99.2 \pm 0.9^\circ$ after the 180 sec UV-light exposure and then increased back to $140.9 \pm 1.8^\circ$ with a subsequent green light exposure of 180 sec (Figure 65). This later increment from its original static angle of $135.2 \pm 1.6^\circ$ indicates that more cis-azobenzene moieties were turned into trans state to give greater surface energy and even more hydrophobic artificial petal.

The contact angle evolution of a deionized water droplet when its volume was changed on a real rose petal and the fabricated Azo-IPN petal upon exposure of different lights are shown in Figure 65. The droplet volume was increased from 0.5 μ L to 5 μ L at 0.5 μ L increment and then decreased back to 0.5 μ L, as indicated by the arrows. On the real rose petal, the contact angle increased with the volume from 127.1° but saturated to

135.2±0.5° when the droplet volume was over 2 μL , as shown in Figure 65a. This saturation angle, marked by the dashed line, is defined as the advancing angle, θ_a . Under the same experimental conditions, we measured $\theta_a=140\pm1.5^\circ$ on the artificial Azo-IPN petal without exposure (Figure 65b). This θ_a decreased to 110.6±0.6° under the UV light exposure (Figure 65c) and changed back to 141.2±1.1° after the green light is applied again (Figure 65d). When we reduced the droplet volume, saturation upon the contact angle diminishment was observed only on the fabricated petal under the UV exposure. Therefore, we can determine the receding angle, $\theta_r=60.3\pm0.8^\circ$ (the lower dashed line in Figure 65c). This specifies a definite contact angle hysteresis, θ_h , as 50.3±0.6°. In contrast, we measured monotonic decrease of the contact angle with the volume in the rest three cases.

In general, the contact angle characteristics on the fabricated Azo-IPN petal is similar to that on the real rose petal in the aspect that they both exhibit large contact angle hysteresis and hence strong petal effect. However, the contact angle is tunable only on the artificial petal. Under the exposure of UV light, the trans-to-cis azobenzene transition increases the surface free energy to degrade the petal effect as the fabricated surface is no longer superhydrophobic. In addition to the contact angle, controllability of the petal surface property under UV exposure can also be revealed when we examine the diameter of droplet contact area, $2r$, in the inset images of Figure 4. Here, the droplet volume is 5 μL and 0.5 μL in the top and bottom insets, respectively, and the fact that the $2r$ remained nearly unchanged in Figures 65a, b, and d indicates that the droplet was pinned on the surface. In contrast, $2r$ diminished when the droplet receded on the fabricated petal under UV exposure as shown in Figure 65c.

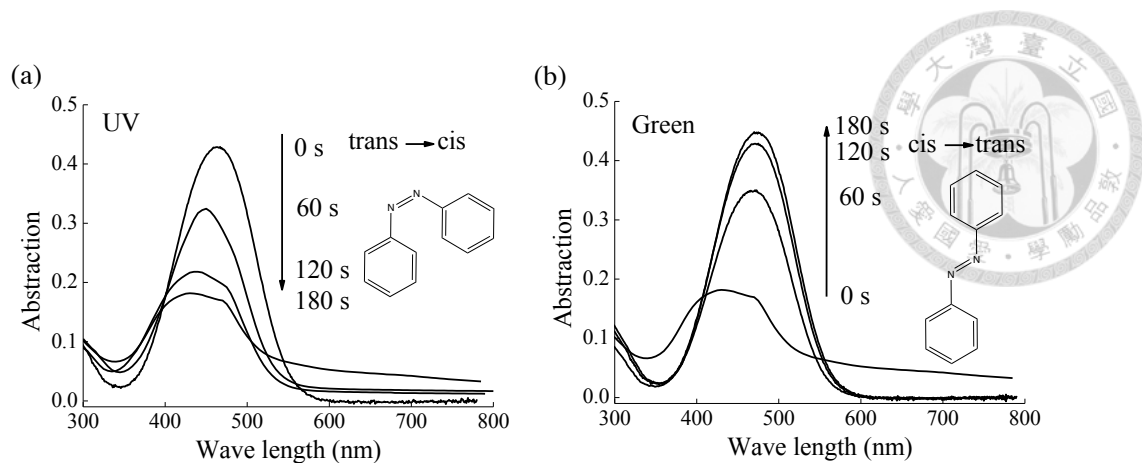


Figure 64. Temporal evolution of the absorbance spectrum of the artificial Azo-IPN petal under the exposure of (a) UV light and (b) green light.

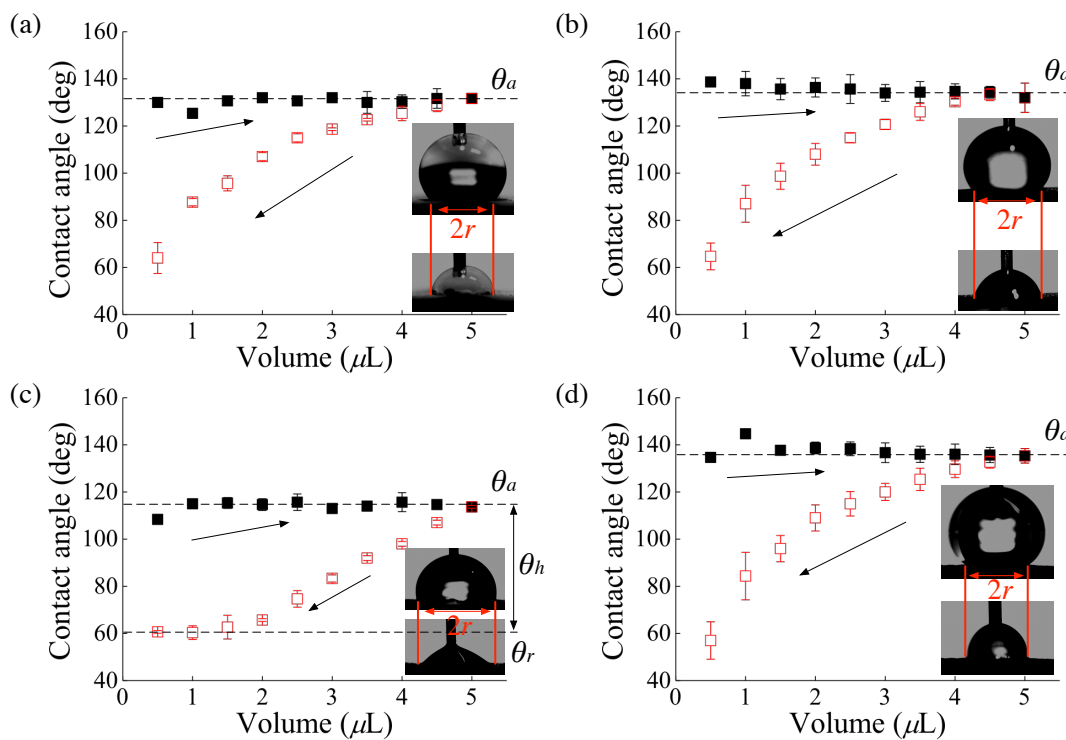


Figure 65. Comparison of the measured contact angle hysteresis θ_h on (a) a real rose.

The wettability of a surface is generally determined by the surface geometry and the surface energy, which are correlated to the surface roughness and dipole moment, respectively. The roughness was estimated from laser confocal microscope and SEM images after UV and green light respectively (Figure 66 and 67).

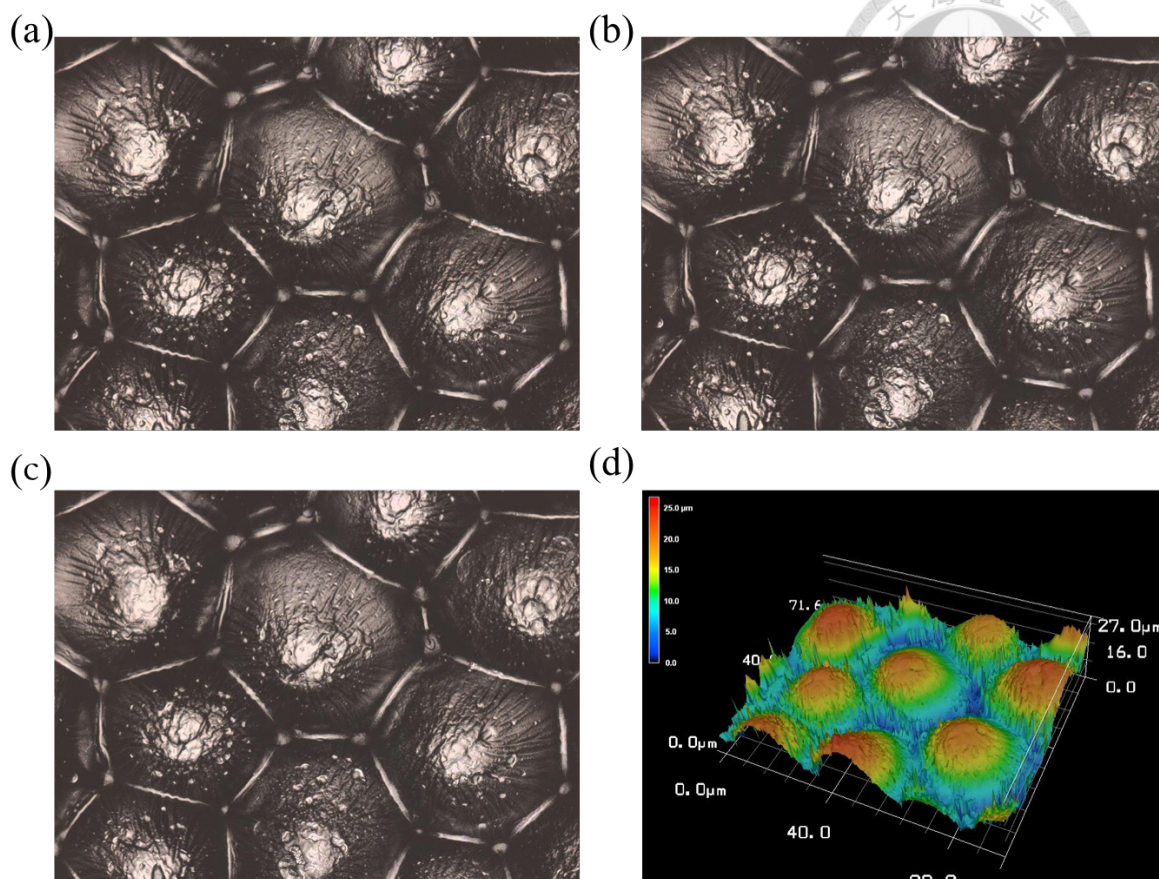


Figure 66. Top-view images, taken with laser confocal microscope: (a) without exposure, (b) UV light (365 nm wavelength, 15 mW/cm²), (c) green light (530 nm wavelength, 20 mW/cm²), (d) 3D image display of Azo-IPN film.

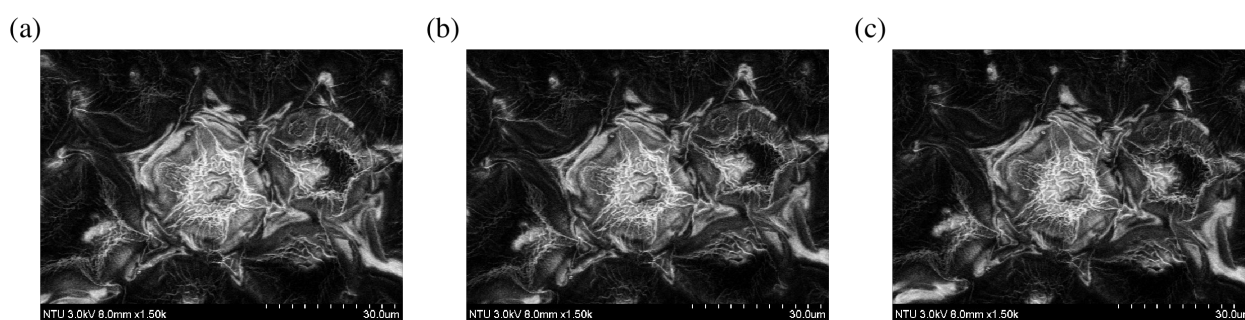


Figure 67. Top-view images, taken with scanning electron microscopy: (a) without exposure, (b) UV light (365 nm wavelength, 15 mW/cm²), (c) green light (530 nm wavelength, 20 mW/cm²)

The root-mean -square roughness changed from 5.12 μm to 5.16 μm and 5.11 μm after the UV and green light exposure, respectively. The change of surface morphology

is not obvious. Therefore, the change of wettability is mainly attributed to the changes of the polarity induced by the photoisomerization of azobenzene. From the FTIR measurement, the characteristic of azobenzene was more obvious after UV exposure (Figure 68).

The FTIR spectrum of Azo-IPN film extract as depicted in Figure 68 shows the difference after different light exposure. The vibration band at 2300 cm^{-1} corresponds to benzene group in azobenzene moieties after UV exposure, although, the Azo-IPN film was too thick to decrease most of the transmittance. This band disappeared after green light exposure, and it was the same as Azo-IPN film without exposure. From FTIR with different exposure, it means that the Azo-IPN film is reversible.

We also injected or removed deionized water to the droplet so that the droplet expended or extracted to permit the measurements of the advancing and the receding angle, θ_a and θ_r , and the evaluation of the contact angle hysteresis, θ_h , as eq (3.1)

The contact-line pinning was prominent on both the real and the fabricated petal in most conditions so that the receding angle and hence the angle hysteresis cannot be precisely measured. Nevertheless, we can still confirm that the contact angle characteristics can be fairly reproduced on the artificial petal and successfully modulated. In view of the angle hysteresis, we can exploit green-line to increase it from 71° on the real rose petal to 84° and reversibly reduce it to $50.3 \pm 0.6^\circ$ after UV-light exposure. The cyclic variation of the contact angle hysteresis by alternating the wavelength of the exposure light is demonstrated in Figure 69. This Azo-IPN film can still be reversibly actuated after 20 times exposure. It has been reported that the trans-to-cis isomerization transition can be reversible for 10^5 to 10^6 cycles [82].

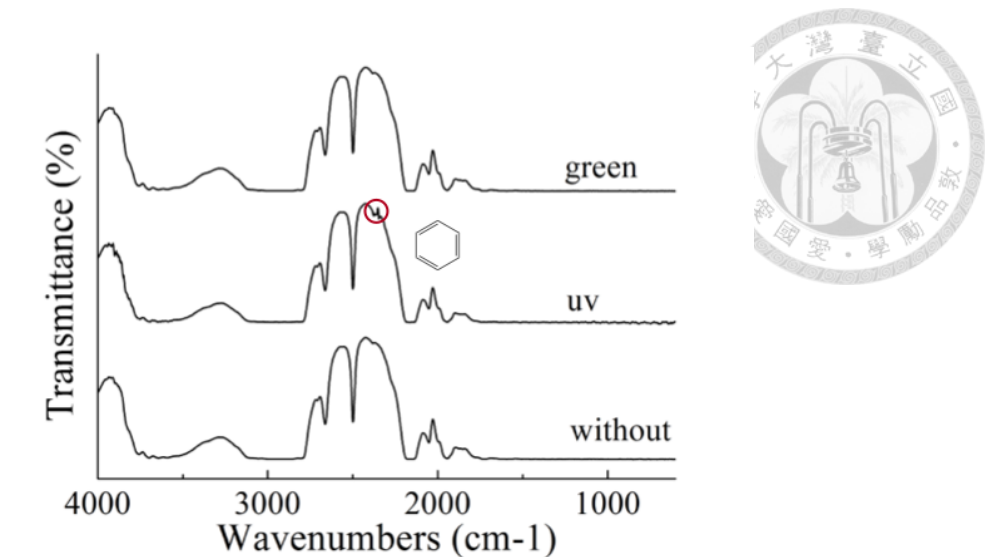


Figure 68. FTIR of Azo-IPN film after different light exposure

Table 3. Measured contact angle and contact angle hysteresis of deionized water on artificial petal of Azo-IPN film.

Substrate	Contact angle (°)			
	Static (θ)	Advancing (θ_a)	Receding (θ_r)	Hysteresis (θ_h)
Real rose petal	129.4 ± 1.5	135.2 ± 0.5	< 64	> 71
Artificial Azo-IPN petal	135.2 ± 1.6	140.1 ± 1.5	< 64	> 76
after 180s UV light exposure	99.2 ± 0.9	110.6 ± 0.6	60.3 ± 0.8	50.3 ± 0.6
after 180s green light exposure	140.9 ± 1.8	141.2 ± 1.1	< 57	> 84

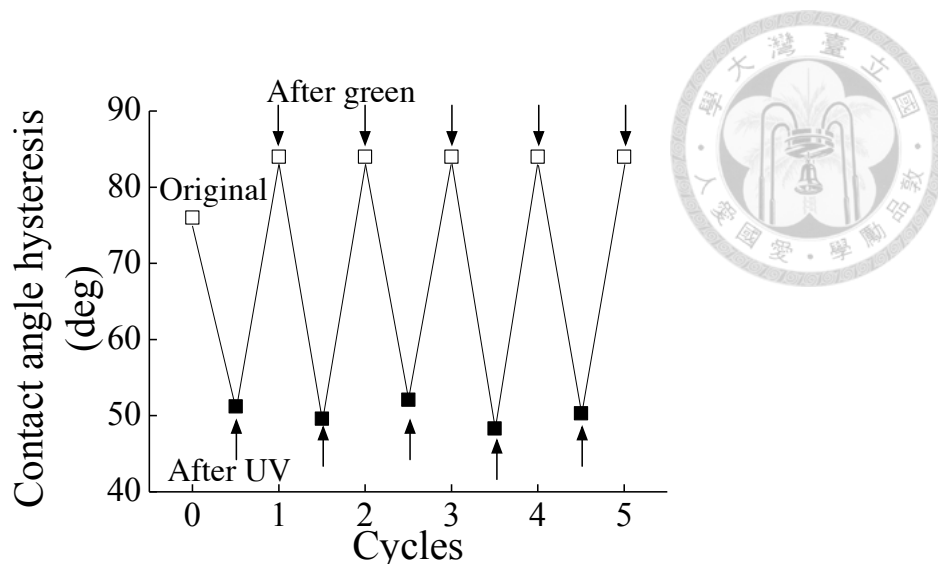


Figure 69. Cyclic variation of the contact angle hysteresis by alternating the wavelength of the exposure light.

Finally, to further illustrate the photo-controllability of the fabricated Azo-IPN petal surface, we recorded the dynamics of a deionized water when it was applied onto an inclined petal surface and subject to different light exposure.

First, the petal surface was irradiated by the UV light (365 nm wavelength, 15 mW/cm² intensity) for 3 minutes before we applied a droplet. We then tilted the petal to 40 degrees from the horizontal and the droplet slid down. We used high-pressure air stream to dry the petal and then exposed it to the green light (530 nm wavelength, 20 mW/cm² intensity) for 3 minutes and an applied droplet can be pinned when the petal was at the same inclination angle as shown in Figure 70 (Multimedia view) which indicates strong petal effect. This petal-effect can be degraded again to allow the droplet to move again by an UV light exposure and enhanced once more with the green light exposure. The droplet can slide down on artificial Azo-petal surface after UV irradiation (Figure 70a), and be pinned on the Azo-petal surface after green light irradiation (Figure 70b). Reversible tuning of the surface property to modulate the degree of petal effect is the novelty of this work.

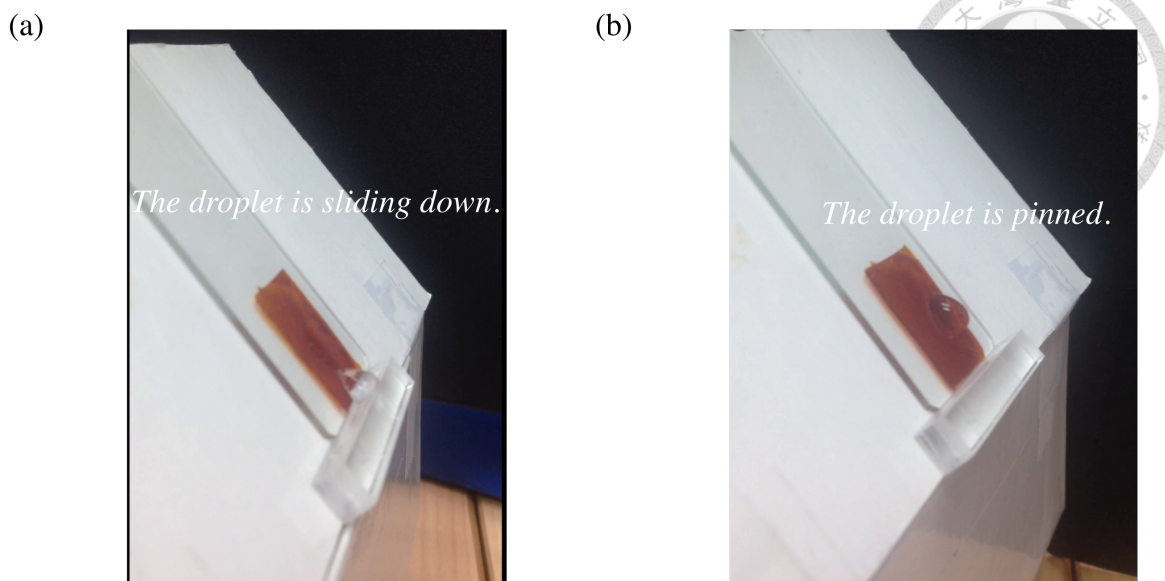
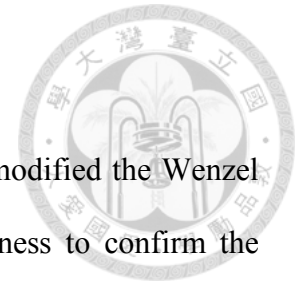


Figure 70. Reversible tenability of the degree of petal effect of a fabricated Azo-IPN petal after exposure to light of various wavelengths. (a) After exposure to UV light (365 nm wavelength, 15 mW/cm² intensity) for 3 minutes. (b) After exposure to green light (530 nm wavelength, 20 mW/cm² intensity) for 3 minutes.

4.4 Conclusion

Comparing to the sample rose petal, the present Azo-IPN artificial counterpart exhibits even more prominent petal effect in terms of its greater contact angle and higher contact angle hysteresis. In addition, the large yet reversible contact angle hysteresis of 31° has never been achieved before and permits effective droplet maneuverability. This biomimetic work thus offers a promising means to control droplet adhesion by the noncontact, fast and reversible method which shall find wide applications in microfluidics, photoelectronics, cell culturing, and optical data storage

Chapter 5 Conclusions



In conclusion, this study takes the line tension in account to modified the Wenzel equation, and designs a solid surface with various surface roughness to confirm the equation, and produces an artificial Azo-IPN petal which can control the contact angle hysteresis fast and reversibly. The contributions of this dissertation are described in detail as follow.

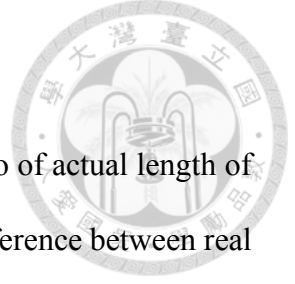
First, we presented the relationship of the line tension and Young equation, Wenzel equation and Gibbs free energy. This study experimentally investigated the role of line tension in the contact angle hysteresis of a droplet on different micromachined surfaces. The empirical equation has been developed to modulated the line tension and contact angle hysteresis.

Second, the line tension can be positive and negative. It always does the opposite movement to pin the droplet. The ratio (κ) of actual length of the three-phase contact line to the apparent and the structure length (L) mainly affect the line tension in the receding state.

Third, by changing κ and L , the static contact angle and the contact angel hysteresis can be altered. The κ and L are important than surface roughness in the hysteresis, from eq (3.4). The contact angle hysteresis can be estimated by knowing these characters.

Forth, the artificial Azo-IPN petal offers a promising means to control droplet adhesion with noncontact, fast and reversible method which shall find wide applications in microfluidics, photoelectronics, cell culturing.

Finally, surface roughness and surface energy are two main factors in wetting behavior. From the experiment, changing the surface energy can alter the contact angle hysteresis efficiently.



.Chapter 6 Future works

In this chapter, we would redefine the surface roughness (λ) and ratio of actual length of the three-phase contact line to the apparent (κ) for decreasing the difference between real case and theoretical model. And the new derivation would be introduced to confirm the role of the line tension.

6.1 Redefined surface roughness (λ) and ratio of actual length of the three-phase contact line to the apparent (κ)

From Figure 71, the surface roughness would be redefined from the red-dash square. The red-dash square is defined as a characteristic structure. The surface roughness (λ) is defined as $\lambda \equiv A_{\text{all}}/A_{\text{apparent}}$ (A_{all} is the area of the rough surface; A_{apparent} is the area of smooth surface), so

$$A_{\text{apparent}} = (L + D)^2 = (L + L * DR)^2 = [L * (1 + DR)]^2 \quad \text{for } DR = D/L \quad (6.1)$$

Where the L is the microstructure lengths, D is the distance and DR is the duty ratio ($DR = D/L$).

$$A_{\text{pyramid}} = 4 * \frac{\sqrt{3}}{4} L^2 = \sqrt{3} L^2 \quad (6.2)$$

Where A_{pyramid} is the side area of the pyramid.

And the A_{all} is

$$A_{\text{all}} = A_{\text{apparent}} - L^2 + A_{\text{pyramid}}$$

So, the surface roughness (λ) can be calculated by

$$\begin{aligned} \lambda &= \frac{A_{\text{all}}}{A_{\text{apparent}}} = \frac{[L * (1 + DR)]^2 - L^2 + \sqrt{3} L^2}{[L * (1 + DR)]^2} \\ &= \frac{(1 + DR)^2 - 1 + \sqrt{3}}{(1 + DR)^2} = \frac{DR^2 + 2DR + \sqrt{3}}{(1 + DR)^2} \end{aligned} \quad (6.3)$$

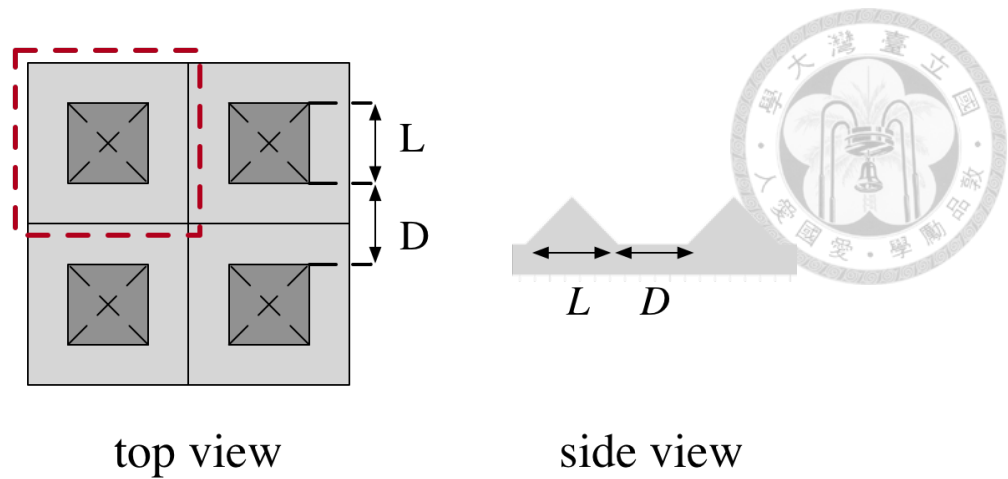


Figure 71. Schematic view of the surface.

Table 4. Surface roughness (λ) for different DR

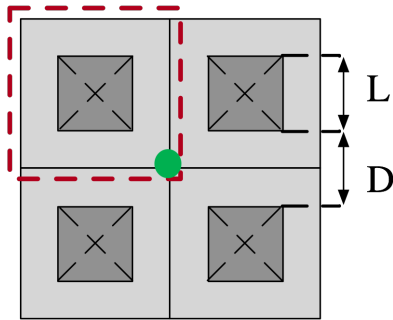
DR	1	2	3	4	5
Surface roughness	1.18	1.08	1.04	1.03	1.02

From this definition, the new surface roughness for different DR are presented in Table 4.

The ratio of actual length of the three-phase contact line to the apparent (κ) is redefined by calculating the expectation value from drawing the real contact line of the droplet (Figure 72). In Figure 72(a), the green spot is the center of the contact line, and the red-dash square is the characteristic structure which is the same as the square in Figure 72(b). For its symmetry, the κ can be calculate just from the 1/4 circle. Take the length of the characteristic square as the unit length, and the 1/4 circle can be separate to 45 sections. From experiment data, the actual ratios of actual length of the three-phase contact line to the apparent (κ) for $DR=1$ are showing in Table 5. The expectation value of the κ for $DR=1$ is 1.048. The all κ of various DR are presented in Table 6.

From the new surface roughness (λ) and ratio of actual length of the three-phase contact line to the apparent (κ), the experiment data can be re-analyzed to confirm the role of the line tension in contact angle hysteresis.

(a)



(b)

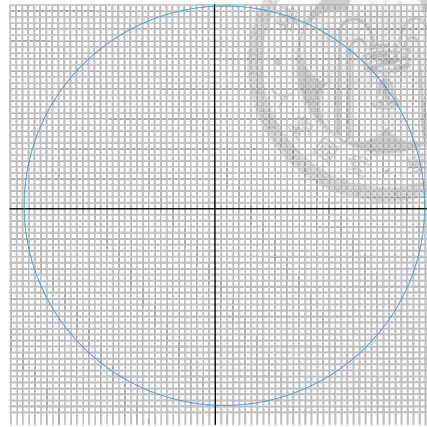


Figure 72. (a) The image of the characteristic structure (red-dash square) and the center of the contact line of the droplet (green spot). (b) The image of the contact line of the droplet. A square means a characteristic structure, as the red-dash square.

Table 5. The numbers of different ratios of 45 sections for $DR=1$:

Case	Ratio	1.41	1.37	1.05	1.12	1
1	Numbers	1	3	13	2	26
2	Numbers	1	1	15	4	24
3	Numbers	1	1	16	1	26

Table 6. The ratio of actual length of the three-phase contact line to the apparent (κ) for different DR .

DR	1	2	3	4	5
κ	1.048	1.036	1.032	1.031	1.029

6.2 New derivation

For a droplet resting on a solid surface, the contact angle, θ_o , at the liquid-solid-vapor interface can be derived from thermodynamics. Herein θ_o is referred to as the intrinsic contact angle under the assumption of ideally smooth solid surface. By

accounting three-phase line tension, τ , its static equilibrium can be expressed by the modified Young's equation as [84]

$$\gamma_{LV} \cos \theta_o = \gamma_{SV} - \gamma_{LS} - \frac{\tau}{r} \quad (6.4)$$

where r is the base radius of the droplet; γ_{SV} , γ_{LS} , and γ_{LV} represent the solid-vapor, liquid-solid, and liquid-vapor interfacial tension, respectively. This modification implies that either the contact angle or the line tension depends on the droplet size. If constant contact angle is assumed, then the line tension will be linearly proportional to the base radius. The effect of line tension on the contact angle will be further examined by experiment. Herein it is accounted throughout the following derivation for complete discussion. One can simply let $\tau = 0$ to ignore the line tension for the whole analysis.

For the contact line to virtually move a distance, δx , on a textured solid surface (Figure 73), the required work, δE , is

$$\delta E = \left[f(\gamma_{LS} - \gamma_{SV}) + \gamma_{LV} \cos \theta + f \frac{\tau}{r} \right] 2\pi \delta x \quad (6.5)$$

where θ_o is the apparent contact angle of the droplet subjected to the textures. f is the roughness ratio of the textured surface. To minimize the required work for the contact line to maintain equilibrium,

$$\delta E = 0 \quad (6.6)$$

Therefore,

$$f(\gamma_{LS} - \gamma_{SV}) + \gamma_{LV} \cos \theta + f \frac{\tau}{r} = 0 \quad (6.7)$$

Substituting (6.4) into (6.7) leads to the Wenzel's model as

$$\cos \theta = f \cos \theta_o \quad (6.8)$$

Even by taking the line tension into account, this derivation shows that the Wenzel' model remain unchanged.



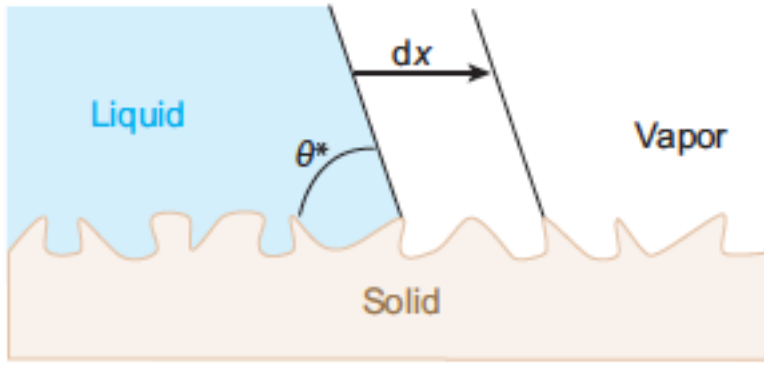


Figure 73. Illustration of moving contact line on a textured surface.

Based on Makkonen's work, the advancing angle, θ_a , allows the liquid-vapor interfacial tension to compensate the additional friction tension, F , so that the contact line can continuously move forward [85]. Specifically,

$$F = \gamma_{LV} (\cos \theta - \cos \theta_a) \quad (6.9)$$

For the contact line to advance with a distance, dx , on a textured surface, the increase of interfacial energy, dE , is

$$dE = f\gamma_{LS}2\pi dx + \lambda \frac{\tau}{r} 2\pi dx \quad (6.10)$$

It should be noted that the line tension is accounted by assuming that the contact line advances uniformly in the radial direction. Therefore, the additional friction tension, F , is

$$F = \frac{dE}{2\pi dx} = f\gamma_{LS} + f \frac{\tau}{r} \quad (6.11)$$

Applying (6.4) and (6.8) into (6.9) and (6.11) leads to

$$\cos \theta_a = f \frac{\gamma_{SV}}{\gamma_{LV}} - 2f \frac{\gamma_{SL}}{\gamma_{LV}} - 2f \frac{\tau}{r\gamma_{LV}} \quad (6.12)$$

Thus, the advancing angle can be calculated given the interfacial tensions, surface roughness, and base radius.

For the droplet to continuously retract, the additional frictional tension accounts for the newly generated solid-vapor interface and the contraction of the contact line. Therefore, it becomes

$$F = f\gamma_{SV} - f\frac{\tau}{r} \quad (6.13)$$

Again, the additional friction tension is compensated by the liquid-vapor interfacial tension with a receding angle, θ_r . That is,

$$f\gamma_{SV} - f\frac{\tau}{r} = \gamma_{LV}(\cos\theta_r - \cos\theta) \quad (6.14)$$

Applying (6.4) and (6.8) into (6.14) leads to

$$\cos\theta_r = 2f\frac{\gamma_{SV}}{\gamma_{LV}} - f\frac{\gamma_{SL}}{\gamma_{LV}} - 2f\frac{\tau}{r\gamma_{LV}} \quad (6.15)$$

Equations (6.12) and (6.14) indicate correlate the advancing and receding angles to the interfacial tension and surface roughness.

The relation between interfacial tensions can be empirically described by modified Berthelot's rule [86],

$$\gamma_{SL} = \gamma_{SV} + \gamma_{LV} - 2\phi(\gamma_{SV}\gamma_{LV})^{1/2} \quad (6.16)$$

where ϕ is the parameter of solid-liquid interfacial interaction. Applying (6.16) into (6.14) leads to

$$\frac{\gamma_{SV}}{\gamma_{LV}} = \frac{1}{4\phi^2} \left(1 + \cos\theta + \frac{\tau}{r\gamma_{LV}} \right)^2 \quad (6.17)$$

$$\frac{\gamma_{SL}}{\gamma_{LV}} = \frac{1}{4\phi^2} \left(1 + \cos\theta + \frac{\tau}{r\gamma_{LV}} \right)^2 - \cos\theta - \frac{\tau}{r\gamma_{LV}} \quad (6.18)$$

By applying (6.17) and (6.18) into the summation of (9) and (12), it is found that the empirical parameter, ϕ , diminished. That is,

$$\cos \theta_a + \cos \theta_r = 3f \cos \theta - f \frac{\tau}{r\gamma_{LV}} \quad (6.19)$$

For the case of $\tau=0$, the summation of the cosine of the advancing and receding angles is a constant if the interfacial tensions and surface roughness are prescribed. Specifically,

$$\cos \theta_a + \cos \theta_r = 3f \cos \theta \quad (6.20)$$

This result is consistent with Makkonen's derivation [85].

By applying (6.17) and (6.18) into (6.12) and (6.15), the contact angle hysteresis can be expressed as

$$\cos \theta_a - \cos \theta_r = -\frac{f}{2\phi^2} \left(1 + \cos \theta + \frac{\tau}{r\gamma_{LV}} \right)^2 + f \cos \theta + \frac{\lambda\tau}{r\gamma_{LV}} \quad (6.21)$$

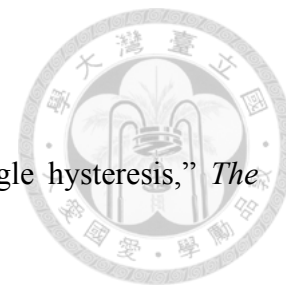
For water-based systems, $\phi \sim 1$ [85]. Therefore, the contact angle hysteresis of a water droplet can be estimated by

$$\cos \theta_a - \cos \theta_r = -\frac{f}{2} \left[\left(\cos \theta + \frac{\tau}{\lambda L \gamma_{LV}} \right)^2 + 1 \right] \quad (6.22)$$

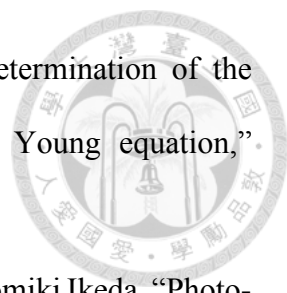
where $\lambda \equiv r/L$ denotes the ratio of the droplet base radius to the feature size, L , on the textured surface.

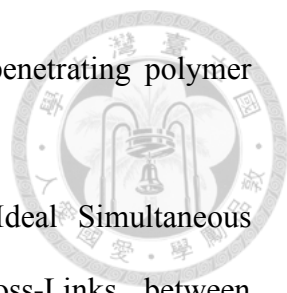
In the experiment, the advancing and receding angles are measured and then applied into (6.19) and (6.20) for comparison. The result will verify whether the line tension affects the contact angle or not. If equation (6.19) rather than (6.20) is valid, then the experimental results are applied into equation (6.22) to verify the effect the feature size on the contact angle hysteresis. Instead, if equation (6.20) is valid, Makkonen's derivation is confirmed. We can then further confirm that the prediction of contact angle hysteresis, by letting $\tau=0$ in (6.22), is independent of the droplet size.


References

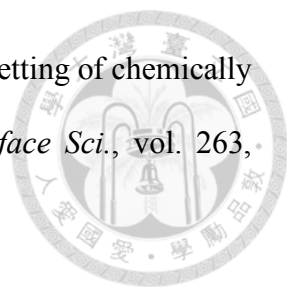


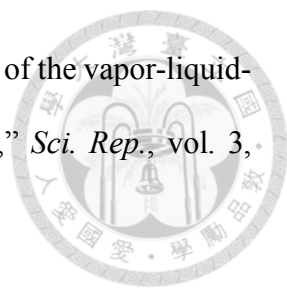
- [1] J.F. Joanny, and P.G. De Gennes, “A model for contact angle hysteresis,” *The Journal of Chemical Physics*, vol. 81, pp.552-562, 1984.
- [2] E.B. Dussan, and R.T.P. Chow, “On the ability of drops or bubbles to stick to non-horizontal surfaces of solids,” *J. Fluid Mech.* vol.137, pp.1-29, 1983.
- [3] P.G. De Gennes, “Wetting: statics and dynamics,” *Rev. Mod. Phys.* vol. 57, pp.827-863, 1985.
- [4] C.W. Extrand, “A thermodynamic model for contact angle hysteresis,” *J. Colloid & Interface Sci.*, vol. 207, pp.11-19, 1998.
- [5] D. Bonn, J. Eggers, J. Indekeu, J. Meunier, and E. Rolley, “Wetting and spreading,” *Rev. Mod. Phys.*, vol. 81, pp.739-805, 2009.
- [6] J. Hyvaluoma, A. Koponen, P. Raiskinmaki, and J. Timonen, “Droplets on inclined rough surfaces,” *Euro. Phys. J. E*, vol. 23, pp.289-293, 2007.
- [7] F.E. Bartell, and J.W. Shepard, “Surface Roughness as Related to Hysteresis of Contact Angles. II. The Systems Paraffin–3 Molar Calcium Chloride Solution–Air and Paraffin–Glycerol–Ai,” *J. Phys. Chem.*, vol. 57, pp.455-458, 1953.
- [8] E.B. Dussan, “On the ability of drops to stick to surfaces of solids. Part 3. The influences of the motion of the surrounding fluid on dislodging drops,” *J. Fluid Mech.*, vol. 174, pp.381-397, 1987.
- [9] E.B. Dussan, “On the ability of drops or bubbles to stick to non-horizontal surfaces of solids. Part 2. Small drops or bubbles having contact angles of arbitrary size,” *J.Fluid Mech.*, vol. 151, pp.1-20, 1985.
- [10] Edward Bormashenko, and Gene Whyman, “On the Role of the Line Tension in the Stability of Cassie Wetting,” *Langmuir*, vol. 29, pp.5515–5519, 2013.

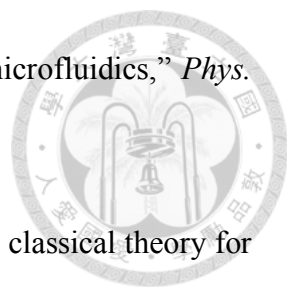
- 
- [11] Yawei Liu, Jianjun Wang, and Xianren Zhang, “Accurate determination of the vapor-liquid-solid contact line tension and the viability of Young equation,” *Scientific Reports*, vol. 3, 2013.
- [12] Christopher J. Barrett, Jun-ichi Mamiy, Kevin G. Yagerc, and Tomiki Ikeda, “Photo-mechanical effects in azobenzene-containing soft materials,” *Soft Matter*, vol. 3, pp.1249-1261, 2007.
- [13] G. S. Hartley, “The cis-form of azobenzene,” *Nature*, vol. 140, pp.281-281, 1937.
- [14] G. S. Hartley, “The cis-form of azobenzene and the velocity of the thermal cis -> trans-conversion of azobenzene and some derivatives,” *Journal of the Chemical Society*, pp.633-642, 1938.
- [15] P. P. Birnbaum, J. H. Linford, and D. W. G. Style, “The absorption spectra of azobenzene and some derivatives,” *Transactions of the Faraday Society*, vol. 49, pp.735-744, 1953.
- [16] George Zimmerman, Lue-Yung Chow, and Un-Jin Paik, “The Photochemical Isomerization of Azobenzene,” *Journal of the American Chemical Society*, vol. 80, pp.3528-3531, 1958.
- [17] Miguel Camacho-Lopez, Heino Finkelmann, Peter Palffy-Muhora, and Michael Shelley, “Fast liquid-crystal elastomer swims into the dark,” *Nature Materials*, vol. 3, pp.307-310, 2004.
- [18] Hyun-Kyoung Kim, Xiao-Shui Wang, Yukihiro Fujita, Atsushi Sudo, Haruo Nishida Masayuki Fujii, and Takeshi Endo, “Photomechanical Switching Behavior of Semi-Interpenetrating Polymer Network Consisting of Azobenzene-Carrying Crosslinked Poly(vinyl ether) and Polycarbonate,” *Macromolecular Rapid Communications*, vol. 26, pp.1032-1036, 2005.


- 
- [19] L. H. Sperling, and V. Mishra, “The current status of interpenetrating polymer networks,” *Polym. Adv. Technol.*, vol. 7, pp.17-208, 1996.
- [20] T. Kiguchi, H. Aota, and A. Matsumoto, “Approach to Ideal Simultaneous Interpenetrating Network Formation via Topological Cross-Links between Polyurethane and Polymethacrylate Network Polymer Precursors,” *Macromolecules*, vol. 37, pp.8249-8255, 2004.
- [21] Yizhong Huang, Hongliang Kang, Guanghua Li, Chunying Wang, Yong Huang, and Ruigang Liu, “Synthesis and photosensitivity of azobenzene functionalized hydroxypropylcellulose,” *RSC Advances*, vol. 3, pp.15909-15916, 2013.
- [22] L. Boruvka, and A. W. Neumann, “Generalization of the classical theory of capillarity,” *The Journal of Chemical Physics*, vol. 66, pp. 5464-5476, 1977.
- [23] W. Barthlott, and C. Neinhuis, “Purity of the sacred lotus, or escape from contamination in biological surfaces,” *Planta*, vol. 202, pp.1-8, 1997.
- [24] X. Gao, and L. Jiang, “Biophysics: Water-repellent legs of water striders,” 432, 36. 2004.
- [25] Y. Zhang, Y. Cheng, L. Shi, J. Li, and Z. Guo, “Recent progress of double-structural and functional materials with special wettability,” *J. Mater. Chem.*, vol. 22, pp.799-815, 2012.
- [26] L. Feng, S. Li, Y. Li, H. Li, L. Zhang, J. Zhai, Y. Song, B. Liu, L. Jiang, and B. D. Zhu, “Super-Hydrophobic Surfaces: From Natural to Artificial,” *Adv. Mater.*, vol. 14, pp.1857-1860, 2002.
- [27] L. Feng, Y. Zhang, J. Xi, Y. Zhu, N. Wang, F. Xia, and L. Jiang, “Petal Effect: A Superhydrophobic State with High Adhesive Force,” *Langmuir*, vol. 24, pp.4114-4119, 2008.

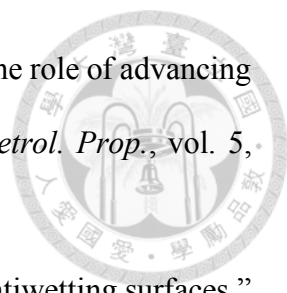
- 
- [28] A. Cassie, and S. Baxter, “Wettability of porous surfaces,” *Trans. Faraday Soc.*, vol. 40, 546-551, 1944.
- [29] R. N. Wenzel, “Resistance of solid surfaces to wetting by water,” *Indust. Eng. Chem.*, vol. 28, pp.988-994, 1936.
- [30] P. G. De Gennes, F. Brochard-Wyrt, and D. Quéré, *Capillarity and Wetting Phenomena*; Springer: Berlin, 2003.
- [31] Z. Yoshimitsu, A. Nakajima, T. Watanabe, and K. Hashimoto, “Effect of surface structure on the hydrophobicity and sliding behavior of water droplet,” *Langmuir*, vol. 18, pp.5818-5822, 2002.
- [32] D. Quéré, “Wetting and roughness,” *Ann. Rev. Matter. Res.*, vol. 38, pp.71-99, 2008.
- [33] N. A. Patankar, “On the Modeling of Hydrophobic Contact Angles on Rough Surfaces,” *Langmuir*, vol. 19, pp.1249-1253, 2003.
- [34] D. Quéré, “Rough ideas on wetting,” *Physica A*, vol. 313, pp.2-46, 2002.
- [35] G. Palasantzas, and J. T. M. de Hosson, “Wetting on rough surface,” *Acta Mater.*, vol. 49, pp.3533-3538, 2001.
- [36] H. Nakae, R. Inui, Y. Hirata, and H. Saito, “Effects of surface roughness on wettability,” *Acta Mater.*, vol. 46, pp.2313-2318, 1998.
- [37] K. Topolski, D. Urban, S. Brandon, and J. Deconinck, “Influence of the geometry of a rough substrate on wetting,” *Phys. Rev. E*, vol. 56, pp.3353-3357, 1997.
- [38] G. Wolansky, and A. Marmur, “Apparent contact angles on rough surfaces: the Wenzel equation revisited,” *Colloids Surf. A*, vol. 156, pp.381-388, 1998.

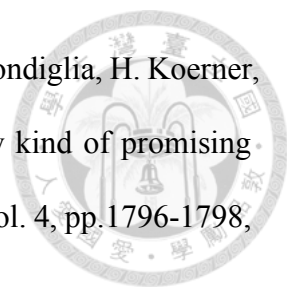
- 
- [39] S. Brandon, N. Haimovich, E. Yeager, and A. Marmur, "Partial wetting of chemically patterned surfaces: The effect of drop size," *J. Colloid Interface Sci.*, vol. 263, pp.237-243, 2003.
- [40] G. Wolansky, and A. Marmur, "The Actual Contact Angle on a Heterogeneous Rough Surface in Three Dimensions," *Langmuir*, vol. 14, pp.5292-5297, 1998.
- [41] A. Marmur, and B. Krasovitsi, "Line tension on curved surfaces: Liquid drops on solid micro- and nanospheres," *Langmuir*, vol. 18, pp.8919-8923, 2002.
- [42] S. Suzuki, and K. Ueno, "Apparent Contact Angle Calculated from a Water Repellent Model with Pinning Effect," *Langmuir*, vol. 33 (1), pp.138–143, 2017.
- [43] J. A. Wallace, and S. Schurch, "Line tension of sessile drops placed on a phospholipid monolayer at the water-fluorocarbon interface," *Colloids Surf.*, vol. 43, pp.207-221, 1990.
- [44] J. Drelich, and J. D. Miller, "Modification of the Cassie equation," *Langmuir*, vol. 199(2), pp.619-621, 1993.
- [45] C. Huh, and S. G. Mason, "Effects of surface roughness on wetting (Theoretical)," *J. Colloid Interface Sci.*, vol. 60, pp.11-38, 1977.
- [46] J. W. Gibbs, "The Collected Works of J. Willard Gibbs, 1, 288, New Haven, Yale University Press, London, 1957.
- [47] J. S. Rowlinson, and B. Widom, "Molecular Theory of Capillarity," Oxford Science Publications, New York, 1984.

- 
- [48] Y. W. Liu, J. J. Wang, and X. R. Zhang, “Accurate determination of the vapor-liquid-solid contact line tension and the viability of Young equation,” *Sci. Rep.*, vol. 3, pp.2008-2013, 2013.
- [49] J. Drelich, “The significance and magnitude of the line tension in three-phase (solid-liquid-fluid) systems,” *Colloids Surf. A*, vol. 116, pp.43-54, 1996.
- [50] A. Amirfazli, and A. W. Neumann, “Status of the three-phase line tension,” *Adv. Colloid Interface Sci.*, vol. 110, pp.121-141, 2004.
- [51] L. Schimmele, M. Napiórkowski, and S. Dietrichl, “Conceptual aspects of line tensions,” *J. Chem. Phys*, vol. 127, 164715, 2007.
- [52] L. O. Heim, and E. Bonaccorso, “Measurement of line tension on droplets in the submicrometer range,” *Langmuir*, vol. 29, pp.14147-14153, 2013.
- [53] Y. G. Gu, D. Q. Li, and P. Cheng, “Determination of line tension from the shape of axisymmetric liquid-vapor interfaces around a conic cylinder,” *J. Colloid Interface Sci.*, vol. 180, pp.212-217, 1996.
- [54] A. Checco, and P. Guenoun, “Nonlinear dependence of the contact angle of nanodroplets on contact line curvature,” *Phys. Rev. Lett.*, vol. 91, 186101, 2003.
- [55] J. Drelich, and J. D. Miller, “The line/pseudo-line tension in three-phase system,” *Particul. Sci. Technol.*, vol. 10, pp.1-20, 1992.
- [56] R. D. Peter, X. M. Yang, and T. K. Kim, “Wetting behavior of block copolymers on self-assembled films of alkylchlorosiloxanes: effect of grafting density,” *Langmuir*, vol. 16, pp.9620-9626, 2000.

- 
- [57] G. M. Whitesides, and A. D. Stroock, “Flexible methods for microfluidics,” *Phys. Today*, vol. 54, 42, 2001.
- [58] D. Winter, P. Virnau, and K. M. Binder, “Monte carlo test of the classical theory for heterogeneous nucleation barriers,” *Phys. Rev. Lett.*, vol. 103, 225703, 2009.
- [59] B. V. Toshev, “Thermodynamic theory of thin liquid films including line tension effects,” *Current Opinion in Colloid & Interface Science*, vol. 13, pp.100-106, 2008.
- [60] J. M. Kim, F. Wolf, and S. K. Baier, “Effect of varying mixing ratio of PDMS on the consistency of the soft-contact Stribeck curve for glycerol solutions,” *Tribology International*, vol. 89, pp.46-53., 2015.
- [61] A. Amirfazli, S. Hänig, A. Müller, and A. W. Neumann, “Measurements of line tension for solid-liquid-vapor system using drop size dependence of contact angles and its correlation with solid-liquid interfacial tension,” *Langmuir*, vol. 16, pp.2024-2031, 2000.
- [62] R. Di Mundo, R. d’Agostino and F. Palumbo, “Long-Lasting Antifog Plasma Modification of Transparent Plastics,” *ACS Appl. Mater. Interfaces*, vol. 6, pp.17059-17066, 2014.
- [63] M. Nosonovsky and B. Bhushan, “Biomimetic Superhydrophobic Surfaces: Multiscale Approach,” *Nano Lett.*, vol. 7, pp.2633-2637, 2007
- [64] D. Dilip, N. K. Jha, R. N. Govardhan and M.S. Bobji, “Controlling air solubility to maintain “Cassie” state for sustained drag reduction,” *Colloids Surf. A: Physicochem. Eng. Aspects*, vol. 459, pp.217-224, 2014.
- [65] M. V. Graham and N. C. Cady, “Nano and Microscale Topographies for the Prevention of Bacterial Surface Fouling,” *Coatings*, vol. 4, pp.37-59, 2014.

- 
- [66] R. N. Wenzel, "RESISTANCE OF SOLID SURFACES TO WETTING BY WATER," *Ind. Eng. Chem.*, vol. 28, pp.988-994, 1936
- [67] N. Senbil and A. D. Dinsmor, "Deformation of the contact line around spherical particles bound at anisotropic fluid interfaces," *Soft Matter*, vol. 13, pp.8232-8239, 2017.
- [68] D. Lee, S. H. Baek, T. H. Kim, J.-G. Yoon, C. M. Folkman, C. B. Eom, and T. W. Noh, "Polarity control of carrier injection at ferroelectric/metal interfaces for electrically switchable diode and photovoltaic effects," *Phys. Rev. B*, vol. 84, 25305, 2011.
- [69] X. Feng, J. Zhai and L. Jiang, "The Fabrication and Switchable Superhydrophobicity of TiO₂ Nanorod Films," *Angew. Chem. Int. Ed.*, vol. 44, pp.5115-5118, 2005.
- [70] Z. Nooralian, M. P. Gashti and I. Ebrahimi, "Fabrication of a multifunctional graphene/polyvinylphosphonic acid/cotton nanocomposite via facile spray layer-by-layer assembly," *RSC Adv.*, vol. 6, 23288, 2016.
- [71] M. P. Gashti, F. Alimohammadi and A. Shamei, "Preparation of water-repellent cellulose fibers using a polycarboxylic acid/hydrophobic silica nanocomposite coating." *Surface and Coatings Technology*, vol. 206, pp.3208-3215, 2012.
- [72] M. P. Gashti, S. Moradian, A. Rashidi and M.-E. Yazdanshenas, "Dispersibility of hydrophilic and hydrophobic nano-silica particles in polyethylene terephthalate films: evaluation of morphology and thermal properties." *Polymers & Polymer Composites*, vol. 23, pp.285-296, 2015
- [73] L. Feng, Y. A. Zhang, M. J. Xi, Y. Zhu, N. Wang, F. Xia and L. Jiang, "Petal Effect: A Superhydrophobic State with High Adhesive Force." *Langmuir*, vol. 24, pp.4114-4119, 2008.

- 
- [74] N. K. Mandsberg and R. Taboryski, “The rose petal effect and the role of advancing water contact angles for drop confinement.” *Surf. Topogr.: Metrol. Prop.*, vol. 5, pp.024001, 2017.
- [75] X. J. Feng and L. Jiang, “Design and creation of superwetting/antiwetting surfaces.” *Adv. Mater.*, vol. 18, pp.3063-3078, 2006.
- [76] Y. Huang, H. Kang, G. Li, C. Wang, Y. Huang and R. Liu, “Synthesis and photosensitivity of azobenzene functionalized hydroxypropylcellulose.” *RSC Adv.*, vol. 3, pp.15909-15916, 2013.
- [77] A. Nakajima, K. Hashimoto and T. Watanabe, “Recent Studies on Super-Hydrophobic Films.” *Monatsh. Chem.*, vol. 132, pp.31-41, 2001.
- [78] X. W. Pei, A. Fernandes, B. Mathy, X. Laloyaux, B. Nysten, O. Riant and A. M. Jonas, “Correlation between the structure and wettability of photoswitchable hydrophilic azobenzene monolayers on silicon.” *Langmuir*, vol. 27, 9403-9412, 2011.
- [79] H. K. Kim, X. S. Wang, Y. Fujita, A. Sudo, H. Nishida, M. Fujii and T. Endo, “Photomechanical Switching Behavior of Semi-Interpenetrating Polymer Network Consisting of Azobenzene-Carrying Crosslinked Poly(vinyl ether) and Polycarbonate.” *Macromol. Rapid Commun.*, vol. 26, pp.1032-1036, 2005.
- [80] T. Kiguchi, H. Aota and A. Matsumoto, “Approach to Ideal Simultaneous Interpenetrating Network Formation via Topological Cross-Links between Polyurethane and Polymethacrylate Network Polymer Precursors.” *Macromolecules*, vol. 37, pp.8249-8255, 2004.
- [81] V. Mishra and L. H. Sperling, “Simultaneous interpenetrating networks of a polyurethane and poly([methyl methacrylate]-stat-[N,N-dimethylacrylamide]).” *J. Polym. Sci., Part B: Polym. Phys.*, vol. 34, pp.883-892, 1996.

- 
- [82] T. J. White, N. Y. Tabiryan, S. V. Serak, U. A. Hrozhyk, V. P. Tondiglia, H. Koerner, R. A. Vaia, T. J. Bunning, "Photodeformable polymers: a new kind of promising smart material for micro- and nano-applications." *Soft Matter*, vol. 4, pp.1796-1798, 2008.
- [83] C. Wu, "Synthesis and characterization of a novel series of unsymmetric dimesogenic compounds containing cholesteryl ester and nitroazobenzene moieties." *Matter. Lett.*, vol. 61, pp.1380-1383, 2007.
- [84] B. Widom, "Line tension and the shape of a sessile drop," *J. Phys. Chem.*, vol. 99, pp.2803-2806, 1995.
- [85] L. Makkonen, "A thermodynamic model for contact angle analysis," *J. Chem. Phys.*, vol. 147, pp.064703, 2017.
- [86] L. A. Girifalco and R. J. Good, "A theory for the estimation of surface and interfacial energies. I. Derivation and application to interfacial tension," *J. Phys. Chem.*, vol. 61, pp.904-909, 1957.